U.PORTO
FACULDADE DE CIÊNCIAS
UNIVERSIDADE DO PORTO

PhD

3rd CYCLE
FCUP
2024

IFU Observations and Ionization Modeling of Extended Halos in High Redshift Active Galaxies

Sandy Gonçalves Morais

IFU Observations and Ionization Modeling of Extended Halos in High Redshift Active Galaxies

Sandy Gonçalves Morais,
Doctoral Program in Astronomy,
Department of Physics and Astronomy,
Faculty of Sciences of the University of Porto
2024

IFU Observations and Ionization Modeling of Extended Halos in High Redshift Active Galaxies

Sandy Gonçalves Morais,
Thesis carried out as part of the Doctoral Program in Astronomy,
Department of Physics and Astronomy,
2024

Supervisor
Andrew Humphrey, Collaborator, Institute of Astrophysics and Space Sciences

Co-supervisor
Montserrat Villar-Martín, Researcher, Center for Astrobiology CSIC-INTA

Acknowledgements

First and foremost I would like to thank my supervisors, Andy and Montse. Without their help, support and patience this work would never have been completed. I would also like to thank Luc Binette for allowing me to use his photoionization code and giving me all the help I needed. A big thanks to all the people I bothered for help with the MUSE data reduction and analysis: Jarle Brinchmann, Giacomo Venturi, Joël Vernet, Luis Peralta de Arriba, Patricio Lagos, Giacomo Venturi, and Marckelson, who not only helped with the MUSE data but with everything else. Also a big thanks to Enrica Bellocchi for all her help and kindness while I was in Madrid. I also want to thank Bjorn Emonts for his help with the ALMA data, even if I ended up not using it.

I acknowledge the support from Fundação para a Ciência e a Tecnologia (FCT) through the Fellowships PD/BD/135228/2017 and COVID/BD/152181/2021, and would like to thank Instituto de Astrofísica e Ciências do Espaço for hosting me during this journey.

Finalmente, e agora em português, quero agradecer à minha família, sem a qual não estaria aqui hoje. Ao meu esponjinho, que acredita em mim mesmo quando eu não acredito e que me apoiou durante os últimos (muitos) anos. Aos meus amigos que me aturaram durante todo o meu percurso académico, principalmente a Ângela e o Camacho que me ouviram queixar mais do que ninguém! Gosto muito de vocês e obrigada por tudo.

Resumo

O estudo do gás ionizado presente em galáxias ativas luminosas que se encontram a alto redshift é essencial para investigar várias características importantes relacionadas com a formação e evolução das galáxias mais massivas do universo. Entre estas características está o impacto que a atividade nuclear tem na galáxia hospedeira, tanto na região nuclear como no meio circumgaláctico, assim como os processos de obtenção e perda de gás durante o crescimento da galáxia.

O trabalho apresentado nesta tese é uma tentativa de estudar diversos mecanismos relacionados com a atividade nuclear em galáxias e de compreender como esses mecanismos influenciam as propriedades cinemáticas, morfológicas e de ionização do gás ionizado nas galáxias ativas mais luminosas (quasares tipo 2 e rádio galáxias de riscas estreitas). Devido ao seu interesse em estudos cosmológicos, esta investigação concentrou-se principalmente (mas não apenas) em galáxias ativas a redshift $\sim$ 2 - 4. O principal objetivo é entender como a atividade nuclear influencia a evolução das galáxias através de diferentes processos, incluindo feedback.

Este trabalho está dividido em dois sub-projectos. Primeiro, concentramo-nos no estudo teórico e observacional dos espectros de riscas de emissão estreitas de $\sim$ 140 galáxias ativas tipo 2 a $z > 2$, tanto rádio galáxias (HzRGs) como quasares, através da comparação de rácios de riscas medidos com previsões de modelos de fotoionização. O papel das distribuições de energia eletrónicas kappa (κ) foi investigado em profundidade pela primeira vez em galáxias ativas, de forma a perceber o impacto que diferentes distribuições de energia têm na determinação das propriedades das galáxias (tais como

ionização, densidade e metalicidade).

O segundo sub-projecto consiste na investigação da nebulosa gigante (~ 150 kpc) de Lyα associada com uma rádio-galáxia a z ~ 3.6, com base em dados de arquivo de espectroscopia de campo integral obtidos com o instrumento MUSE montado no VLT. As implicações dos nossos resultados são discutidas no contexto da física do gás associado com HzRGs a alto redshift. Por fim, são discutidas as perspetivas para pesquisas futuras decorrentes deste trabalho.

Abstract

Studying the ionized gas in high-z luminous active galaxies is essential to investigate several key aspects related to how the most massive galaxies in the universe formed and evolved. Among these are the impact of the nuclear activity on the host galaxy, from the nuclear region out into the circumgalactic medium, as well as the processes of gain or loss of gas during galaxy growth.

The work presented in this thesis is an attempt to study different mechanisms related to the nuclear activity in galaxies and how they influence the ionization, kinematic and morphological properties of the ionized gas in the most luminous active galaxies (type 2 quasars and narrow-line radio galaxies). Because of their relevance in cosmological studies, this investigation has been focused especially (but not only) on z ~ 2 - 4 active galaxies. Ultimately, the goal is to understand how nuclear activity influences the evolution of galaxies via different processes, including feedback.

This work is divided in two sub-projects. First, we focus on the theoretical and observational study of the narrow emission line spectra of ~ 140 type 2 luminous active galaxies at z > 2, both radio galaxies (HzRGs) and quasars, by means of comparing the measured line ratios with photoionization model predictions. The role of the kappa (κ) electron energy distribution (EED) has been investigated in depth for the first time in active galaxies, to understand the impact that different EEDs have on the determination of galaxy properties (such as ionization, density and metallicity).

The second sub-project consists in investigating the giant (~ 150 kpc) Lyα nebula associated with a radio galaxy at z ~ 3.6 based on integral field spectroscopic archive data

obtained with the MUSE instrument on VLT. The implications of our results are discussed in the context of the physics of the gas associated with HzRGs at high redshift. Finally, prospects for future research leading on from this work are discussed.

Contents

List of Figures

List of Tables

Chapter 1

Active Galaxies

Active galaxies are galaxies that host AGN in their center. The term AGN refers to a very small, sub-pc scale central region, that emits radiation across the whole electromagnetic spectrum, from radio wavelengths to γ rays, suggesting that the emission is non-thermal. Despite their small size, AGN emit luminosities in the range $\sim 10^{42}$ - 10^{48} erg s^{-1}, up to 10^4 times more luminous than regular non-active galaxies.

In the currently accepted cosmological model, the Lambda cold dark matter scenario (ΛCDM; Riess et al., 1998), galaxy formation occurs hierarchically, starting with the formation of small clumps of gas and stars that then merge into larger structures, in a "bottom-up" manner (White and Rees, 1978; Blumenthal et al., 1984; Lee and Yi, 2013; Lee and Yi, 2017). Feedback driven by AGN (e.g., Fabian, 2012) is invoked in galaxy formation models to avoid the excessive growth of massive galaxies and drive their evolution from gas-rich starburst galaxies to the red and dead elliptical galaxies (Hopkins et al., 2008; Somerville et al., 2008; Davidzon et al., 2017; Wang et al., 2019a) observed in the local Universe. AGN are thus believed to play an important role in regulating the growth of massive galaxies (e.g., Zubovas and King, 2012; Matzeu et al., 2023).

The discovery that almost all massive galaxies have a supermassive black hole (SMBH) in their central regions (e.g., Kormendy and Richstone, 1995; Ferrarese and Ford, 2005; Ho, 2008), that the mass of the black hole is tightly correlated with the stellar velocity dispersion (e.g., Ferrarese and Merritt, 2000; Gebhardt et al., 2000), with the stellar mass (e.g., Marconi and Hunt, 2003; Häring and Rix, 2004) and with the luminosity of their host galaxy is seen as evidence of co-evolution between the SMBH and its host (e.g., Kormendy and Ho, 2013). This led to the belief that host galaxies and their central black holes grow simultaneously until they run out of gas (e.g., Archibald et al., 2002; Hopkins et al., 2006; Drouart et al., 2014; Jones et al., 2019) or the AGN expels the remaining gas from the host galaxy, terminating both star formation and black hole growth (e.g., Silk and Rees, 1998; King, 2003; Zubovas and King, 2012; King and Pounds, 2015; Koutsouridou and Cattaneo, 2022) in a process known as AGN feedback.

The impact of AGN feedback is believed to have been particularly important in the past, at redshifts ~ 2 - 3. This epoch corresponds to the density peak of luminous AGN (quasars and radio-galaxies; e.g., Hasinger et al., 2005; Richards et al., 2006; Brown et al., 2006; Rigby et al., 2015; Pan et al., 2022) and also to the peak of the star-formation rate density in the universe (e.g., Shankar et al., 2009; Sobral et al., 2013; Madau and Dickinson, 2014; Jo et al., 2021). Since AGN feedback is supposed to regulate the growth and the star formation of these massive galaxies, this appears to be the ideal epoch to study this mechanism and trace its impact in the host galaxies.

This chapter gives a brief description of the basic components of AGN (Section 1.1), and presents some of the criteria used to classify different AGN classes (Section 1.2). Then, we describe the mechanisms of AGN feedback and its importance in the evolution of AGN host galaxies (Section 1.3). This thesis will focus mainly on type 2 AGN at high redshift, thus special emphasis is given to these classes of objects (Section 1.4) and to their surrounding environment (Section 1.5).

1.1 Basic structure and geometry

The internal structure of an AGN is shown in Figure 1.1. It is believed to consist of an accreting SMBH (10^6 $M_\odot$ < M_{SMBH} < 10^{10} $M_\odot$; e.g., Ho, 2002; Natarajan and Treister, 2009) surrounded by an accretion disk, located in the nucleus of the galaxy (Shakura and Sunyaev, 1973) which is the main source of the non-thermal continuum.

At distances of ∼ 0.01 to 1 pc from the SMBH there is a broad-line region (BLR), a region under the gravitational influence of the SMBH with high gas column density (∼ 10^{23} cm^{-2}) and high velocity gas clouds (> 1000 km s^{-1}; Netzer, 2013; Netzer, 2015), that consists of a large number of small clouds with a low covering factor[1] (< 0.3; e.g., Carswell and Ferland, 1988; Peterson, 2006; Netzer, 2022). The BLR clouds are the source of the broad optical and UV emission lines (e.g., Mo et al., 2010) observed in the spectra of some AGN. The extreme electron densities ($n_e \gtrsim 10^8$ cm^{-3}; e.g., Snedden and Gaskell, 1999; Osterbrock and Ferland, 2006) prevent the emission of forbidden emission lines due to collisional de-excitation, thus permitted and semi-forbidden lines of very high critical densities are preferentially emitted in this region.

This central region of the AGN is surrounded by a dusty obscuring structure, that hides the SMBH and the BLR from transverse lines of sight (e.g., Tristram et al., 2007). The obscuring structure was believed to be shaped like a torus but there is growing evidence that it is actually a two-component structure, consisting of a dusty hollow cone-like structure, extending up to scales of hundreds of parsecs (e.g., Asmus et al., 2016; Asmus, 2019) and an equatorial dusty thin disk (Tristram et al., 2014; Stalevski et al., 2017; Hönig and Kishimoto, 2017; Hönig, 2019).

At several hundreds to thousands of parsecs from the SMBH there is a narrow-line region (NLR), a region of interstellar gas ionized by the AGN. Gas clouds in this region have low column density ($N_H \sim 10^{20-21}$ cm^{-2}) and low velocity width (FWHM < 2000 km s^{-1}) producing narrow emission lines (e.g., Padovani et al., 2017). Due to the low electron densities ($\lesssim 10^6$ cm^{-3}), in addition to permitted and semi-forbidden lines, a rich spectrum of forbidden lines is also emitted in this region (e.g., Netzer, 2013).

In some objects an extended narrow-line region (ENLR[2]) is also observed. This is a region of (often) highly ionized interstellar gas presumably photoionized by the AGN (e.g., Jones et al., 2004) that can extend for tens of kpc from the central nucleus. The

[1] Covering factor is the fraction of the sky covered by BLR clouds, as seen by the central source.
[2] Also known as extended emission line region (EELR).

ENLR is sometimes assumed to be an extension of the NLR beyond ~ 1 kpc. This value is somewhat arbitrary, given that they have similar characteristics, both regions show narrow permitted and forbidden lines and electron temperatures of the same order (e.g., Congiu et al., 2017). In high redshift AGN (z > 2) extended emission line regions can be seen in Lyα, and are usually known as Lyα nebulae.

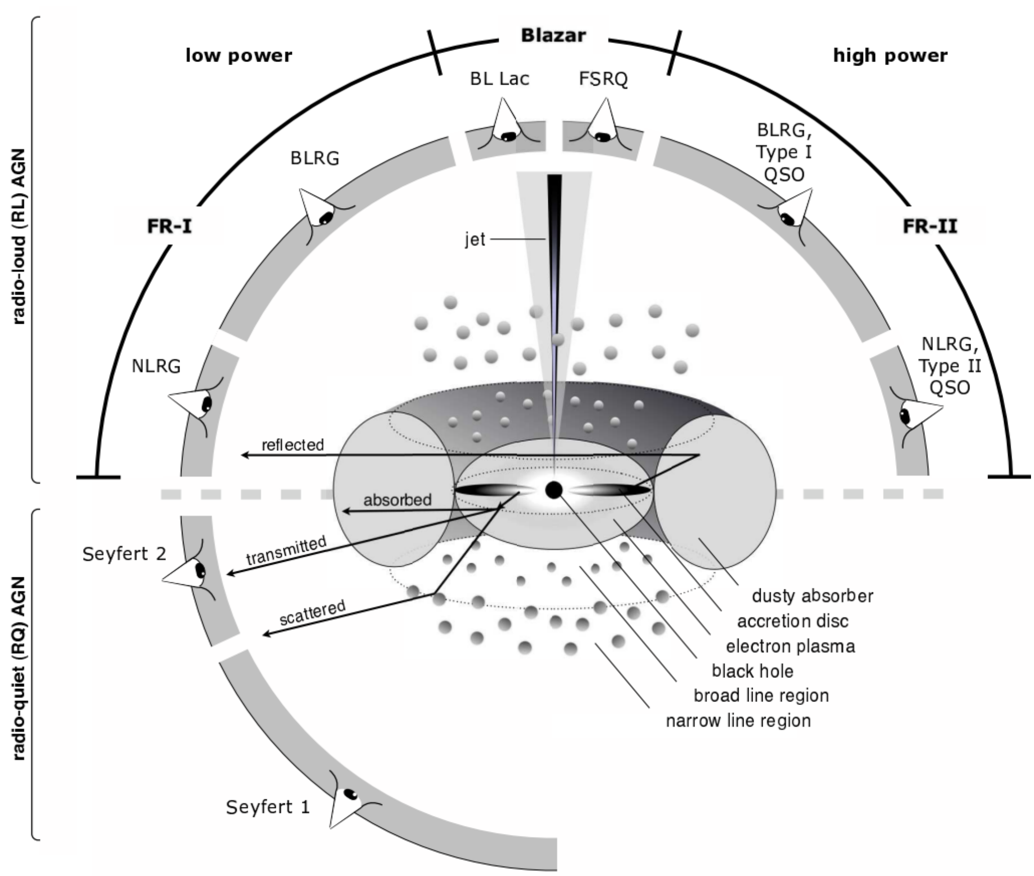

Figure 1.1: Illustration of the unified model, showing different classes of AGN. An accretion disk surrounds the central SMBH. Clouds orbiting outside the disk produce broad emission lines, in the BLR. A thick, dusty torus surrounds the BLR. Much farther from the SMBH, narrow-lines are produced in clouds of the narrow-line region. In some AGN, radio jets emanate from a region close to the SMBH. From Beckmann and Shrader (2012).

In radio-loud sources, which make up about 10 to 20% of the AGN population, relativistic radio-jets are launched from the region near the SMBH (e.g., Blandford and Rees, 1974; Urry and Padovani, 1995; Hada et al., 2013; Blandford et al., 2019).

1.2 AGN taxonomy

Historically, AGN have been classified according to their observed properties in the spectral band in which they were discovered. This resulted in a considerable number of observationally-driven, and somewhat arbitrary, classes and sub-classes (for a complete list of AGN classes see Padovani et al., 2017) including the classical: Seyfert galaxies, radio galaxies, quasars, and blazars. In general, the various classes of AGN have been divided according to three properties: orientation, AGN luminosity and degree of radio loudness (e.g., Tadhunter, 2008):

- **Orientation**

  The unified model developed by Antonucci (1993) and Urry and Padovani (1995) attempts to explain many of the differences in the observed characteristics of AGN as an effect of orientation. In other words, much of the diversity in observed AGN properties is the result of a small number of AGN-types being observed at a diversity of viewing angles (see Figure 1.1). In this model the inner part of the AGN (accretion disk and BLR) is surrounded by an obscuring structure (assumed to be a torus) that hides the view of the central region along certain observing angles, creating the dichotomy between type 1 and type 2 AGN.

  In type 1 AGN (type 1 quasars, Seyfert 1 galaxies, broad-line radio galaxies) the central engine and the broad emission line regions are unobscured and a bright, non-stellar central source is visible at all wavelengths with little contamination by stellar light. These objects exhibit the superposition of both broad (BLR; $\gtrsim 10^3$ km s^{-1}) and narrow (NLR; $\sim 10^2$ km s^{-1}) emission line spectra (see Figure 1.2).

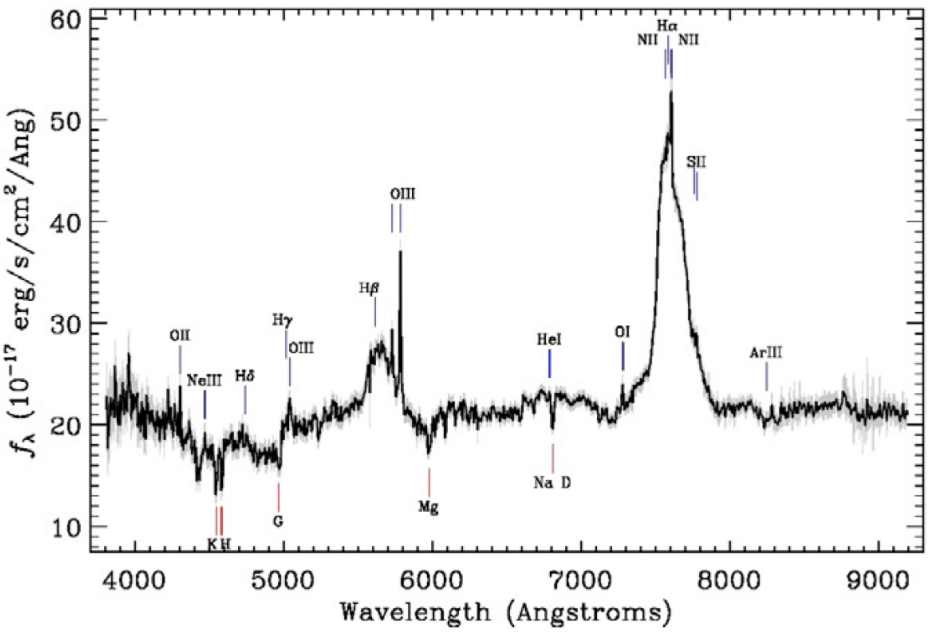

Figure 1.2: Spectrum of a Seyfert 1 galaxy showing both broad and narrow emission lines. Plot taken from Mickaelian et al. (2021).

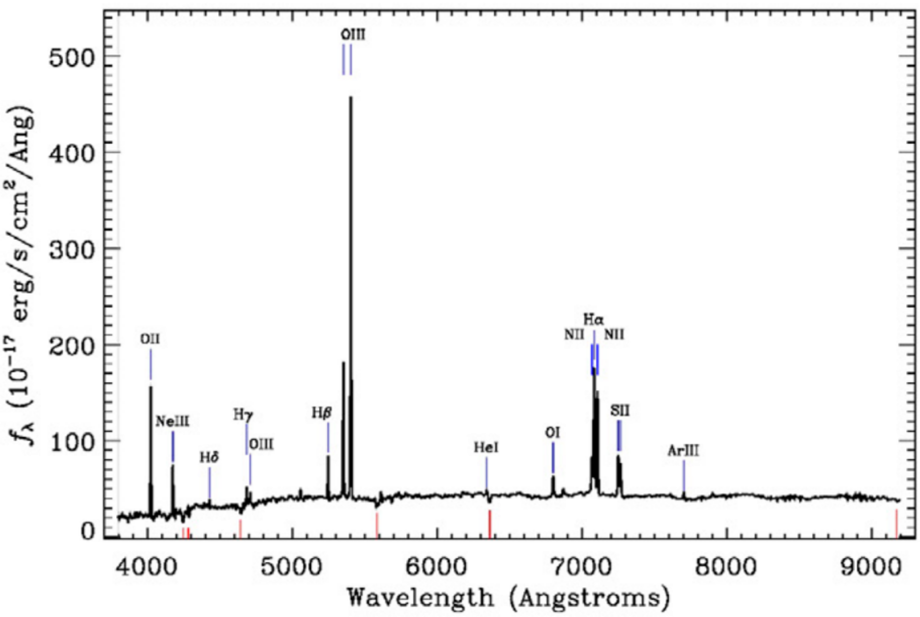

Figure 1.3: Spectrum of a Seyfert 2 object showing only narrow emission lines. Plot taken from Mickaelian et al. (2021).

Type 2 AGN (Seyfert 2s, narrow-line radio galaxies, type 2 quasars) are viewed relatively edge-on, in such manner that the central engine and the BLR are obscured and only the narrow emission lines are directly visible as shown in Figure 1.3.

- **Radio loudness**

The division between radio-loud and radio-quiet was among the earliest AGN classifications to be made. In this classification scheme the main difference between radio-loud and radio-quiet AGN is the presence of relativistic jets that dominate the radio emission (e.g., Kellermann et al., 1989; Mullin et al., 2008). This division has been defined in different ways, using the ratio of radio (5 GHz) to optical (B-band) luminosity (R = f_{5GHz} / f_{4400}; Schmidt, 1970; Kellermann et al., 1989), with a threshold at R = 10, such that objects with R > 10 are classified as radio-loud and sources with R < 10 as radio quiet, or using the radio luminosity, with the threshold at $L_{5GHz} \sim 10^{25}$ W Hz^{-1} sr^{-1} (Miller et al., 1990).

In general, around 10 to 20% of optically selected AGN are radio-loud (e.g., Kellermann et al., 1989; Ivezić et al., 2002; White et al., 2007) and the remaining population is radio-quiet or radio-intermediate (e.g., Barvainis et al., 2005; D'Amato et al., 2022). While the name can be misleading, radio-quiet sources are not radio silent: their radio emission is about 10^3 times weaker than in their radio-loud counterparts (e.g., Miller et al., 1993). The origin of the radio emission in radio-quiet objects is still under debate, the most probable mechanisms being non-thermal emission due to the nuclear activity or ongoing star formation in the host galaxy (e.g., Herrera Ruiz et al., 2016; Zakamska et al., 2016; Wang et al., 2023a; Condon et al., 2013; Bonzini et al., 2013; Stacey et al., 2019; Radcliffe et al., 2021; Perger et al., 2019; Retana-Montenegro, 2022). Radio-quiet AGN consist mainly of radio-quiet quasars and Seyfert galaxies, while the radio-loud population consists of radio galaxies, radio-loud quasars and Blazars.

Fanaroff and Riley (1974) divided the radio-loud population into two classes, Fanaroff-Riley (FR) type I and FR type II, based on their radio morphology. FR I are dominated by emission from the compact core ("edge-darkened"), and show diffuse radio emission in the outer regions (see Figure 1.4). FR II are highly luminous, have radio lobes with prominent hotspots and bright outer edges ("edge-brightened").

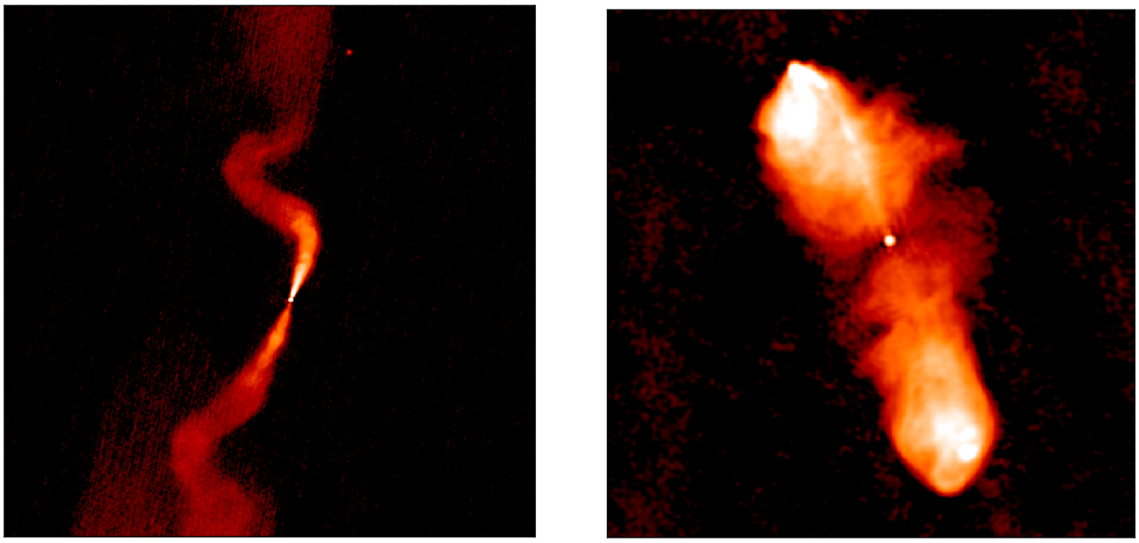

Figure 1.4: Left: The FR I source 3C 31, whose radio emission is dominant in the core; Right: The FR II source 3C 98, with lobe-dominated radio emission. Images taken from Hardcastle and Croston (2020).

These two classes also show differences in radio power: FR II are powerful radio sources, with $L_{1.4GHz} \sim 10^{25}$ W Hz^{-1}, while FR I usually have lower radio power.

It has been suggested that the difference between FR I and FR IIs arises from differences in the accretion mode of their SMBHs (e.g., Ghisellini and Celotti, 2001; Mingo et al., 2014), power of the jet (e.g., Gendre et al., 2013), or environment of the AGN host galaxies (e.g., Gendre et al., 2010; Gendre et al., 2013; Croston et al., 2019; Yates-Jones et al., 2021). This classification has been widely adopted and even though the exact conditions needed to produce a FR I or FR II source are still not completely understood (e.g., Bicknell et al., 2004) this radio-loud classification scheme is still useful today (e.g., Mingo et al., 2019; Vaddi et al., 2019; Fanaroff et al., 2021).

- **Blazars** ("blazing quasi-stellar radio sources")

  These sources are radio loud AGN that show variability on timescales of one day or less at all wavelengths. The axis of the relativistic jets is believed to be closely aligned with the line of sight of the observer (see Figure 1.1).

  They have been divided in two classes: BL-Lac and optically violently variables (or OVVs). BL-Lac objects are strong radio emitters, with highly variable optical and X-ray emission. Their optical and X-ray emission is highly polarized and their spectra do not show emission or absorption lines: they are featureless power-laws. OVVs are variable optical sources, with polarized optical light that emit broad emission lines similar to the ones observed in quasars.

- **Luminosity**

  According to luminosity, spectral properties and appearance AGN have been divided into the following types:

  - **Seyfert galaxies**

    First identified in 1943 by Carl Seyfert (Seyfert, 1943) these objects are moderate luminosity AGN ($L_{bol} \sim 10^{43-45}$ erg s^{-1}) that emit high-excitation emission lines.

    Seyfert galaxies are divided into different categories based on the characteristics of their spectra, ranging from Seyfert 1 to Seyfert 2. Seyfert 1 galaxies display broad permitted lines, such as Hα and Hβ with FWHM ~ 1000 - 5000 km s^{-1} and narrower forbidden lines, such as [O III] $\lambda\lambda$4959,5007 and [N II] $\lambda\lambda$6548,6583 with FWHM ~ 500 km s^{-1}. In Seyfert 2 galaxies both permitted and forbidden lines show narrow velocity widths. There are also intermediate or transition Seyfert categories (such as Seyfert 1.5, Seyfert 1.9; e.g., Osterbrock, 1977; Osterbrock, 1981) that show varying levels of broad component emission, where the higher the type of the Seyfert, the more obscured is the central region.

- **Quasars**

  Quasars were first identified in the radio waveband (Schmidt, 1963) and later in the optical regime (Sandage, 1965). The term quasar is a portmanteau representing the term 'quasi-stellar radio source', and was assigned to quasars due to their appearance as point-like objects in the center of their host galaxies.

  Analogously to Seyfert galaxies, quasars have also been divided into type 1 and type 2 depending on the presence or absence of broad emission lines in their spectra. Type 1 quasars are the most optically luminous type of AGN with bolometric luminosities of $L_{bol} \sim 10^{45-48}$ erg s^{-1} (e.g., Runnoe et al., 2012; Duras et al., 2017), outshining their host galaxy, and making the host extremely difficult to detect. The spectra of type 1 quasars are similar to those of Seyfert 1 galaxies; the fundamental difference between these two types of objects lies in their bolometric luminosity (Schmidt and Green, 1983; Soifer et al., 1987). Due to their high luminosity across the electromagnetic spectrum, quasars can be detected across a vast range in redshift (up to $z > 7$; e.g., Bañados et al., 2018; Wang et al., 2021a).

  In type 2 quasars, the central regions are hidden, and their emission spectrum shows only narrow lines. These objects are one of the foci of this thesis and they are briefly described in section 1.4.

  Quasars have also been divided into radio-quiet (also known as quasi-stellar objects or QSO) and radio-loud (quasi-stellar radio sources) based on the presence or absence of powerful radio jets. These two classes share similar optical properties.

- **Radio galaxies**

  Radio galaxies were initially identified in radio surveys and later identified with optical sources that revealed that they are usually hosted by massive elliptical galaxies (e.g., Matthews et al., 1964; Dunlop et al., 2003). They emit relatively strong radio emission ($P_{1.4GHz}$ >10^{23} W Hz^{-1}) associated with the radio jets, and their optical spectrum is similar to those of Seyfert galaxies, showing strong emission lines. They have been divided into broad- and narrow-line radio galaxies (BLRGs and NLRGs, respectively) depending on their spectra. BLRGs possess an emission spectrum similar to those of Seyfert 1 galaxies, with broad permitted lines and narrower forbidden lines, and NLRGs show an optical spectrum comparable to Seyfert 2s, showing only narrow emission lines.

  Based on their radio morphology, radio galaxies have been further divided into the FR I ("edge-darkened") and FR II classes ("edge-brightened") described above.

- **LINERs** (Low-Ionization Nuclear Emission line Regions)

  These objects emit a spectrum with strong, low-ionization lines like those of Seyfert 2 galaxies, and weak high-ionization lines. They have luminosities in the range 10^{39-42} erg s^{-1} and are the most common type of AGN in the local Universe (e.g., Ho, 2008; Ricci et al., 2014).

These are some of the classification criteria that have led to the complex family of different AGN types. The unification scheme was an attempt at unifying the different classes into a common model that could represent the basic properties of all AGN. However, trying to find a common model to explain all the different AGN classes has proven to be a challenging task and new classification criteria are still being presented (e.g., Netzer, 2015; Padovani, 2016; Ogawa et al., 2021).

Although different classes of AGN might present different characteristics, their basic structure presented in Figure 1.1 should be representative of the overall structures of AGN needed for this work.

1.3 Role of AGN in galaxy evolution: feedback

AGN feedback is the process by which the energy generated by accretion onto the SMBH interacts with the interstellar medium (ISM) of the host galaxy, potentially influencing its evolution (e.g., Heckman and Best, 2014).

This mechanism is required in models of galaxy formation to explain why the most massive halos show low star formation efficiency (see Figure 1.5; e.g., Somerville et al., 2008; Behroozi et al., 2013), the low rate of gas cooling observed in galaxy clusters (Fabian, 1994; Brüggen and Kaiser, 2002) and the bright end cut-off in the luminosity function of galaxies (Benson et al., 2003; Croton et al., 2006).

Negative feedback is believed to play a major role in the evolution of massive galaxies by regulating their growth (both in mass and size), star formation and chemical enrichment. Cosmological simulations suggest that in low mass halos stellar feedback is capable of regulating the growth of galaxies by reducing the efficiency of star formation (e.g., Li et al., 2018). However, in the more massive systems ($M_* \gtrsim 10^{11}$ $M_\odot$; e.g., Harrison, 2017; Förster Schreiber and Wuyts, 2020) the energy released by stellar feedback is not sufficient and AGN feedback is required in order for models to reproduce the observations (e.g., Croton et al., 2006; Bower et al., 2006; Davé et al., 2019; Vogelsberger et al., 2020; Rosito et al., 2021) as illustrated in Figure 1.5.

AGN feedback is thus believed to be responsible for heating gas or expelling it from the galaxy in gaseous outflows (e.g., Di Matteo et al., 2005; Tortora et al., 2009; Harrison et al., 2014; Cresci et al., 2015a; Vayner et al., 2017), quenching star formation and limiting galaxy growth (Springel et al., 2005; Hopkins and Beacom, 2006; Le Fèvre et al., 2019), especially in the most massive dark matter halos. Interestingly, with the discovery of AGN-driven outflows in some dwarf galaxies ($M_* < 10^{10}$ $M_\odot$; e.g., Manzano-King et al., 2019), recent works suggest that AGN-driven outflows may also be important in low mass halos (e.g., Dickey et al., 2019; Aravindan et al., 2023).

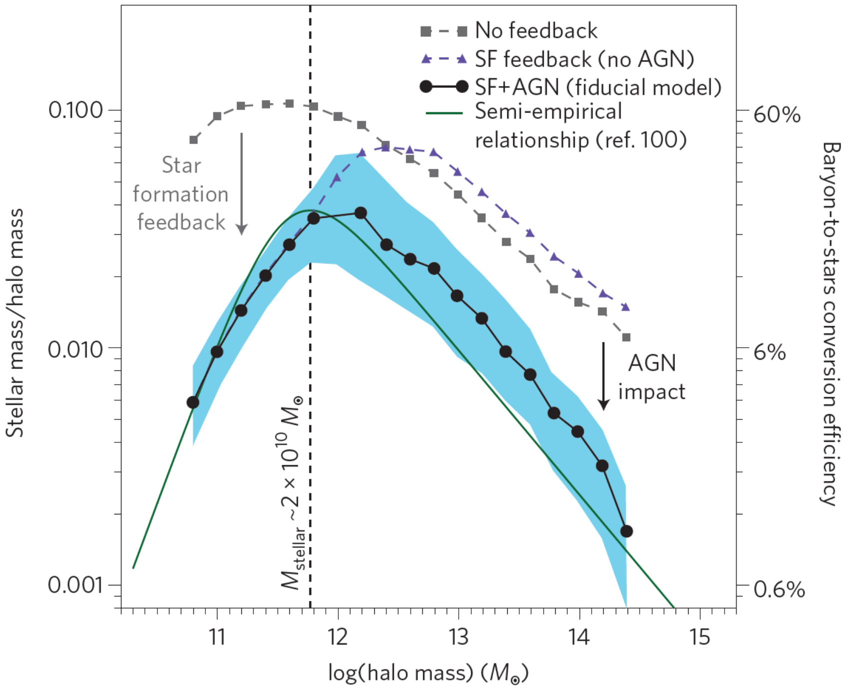

Figure 1.5: Figure 1 in Harrison (2017). Stellar mass to halo mass ratio as a function of halo mass for three different runs of a simulation and the semi-empirical relationship (Moster et al., 2013). The right y-axis shows the efficiency for turning baryons into stars. Harrison (2017) used the models developed by Somerville et al. (2008) to simulate cases assuming star formation induced feedback (triangles), AGN and star formation feedback (circles) and no feedback (squares). The shaded blue region shows the 16th and 84th percentiles of the fiducial model that includes feedback from AGN and star formation.

AGN inject large amounts of energy into the surrounding medium; this energy can be released in the form of mechanical energy, which is usually called radio or jet mode feedback, or in the form of radiation, the so-called radiative or quasar-mode feedback. Radiative mode feedback has been linked to high luminosity AGN, those accreting close to the Eddington limit[3] ($\lambda_{Edd} \gtrsim 1\%$; e.g., Heckman and Best, 2014). Radiative AGN

[3]The Eddington luminosity of the AGN is the maximum luminosity at which there is balance between

release most of their energy through accretion disk winds or radiation pressure. Resulting outflows are expected to be powerful enough to heat or expel gas from the host galaxy limiting the amount of gas available to form stars (e.g., Moe et al., 2009; Hopkins and Elvis, 2010; Cano-Díaz et al., 2012; Maiolino et al., 2012; Costa et al., 2018). Radiative AGN are usually found in star forming galaxies with a young stellar population (e.g., Hickox et al., 2009; Hernán-Caballero et al., 2014; Harrison, 2017); they are luminous in several wavelength bands (X-rays, optical, infrared and sometimes in radio) and are somewhat rare among the galaxy population. Recent works have shown that in addition to radiatively-driven winds, some highly accreting radio-quiet AGN also possess radio-jets capable of driving outflows (e.g., Jarvis et al., 2019; Girdhar et al., 2022; Singha et al., 2023).

Radio mode feedback has been associated with AGN that have low accretion rates (e.g., Hickox et al., 2009). They are radiatively inefficient compared to radiative-mode AGN and the radio jets are the main source of energy. In this mode, the AGN releases its energy in a kinetic form via radio-jets. As the radio-jets propagate outwards, they shock-heat the ambient gas, preventing radiative cooling and inhibiting star formation, thus limiting the stellar mass of the host galaxy (e.g., Best et al., 2006; Croton et al., 2006; Somerville et al., 2008; Fabian, 2012).

The interaction between the radio jets and the ISM of the host galaxy can also drive outflows (e.g., Villar-Martín et al., 2003; Humphrey et al., 2006; Humphrey et al., 2008a; Morganti et al., 2013; Santoro et al., 2020; Venturi et al., 2021). Radio-mode AGN are bright radio emitters usually hosted by extremely massive elliptical galaxies ($M_* \sim 10^{11-12}$ $M_\odot$; e.g., Harrison et al., 2014). In the local universe they frequently show an old stellar population. Due to the differences between radiative and radio AGN, it has been suggested that these two types of AGN are in different evolutionary stages or have different accretion mechanisms (e.g., Harrison, 2017).

In order to confirm the presence and impact of negative AGN feedback on the massive

the radiative force and the gravitational force in the accretion disk. Beyond this limit, radiation pressure will overcome gravity, and material outside the SMBH will be driven away instead of falling inwards.

galaxy population, a large number of observations has been made. However, the results are far from clear. Some observations show that gaseous outflows are confined to the central regions (r $\lesssim$ 1 kpc; e.g., Villar-Martín et al., 2014; Villar-Martín et al., 2016; Salvestrini et al., 2022; Winkel et al., 2023), suggesting that feedback is not very efficient at removing gas from their hosts; other observations show that AGN feedback has no significant impact on the evolution of the host galaxies (e.g., Shangguan et al., 2018; Scholtz et al., 2020; Smirnova-Pinchukova et al., 2022; Molina et al., 2022). A large number of active galaxies show AGN-driven outflows extending from tens of pc to kpc scales and with velocities of hundreds of km s^{-1} (e.g., Villar-Martín et al., 2014; Karouzos et al., 2016; Bischetti et al., 2019; Herrera-Camus et al., 2020; Wylezalek et al., 2020; Salvestrini et al., 2022; Winkel et al., 2023; Vayner et al., 2023). However, in these cases, the long-term impact of the feedback mechanism is yet to be determined since both observations and simulations show that only a fraction of the outflowing gas is capable of escaping the galaxy (e.g., Fluetsch et al., 2019), with the remaining gas falling back into it (e.g., Arribas et al., 2014; Xu et al., 2023).

While much of the literature on AGN feedback concerns negative feedback, there are also observations that show positive feedback, i.e. feedback that triggers star formation in the host galaxies (e.g., Dey et al., 1997; Klamer et al., 2004; Cresci et al., 2015b; Maiolino et al., 2017; Gallagher et al., 2019; Venturi et al., 2023).

As we can see, the impact that outflows have on the evolution of the host galaxy are far from clear, and a deeper understanding of feedback processes in active galaxies is needed. At low redshifts, most of the stellar components of massive galaxies are already formed, suggesting that AGN feedback must have had a greater impact at earlier epochs. Star formation and black holes reached their peak activity at z ~ 1 - 3 (see Figure 1.6; e.g., Shankar et al., 2009; Seymour et al., 2011; Madau and Dickinson, 2014; Drouart et al., 2014; Podigachoski et al., 2015; Wang et al., 2019b; Bellstedt et al., 2020) so it is likely that AGN feedback was also stronger at this time, making it the ideal epoch to study this mechanism and trace the impact of the nuclear activity in the host galaxy.

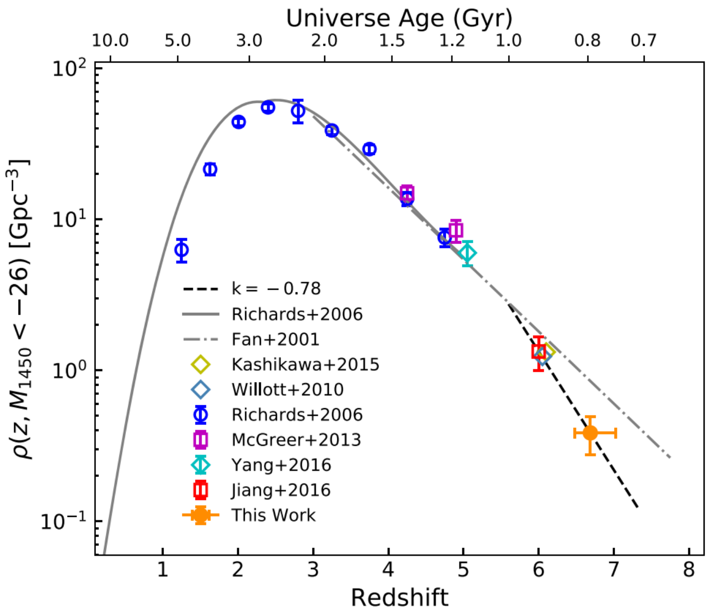

(a)

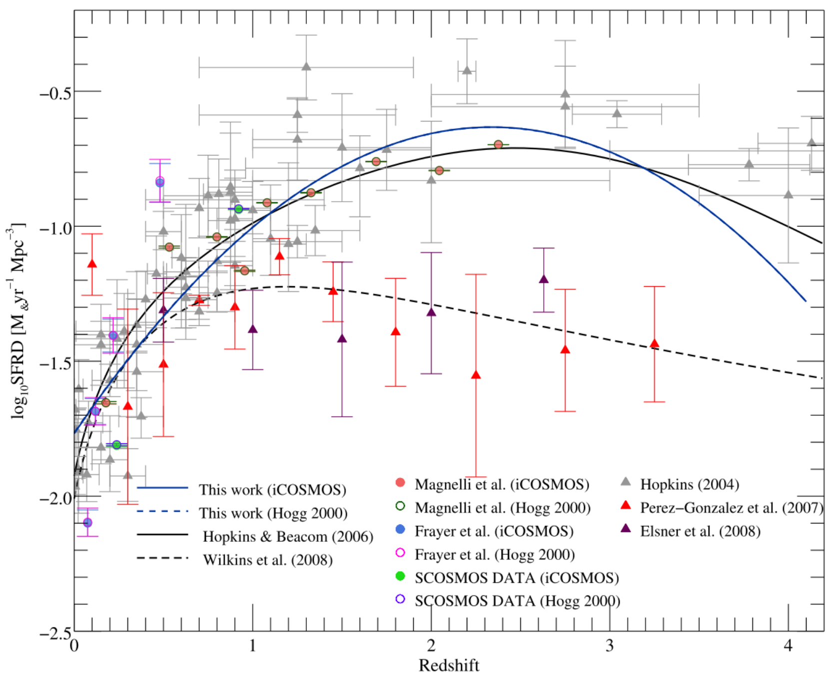

(b)

Figure 1.6: (a) Spatial density of luminous quasars across cosmic time showing a rapid evolution in the early universe and a peak at z ~ 2 - 3 (Figure 10 in Wang et al., 2019b); (b) Evolution of the star formation rate densities (SFRDs) across cosmic time. The blue solid line represents SFRD measurements obtained using infrared luminosities that reach a peak at z ~ 2.2 - 2.4 and show a steep decline from z = 1 to 0 (Figure 3 in Jo et al., 2021).

According to cosmological models, AGN feedback plays a major role in galaxy evolution. These results need to be confirmed by observations, however, as aforementioned the observations are not clear, especially because there are several difficulties when studying this process. The key issues and challenges related to the study of AGN feedback are summarized in Figure 1.7 and further discussed in Harrison et al. (2018).

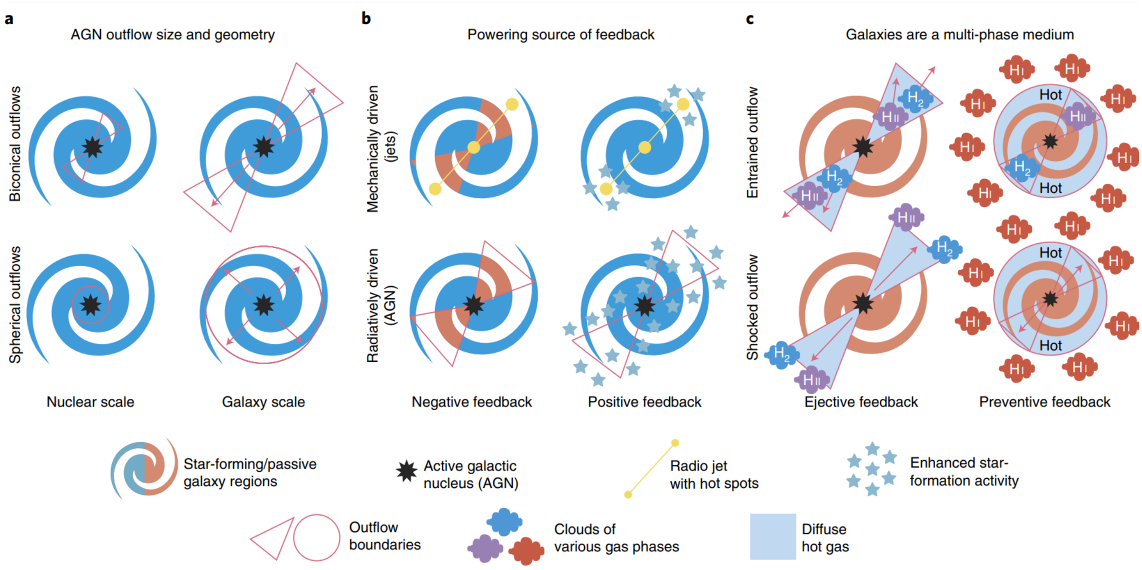

Figure 1.7: Schematic representation of key open issues related to AGN feedback: a) difficulty in constraining the size and geometry of the outflows and how much gas they affect; b) the powering source (radiation or shocks) is not always clear nor is the effect of the feedback process (positive or negative); c) lack of observations showing the impact of the outflows in the different gas phases. Fig. 1 in Husemann and Harrison (2018).

In order to understand the impact of AGN feedback in the evolution of AGN host galaxies the mass, size, geometry and energetics of the outflows need to be accurately measured. Furthermore, these measurements need to take into account the different outflow phases and different spatial scales (see also Figure 1.8). This would be important for facilitating a germane comparison between observations and model predictions, since models typically consider the entirety of the outflowing material, whereas observations typically probe only some gas phases.

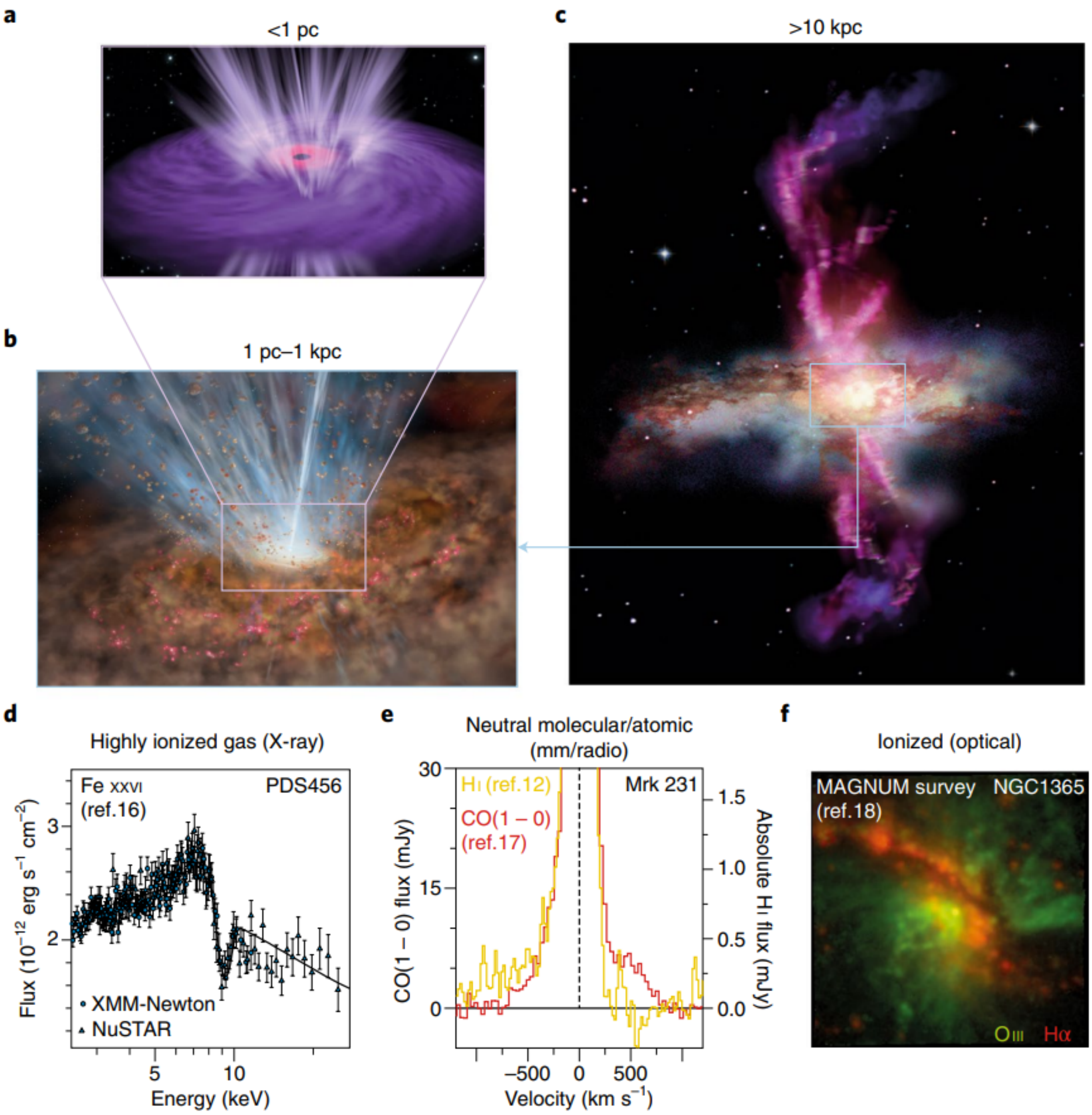

Figure 1.8: Figures (**a**) to (**c**) present an artistic view of AGN-driven outflows in different gas phases: (**a**) the AGN induces an outflow in the inner region (< 1 pc); (**b**) the outflowing gas propagates through the ISM (1 pc - 1 kpc); (**c**) and reaches the outer regions of the host galaxy (> 10 kpc). Panels (**d**) to (**f**) show some of the observational evidence of multiphase outflows: (**d**) an ultrafast (∼ -0.25c) ionized gas wind expelled from the inner accretion disk in PDS 456; (**e**) gas outflows extending for a few hundreds of parsecs observed in molecular and atomic gas phases in Mrk 231; (**f**) a double conical outflow of ionized gas propagating from the central region up to a few kiloparsecs in NGC 1365. Figure 1 in Cicone et al. (2018).

Up to now, most studies have focused on only one component of the outflow, such as the ionized gas (e.g., Villar-Martín et al., 2011; Villar-Martín et al., 2014; Xu et al., 2023) or the cold gas phase (e.g., Cicone et al., 2015; Fluetsch et al., 2019) and only a small number of works have been able to study different gas phases in a single galaxy (e.g., Morganti et al., 2015; Herrera-Camus et al., 2019; Herrera-Camus et al., 2020).

Difficulties also exist in determining the kinetic energies involved, to understand the geometry and mass of the observed outflows (e.g., Harrison, 2017; Nesvadba et al., 2017a) and in constraining their size (e.g., Villar-Martín et al., 2016). Understanding AGN feedback is crucial but this phenomenon is extremely complex, involving different mechanisms and different gas phases (coronal, ionized, neutral, molecular) which are distributed across different spatial scales (from sub-pc in the X-ray up to 10 - 20 kpc in the ionized and cold molecular gas phases) and require different observing techniques. Some of the required techniques will only become available with upcoming facilities (see Cicone et al., 2018).

1.4 Type 2 high-z active galaxies

In this thesis we focus on type 2 luminous AGN at z ~ 2 - 4, both radio-loud (narrow-line radio galaxies) and radio quiet (type 2 quasars). The advantage of selecting type 2 systems is that the nuclear obscuring structure acts as a "natural coronograph" that obscures the central source (the accretion disk and BLR). This allows the nuclear environment and the host galaxy to be studied more accurately, since the dominant glare of the nuclear point source that can hinder studies of type 1 quasars and BLRGs is absent.

- **Type 2 quasars**

  Type 2 quasars (or QSO2s) are luminous AGN whose accretion disk and BLR are obscured by a dusty structure. The quasar continuum and broad emission lines are hidden and they possess only narrow emission lines in their spectra. These objects are the high-luminosity analogs of Seyfert 2 galaxies, with narrow permitted and forbidden lines (FWHM <1000 km s^{-1}), predicted by unification models. QSO2s are fainter in optical bands than type 1 AGN of the same intrinsic luminosity, their continuum emission is often dominated by the host galaxies and they lack powerful radio emission, characteristics that have delayed their detection. Significant numbers of QSO2s were identified with the advent of the Sloan Digital Sky Survey (SDSS). At lower redshifts ($z < 1$) more than 1000 candidates have been found using the [O III] λ5007 emission line (Zakamska et al., 2003; Zakamska et al., 2004; Reyes et al., 2008; Yuan et al., 2016). At higher redshifts ($z > 2$) their discovery is more recent, and based on the presence of strong and narrow (< 2000 km s^{-1}; Alexandroff et al., 2013; Ross et al., 2015) high ionization lines in their UV spectra, such as Lyα and C IV .

- **Narrow line radio galaxies**

Narrow line radio galaxies are radio-loud AGN, that emit large-scale radio jets driven by AGN activity. The jets extend from several hundred kiloparsecs to megaparsecs (e.g., Dabhade et al., 2017) from the central region and show strong radio emission over several orders of magnitude. Due to the strength of their radio emission, radio galaxies can be observed to very large distances ($z \sim 5$; van Breugel et al., 1999) and have long acted as beacons for tracing distant galaxies.

The canonical structural model of powerful radio galaxies was developed by Blandford and Rees (1974) and Scheuer (1974). A representation of the global characteristics is shown in Figure 1.9. In this "beam model", collimated radio-jets emerge from the central region at supersonic speeds until they terminate in hotspots, where electrons are accelerated by strong shocks (e.g., Blandford and Rees, 1974; Georganopoulos and Kazanas, 2003). As the jet terminates its flow gets thermalized and flows back towards the host galaxy, inflating a cocoon of shocked material that surrounds the jets (Longair et al., 1973; Blandford and Rees, 1974; Scheuer, 1974).

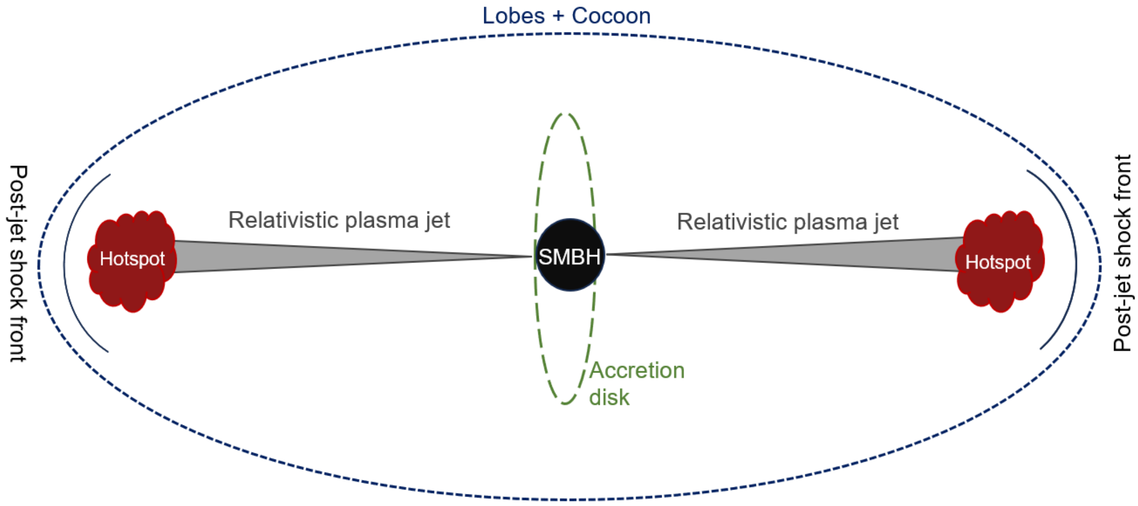

Figure 1.9: Representation of the global characteristics of radio galaxies first put forward by Blandford and Rees (1974) and Scheuer (1974).

1.5 The ISM and CGM of high-z active galaxies

Our goal is to study the interplay between AGN activity and the host galaxy thus we will briefly describe the interstellar and circumgalactic mediums, as well as the Lyman-α λ1216 (hereafter Lyα) nebulae that trace these gaseous environments. These components are of crucial importance to understand the evolution of the host galaxies.

The ISM is an inhomogeneous multi-phase medium, composed by cold (T $\sim$ 10 - 100 K), warm (T $\sim$ 10^4 K; e.g., NLR, ENLR, H II -regions) and hot (T $\gtrsim$ 10^5 K) gases (e.g., Field et al., 1969; McKee and Ostriker, 1977). As discussed earlier, feedback can have a significant effect on the morphology, kinematics and ionization properties of the ISM.

Between the ISM and the intergalactic medium (IGM), still within the virial radius of the dark matter halo of a galaxy, exists the circumgalactic medium (CGM) extending to distances of hundreds of kpc from its nucleus ($\lesssim$ 300 kpc; e.g., Shull, 2014; Tumlinson et al., 2017).

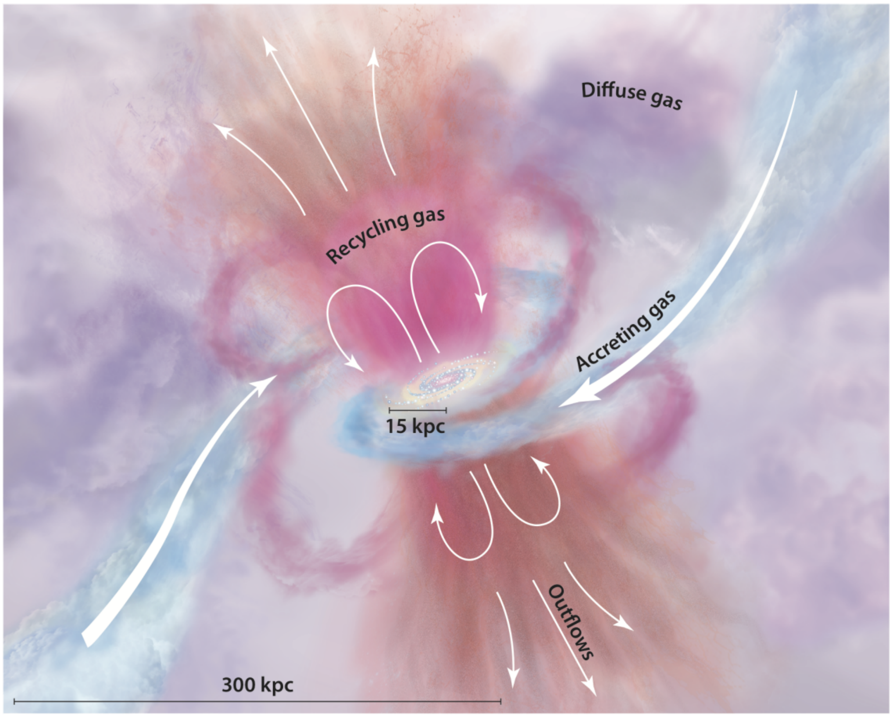

Figure 1.10: Cartoon view of the CGM created by Tumlinson et al. (2017). Filamentary accretion from the IGM (blue) feeds the galaxy's red central region (bulge and blue gaseous disk). Outflowing gas emerges from the disk (pink and orange colors) and gas that was ejected in earlier phases is recycled. Purple tones show the diffuse gas halo including a mixture of gas that has been accreted and subsequently ejected over the galaxy's lifetime.

Observations have shown that the CGM, just like the ISM, is a multi-phase medium. The hot gas phase is observed in X-ray emission (e.g., Anderson et al., 2013; Anderson et al., 2016), the warm gas phase is observed in the UV and optical range (e.g., Cai et al., 2017; Arrigoni Battaia et al., 2019), and the cold gas phase has been detected through the observation of fast and massive (v >1000 km s^{-1}; $\sim 10^{9-10} M_\odot$) outflows of cold and dense molecular gas (e.g., Sturm et al., 2011; Dasyra and Combes, 2012; Veilleux et al., 2020).

The CGM regulates the exchange of gas between a galaxy and the IGM, controlling the gas supply of galaxies and acting as a reservoir of fuel for star formation and the central

SMBH. This medium is composed by a mixture of gas that has been expelled from the galaxy through AGN or stellar feedback events (e.g., Biernacki and Teyssier, 2018), gas accreted from the IGM through filamentary flows of cold gas (e.g., Dekel et al., 2009; Danovich et al., 2015; Bennett and Sijacki, 2020) and gas accreted via merger events (e.g., Riechers et al., 2008; Hani et al., 2018; Hani et al., 2018). Thus, all the processes that occur within a galaxy (feedback, mergers, accretion, inflow and outflow) leave an imprint in the CGM, making it a key component to study its evolution. Figure 1.10 presents a cartoon view of the various gas phases present in the CGM.

The CGM has, generally, been studied using absorption lines in the spectra of quasars (e.g., Fynbo et al., 1999; Adelberger et al., 2003; Fynbo et al., 2003; Giavalisco et al., 2011; Bouché et al., 2016), because its diffuse nature and resulting low surface brightness makes it challenging to observe in emission.

1.5.1 Lyα nebulae

The detection of extended Lyα nebulae surrounding AGN (e.g., Vernet et al., 2001; Villar-Martín et al., 2003; Reuland et al., 2003; Villar-Martín et al., 2007b; Hennawi et al., 2015; Swinbank et al., 2015; Borisova et al., 2016; Villar-Martín et al., 2018; Lusso et al., 2019; Arrigoni Battaia et al., 2019; Marques-Chaves et al., 2019) was a step forward in this area, allowing us to directly study the warm gas in the CGM. These nebulae extend for tens to hundreds of kpc, into the CGM of the host galaxies and in some cases into the IGM (e.g., Cantalupo et al., 2014), making them useful tracers of the properties of the gas in these regions (e.g., Miley et al., 2006; Cantalupo et al., 2014; Cai et al., 2019; Costa et al., 2022). They provide insights into the evolution of massive galaxies by mapping the exchange of gas between a galaxy and the surrounding environment, and into the interaction between the AGN and its host galaxy in the late stages of the formation of the galaxy.

The Lyα emission line arises when an electron in a hydrogen atom spontaneously decays from the first excited level to the ground state (n = 2→1, where n is the principal quantum number). A photon of energy 10.2 eV, or wavelength λ = 1215.67 Å is emitted, in a transition usually referred to as Lyα line (Lyman, 1906). In the case where a free electron recombines with a hydrogen ion, Lyα is formed as a cascade of transitions as an excited hydrogen atom de-excites to its ground state (see Figure 1.11).

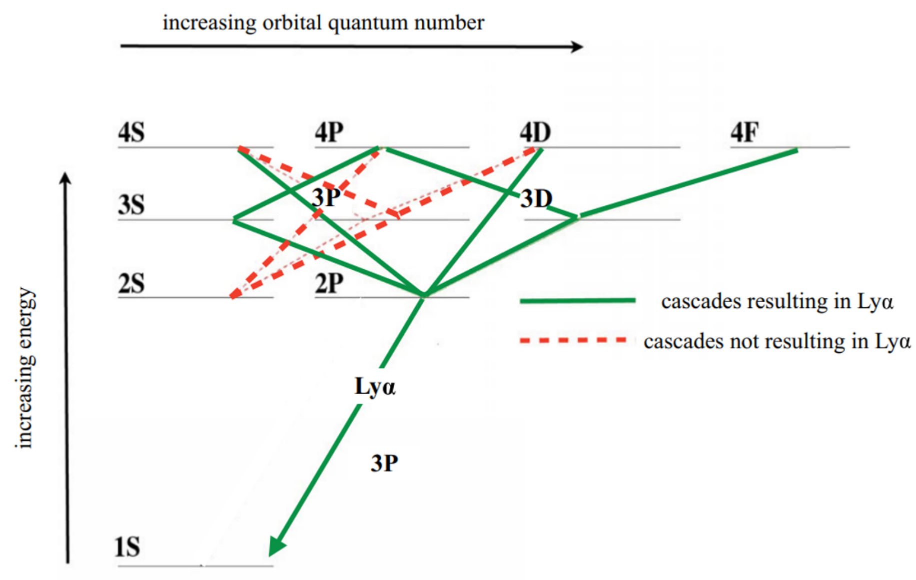

Figure 1.11: Scheme of the energy levels of a hydrogen atom. Green lines show cascades that result in the emission of a Lyα photon and dotted red lines show cascades that do not result in the emission of a Lyα photon. Figure taken from Dijkstra (2014).

Several physical processes other than recombination can also give rise to Lyα photons, amongst them scattering and collisional excitation. We will describe these processes in more detail below, in the context of Lyα nebulae.

Partridge and Peebles (1967) first argued that Lyα should be very bright in primeval galaxies due to the large abundance of ionizing photons from young stars. Lyα emission was also expected as a result of the galaxy formation process (Haiman et al., 2000): as a galaxy forms, large quantities of gas infall into the gravitational potential well of its dark matter halo, this gas is heated by the halo potential, and thermal energy is dissipated by collisional excitation of the Lyα transition. As a result of gas cooling, a low-surface brightness Lyα nebula is expected (Haiman et al., 2000; Fardal et al., 2001). In the presence of an AGN, this Lyα emission could be enhanced due to the ionizing photons radiating from the AGN, and produce an extended Lyα "fuzz" (Rees, 1988; Haiman and Rees, 2001). These studies highlighted the importance of Lyα as a tool to detect primeval galaxies.

After these results, many efforts were performed to reveal extended Lyα around high-z quasars. The first surveys were not very successful and only a handful of sources had been discovered by the 1990s (e.g., Steidel et al., 1991; Bremer et al., 1992). The first extended Lyα nebulae were detected surrounding high redshift radio galaxies (HzRGs; e.g., McCarthy et al., 1990; Eales et al., 1993; McCarthy et al., 1987b). These galaxies were initially found due to their strong radio emission, but follow up spectroscopic studies detected strong Lyα emission. As more HzRGs were discovered in the 1990s (e.g., Röttgering et al., 1994), it became clear that Lyα nebulae were present in almost all of them (e.g., van Ojik et al., 1996; Reuland et al., 2003; Miley and De Breuck, 2008).

Nowadays, we know that extended Lyα emitting regions are ubiquitous among HzRGs (e.g., McCarthy et al., 1990; Heckman et al., 1991; Pentericci et al., 2001; Reuland et al., 2003; Villar-Martín et al., 2003; Miley et al., 2006; Shukla et al., 2021; Wang et al., 2023b), radio-loud and radio-quiet quasars (e.g., Christensen et al., 2006; Borisova et al., 2016; Farina et al., 2019; Arrigoni Battaia et al., 2018; Arrigoni Battaia et al., 2019; Mackenzie et al., 2021; Fossati et al., 2021). The discovery of Lyα nebulae around quasars is fairly recent. The Multi Unit Spectroscopic Explorer (MUSE) has revealed that Lyα nebulae surrounding radio-quiet and radio-loud quasars are very common (e.g., Borisova et al., 2016; Arrigoni Battaia et al., 2019), suggesting that the previous low detection rate could have been due to limitations of the observing techniques.

There are also structures known as "Lyα blobs" which are luminous Lyα nebulae ($L_{Ly\alpha}$ $\sim 10^{43-44}$ erg s^{-1}) with sizes between $\sim$ 50 - 100 kpc that share some properties with the Lyα halos that surround HzRGs and quasars, many without clear signs of the presence of AGN (e.g Steidel et al., 2000; Matsuda et al., 2004; Smith and Jarvis, 2007; Yang et al., 2014).

Nebulae detected around type 2 AGN (QSO2s and HzRGs) and those surrounding type 1 AGN (radio-quiet and radio-loud quasars) show some differences. Those surrounding HzRGs reach sizes of > 100 kpc (e.g., Reuland et al., 2003; Swinbank et al., 2015), showing a tendency to be smaller than nebulae surrounding radio-quiet quasars (∼ 200 - 500 kpc; e.g., Cantalupo et al., 2014).

Morphological and kinematic studies of Lyα nebulae in radio-quiet and radio-loud quasars show that these properties seem to be independent of the radio loudness, but the smallest nebulae tend to be more symmetric (e.g., Borisova et al., 2016) than the largest ones (e.g., Cantalupo et al., 2014; Hennawi et al., 2015; Arrigoni Battaia et al., 2018). The majority of the nebulae in these objects show relatively quiescent kinematics ($\mathrm{FWHM}_{\mathrm{Ly}\alpha} \lesssim 900$ km s^{-1}; Borisova et al., 2016; Arrigoni Battaia et al., 2018; Arrigoni Battaia et al., 2019), consistent with gravitational motions. There are a few cases where authors found extreme kinematics ($\mathrm{FWHM}_{\mathrm{Ly}\alpha} > 1000$ km s^{-1}) on tens of kpc scales (< 30 kpc) around quasars (e.g., Brusa et al., 2015; Cicone et al., 2015; Perna et al., 2015) but this does not appear to be the norm (e.g., Perna et al., 2015; Arrigoni Battaia et al., 2019).

The Lyα nebulae surrounding HzRGs are usually asymmetric, extending more in the direction of the radio axis (e.g., van Ojik et al., 1996; Villar-Martín et al., 2007b; Wang et al., 2023b). They show a mix of gas with low and high velocity widths. While perturbed kinematics ($\mathrm{FWHM}_{\mathrm{Ly}\alpha} > 1000$ km s^{-1}) are found within the extent of the radio source and frequently associated with the radio-jets, smaller velocity widths ($\mathrm{FWHM}_{\mathrm{Ly}\alpha} < 700$ km s^{-1}) are observed on larger scales (∼ 100 kpc), beyond the radio structures in the extended low surface brightness halo where the kinematics are consistent with gravitational motions (e.g., van Ojik et al., 1997; Villar-Martín et al., 2003) similar to the quiescent gas that is seen around quasars. In addition to Lyα, extended emission from C IV $\lambda\lambda$1548,1550, He II λ1640, and C III] $\lambda\lambda$1907,1909 is usually also observed in the spectra of HzRGs (e.g., Villar-Martín et al., 1999; Vernet et al., 2001; De Breuck et al., 2000; Villar-Martín et al., 2003).

The nature of these nebulae has been debated for several decades already, and the community is yet to reach a solid consensus. Several mechanisms have been proposed to explain the extended Lyα emission, amongst them

- **Recombination following hydrogen photoionization or fluorescence**: this is believed to be the main emission mechanism in photoionized nebulae (e.g., Mackenzie et al., 2021; Humphrey et al., 2008a; Geach et al., 2009; Overzier et al., 2013; Cantalupo et al., 2014; Cantalupo, 2017). In this scenario, AGN or young massive stars produce ionizing radiation that photoionizes the surrounding hydrogen gas. The ionized hydrogen atoms recombine with free electrons present in the gas that rapidly fall down to the ground state in radiative cascades emitting photons in the process. Under case B recombination[4], after the capture of a free electron in an ionized gas with a temperature of around 10^4 K, 68% of recombinations result in the production of a Lyα photon (e.g., Osterbrock, 1989; Dijkstra, 2014), making Lyα the brightest hydrogen emission line.

- **Resonant scattering or "continuum pumping"**: in this scenario, Lyα-wavelength photons are produced in the central regions of the host galaxy either by recombination or collisions and are subsequently scattered in the ISM and CGM (e.g., Villar-Martín et al., 1996; Hayes et al., 2011; Humphrey et al., 2013a; Cantalupo et al., 2014; Beck et al., 2016; Kim et al., 2020; Costa et al., 2022). The amount of scatterings depends on the properties of the medium, such as the neutral hydrogen column density, geometry, and kinematics.

- **Collisional excitation or cooling radiation**: in this case, the Lyα emission is powered by the gravitational energy of the cold streams of gas falling into the dark matter potential of the host galaxy (e.g., Haiman et al., 2000; Dijkstra et al., 2006; Dijkstra and Loeb, 2009; Rosdahl and Blaizot, 2012; Humphrey et al., 2013a; Fumagalli et al., 2014; Trebitsch et al., 2016; Ao et al., 2020). Collisional excitation

[4]Case B recombination assumes a medium that is locally optically thick to hydrogen-ionizing photons, which is expected in the astrophysical media in which we are interested in this work.

occurs when a free electron collides with a hydrogen atom without recombining, transferring some of its kinetic energy to the atom. This energy is subsequently lost via radiative de-excitation. This process is also known as "cooling radiation" (Haiman et al., 2000; Furlanetto et al., 2005), because the kinetic energy of the free electrons is converted into radiation, resulting in the cooling of the gas. This mechanism depends strongly on the density of the gas, since it depends on the interaction between free electrons and neutral hydrogen (H I), so higher gas densities lead to a higher number of collisions.

- **Radiation induced by shocks**: this excitation mechanism can be powered by the radio-jets or outflowing gas (superwinds; e.g., Taniguchi and Shioya, 2000; Mori et al., 2004; Allen et al., 2008).

Several mechanisms may be working at once (e.g., Arrigoni Battaia et al., 2019; Mitchell et al., 2021; Li et al., 2022), but determining the contribution from different powering mechanisms is challenging.

The study of the extended Lyα emission is especially difficult because Lyα is a resonant line, thus highly affected by resonant scattering. Lyα photons may be reabsorbed and re-emitted several times before escaping their production site, and in each scattering the frequency of the Lyα photons can be shifted, and the direction of propagation can also be altered (Osterbrock, 1962). This complicates the study of Lyα nebulae, especially in cases where no other lines are detected because the emerging Lyα spectrum depends not only on the mechanism driving the emission of the line but also on the properties of the medium through which the Lyα flux travels (amount of dust, velocity, geometry and density of H I; e.g., Neufeld, 1990; Verhamme et al., 2006; Dijkstra, 2014). In addition, a large number of scatterings also increases the chances of Lyα being absorbed by dust present in the system. On the other hand, as Lyα photons escape from galaxies, the kinematic structure of the H I gas becomes imprinted on the line, changing the shape of the line profile (e.g., Verhamme et al., 2006; Verhamme et al., 2008) making it a potentially useful tracer of the properties of the ambient gas.

Even with all its associated challenges, the study of Lyα nebulae is of extreme importance. Gas in these regions traces the ISM and CGM where a large number of astrophysically important processes are believed to be taking place, among them infall of gas to the central regions of the galaxy, outflows due to feedback effects, or merger events. Thus, all the processes that lead to the formation of massive galaxies can potentially leave an imprint in these nebulae, imprints that we aim to decipher.

1.6 Outline of this thesis

This thesis is a study of emission-line nebulae associated with AGN at high redshift and is split in two parts. Part I focuses on the ionization modelling of gas in the NLR of AGN, more precisely on the possible presence of non-thermal electron energy distributions in AGN photoionized nebulae, and their impact on the estimation of the nebulae physical parameters (such as metallicity and density).

Part II focuses on a particular radio galaxy, 4C +03.24 at z ~ 3.57, and the Lyα halo that surrounds it. A detailed study of the Lyα nebula is presented, studying the kinematics and morphology of this region and examining the signs of interaction between the radio-jets and the host galaxy. The goal is to understand the nature of the Lyα nebula associated with this object and assess the impact of AGN feedback in this galaxy.

- In **Chapter 2** we give a brief introduction to the Maxwell-Boltzmann (M-B) and the κ electron energy distributions. The photoionization models and parameters used in this work are presented, as well as a comparison of the results obtained using M-B and κ electron energy distributions. In this chapter we show how the electron energy distribution affects the gas parameters (e.g., ionization parameter, metallicity) obtained with the photoionization models.

- **Chapter 3** presents a comparison between models and line ratios gathered from the literature for a sample of relevant AGN. We use the aforementioned ionization models with the objective of finding the best fitting model for each galaxy in the sample, to assess whether models using a κ or M-B distribution are better able to reproduce the observed emission line ratios.

- In **Chapter 4** we present the analysis of the spectacular Lyα nebula that surrounds the radio-galaxy 4C+03.24. Kinematic and morphological analyses are presented and we present a scenario to explain the properties of the extended Lyα nebula.
- Finally, in **Chapter 5** we present a summary of the main results of this thesis and an outlook into future works that are needed to address a number of highly relevant open questions.

In this work we assume a flat ΔCDM cosmology with Ω_Δ = 0.73, Ω_m = 0.27 and H_0 = 71 km s^{-1} Mpc^{-1} to derive physical properties. Using this cosmology, at z = 3.57 one arcsec corresponds to 7.399 kpc.

Chapter 2

Electron energy distributions in the ionized gas of active galaxies: Maxwell-Boltzmann versus κ distributions

One of the main goals of this work is to gain a better understanding of the evolution of galaxies, in particular on the impact of feedback effects on the evolution of type 2 AGN hosts. To do this it is important to investigate the ISM properties of active galaxies, such as metallicity, electron density and ionization parameter, that can provide information about their evolution histories. These properties can be inferred from the emission lines observed in the spectra of the galaxies.

The NLR of active galaxies is particularly important and is usually targeted in spectroscopic studies (e.g., Villar-Martín et al., 1999; Nagao et al., 2006; Humphrey et al., 2008a; Matsuoka et al., 2009; Feltre et al., 2016; Morais et al., 2017; Silva et al., 2018; Matsuoka et al., 2018) because the gas clouds are distributed up to the kiloparcsec scale, allowing us to trace the ISM on a similarly large scale. In addition, the NLR shows emission lines from a multitude of chemical elements in a wide range of ionization stages which makes them ideal places to study the properties of the ISM. Low-ionization lines such as [Si II] λ1261, Mg II λ2800, C II] λ2326, are observed, but also high ionization lines such as C IV $\lambda\lambda$1548,1550, He II λ1640, C III] $\lambda\lambda$1907,1909 and [Ne V] λ3426 (see example in Figure 2.1). It has been shown that the wide range of ionization states observed in the NLR and ENLR of AGN cannot be produced by stars, requiring a source with a harder spectrum. The general consensus is that the gas in these regions is ionized predominantly by the radiation field of an AGN (e.g., Ferland and Netzer, 1983; Osterbrock and Ferland, 2006; Thomas et al., 2016).

When sufficient optical emission lines are observed in the spectra of an object, they can be used to determine several parameters directly, using ratios involving faint lines (electron temperature and density, chemical composition; e.g. Peimbert, 1967; Izotov et al., 2006; Curti et al., 2017; Kakkad et al., 2018; Maiolino and Mannucci, 2019). However this is usually not the case in observations at high redshift. In the NLR of AGN usually only a few emission lines are observed and mostly in the rest-frame UV band, at least until recent observations with the James Webb Space Telescope (see Section 5; e.g. Taylor et al., 2022; Sanders et al., 2023a). Thus, it is more usual that the properties of the NLR are derived through comparisons between photoionization models and the observed spectra (e.g., Ferland and Netzer, 1983; Binette et al., 1996; Feltre et al., 2016; Silva et al., 2018; Matsuoka et al., 2018).

Photoionization codes compute recombination rates, ionization rates, and fluxes of spectral lines, which depend on a number of parameters (e.g., chemical composition of the gas, hydrogen density). Among those parameters we have the shape of the electron velocity (or energy) distribution, which is usually assumed to be a Maxwell-Boltzmann (M-B) distribution (e.g., Villar-Martín et al., 1997; Moy and Rocca-Volmerange, 2002; Humphrey et al., 2008a; Matsuoka et al., 2009; Morais et al., 2017; Silva et al., 2018). However, recently it has been shown that using κ distributions of electron energies may be more appropriate to reproduce the conditions observed in ionized gas (e.g., Nicholls et al., 2012; Nicholls et al., 2013).

A key issue is that the results of photoionization models are strongly affected by the electron energy distribution (EED) selected. By using a distribution that does not apply to the gas one is modeling, the inferred quantities or properties may be inaccurate, leading to potentially incorrect conclusions about, for example, the chemical evolution history of an AGN host galaxy. In the next section, the Maxwell-Boltzmann and the κ electron energy distributions, and their main differences are described.

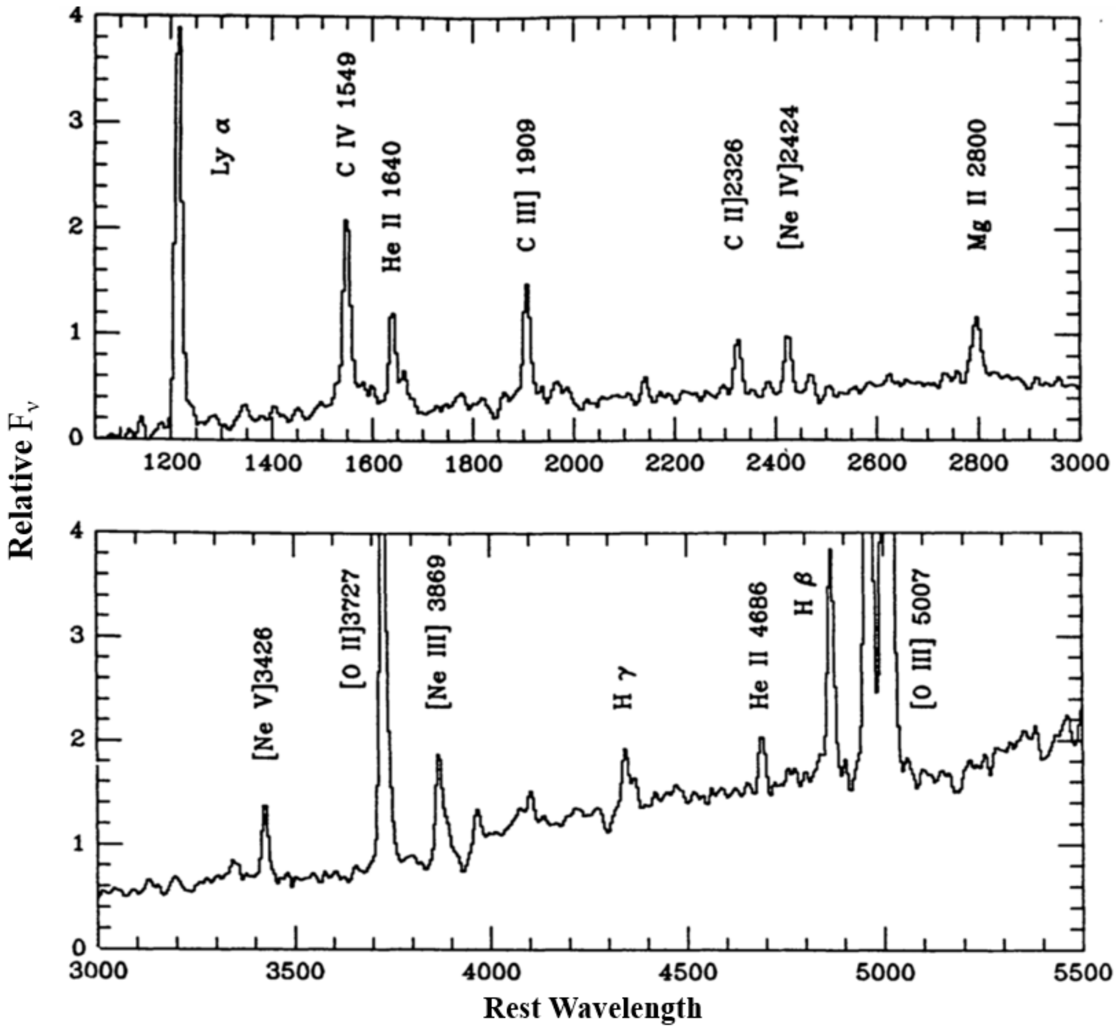

Figure 2.1: Composite radio galaxy spectrum at rest-frame UV (top figure) and optical (bottom figure) wavelengths, constructed from observations of galaxies with $0.1 < z < 3$. Adapted from Figure 1 in McCarthy (1993).

2.1 Electron energy distributions

2.1.1 Maxwell-Boltzmann distribution

The Maxwell-Boltzmann (M-B) electron velocity distribution is a mathematical equation that describes how many particles are found at each velocity when a particle system is in thermal equilibrium. This distribution was first defined to describe the properties of an ideal gas, where particles move freely, with no interaction with each other and no energy exchange processes, except for brief collisions in which there is momentum and energy exchange between particles and with the environment. In these types of systems, particles are distributed in a specific way; there are many particles with small velocities and a small number of particles with large velocities.

Following Hebb and Menzel (1940), the fraction $f(v)$ of electrons having velocities between v and $v + dv$ is given by

$$f(v)\,dv = 4\pi\, n_e \left(\frac{m_e}{2\pi k_B T_e}\right)^{3/2} v^2\, exp\left(-\frac{m_e v^2}{2k_B T_e}\right) dv\,, \tag{2.1}$$

where $n_\mathrm{e} = \int_0^\infty f(v)dv$, or the electron number density, T_e is the electron temperature, k_B is the Boltzmann constant, m_e the electron mass and v is the thermal velocity, or most probable velocity, given by

$$v = \sqrt{\frac{2k_B T_e}{m_e}}\,. \tag{2.2}$$

In energy terms the M-B equation is written as

$$f(E)\,dE = 2n_e\sqrt{\frac{E}{\pi}}\left(\frac{1}{k_B T_e}\right)^{3/2} exp\left(-\frac{E}{k_B T_e}\right) dE\,, \tag{2.3}$$

where $f(E)$ is the fraction of electrons having an energy E, and T_e and k_B are the same as in equation 2.1.

The velocity distribution of the free electrons in gaseous nebulae has been assumed to follow a M-B distribution since at least the 1930s, when treatments of the physical state of Planetary Nebulae (PNe) already assumed this distribution (e.g., Bohm and

Aller, 1947; Hebb and Menzel, 1940). This assumption is based on the electron thermalization timescale, the timescale a free electron requires to become thermalized and described by the M-B distribution (e.g., Bohm and Aller, 1947; Spitzer, 1962). It is usually assumed that free electrons share their energy with the neighbouring medium so rapidly that they become thermalized before they are able to produce any line emission (e.g., Ferland et al., 2016). The thermalization timescale of energetic electrons is proportional to the cube of their velocity (Spitzer, 1962), so plasmas with high energy electrons will take longer to reach equilibrium than plasmas with lower energy electrons. Since the thermalization timescale depends on the frequency of collisions, electron energies in high density gas will equilibrate faster than in low density gas.

Photoionization models using M-B distributions have been widely used to study the conditions of the gas in H II regions, PNe and AGN (e.g., Villar-Martín et al., 1997; Villar-Martín et al., 1999; Kewley and Dopita, 2002; Humphrey et al., 2008a; Zhang, 2008; Dors et al., 2018; Guo et al., 2020). However, there are two longstanding problems in the study of photoionized nebulae: the systematic discrepancies in abundances and temperatures derived from different ionic species (e.g., Wyse, 1942; Kaler, 1986; Wilson et al., 1997; Liu et al., 2001; García-Rojas and Esteban, 2007; Dors et al., 2015; Peimbert et al., 2017; Dors et al., 2020; Rickards Vaught et al., 2023); and the discrepancy in the temperatures estimated from models and the temperatures measured using oxygen lines, where temperatures observed are found to be systematically higher than the ones predicted by photoionization models (e.g., Tadhunter et al., 1989; Villar-Martín et al., 2008; Holt et al., 2009; Binette et al., 2022). Despite several efforts to solve these discrepancies (e.g., Peimbert, 1967; Zhang, 2008; Ali and Dopita, 2019; García-Rojas et al., 2019), they remained unresolved for several decades. However, recently Nicholls et al. (2012) and Nicholls et al. (2013) suggested that using kappa (κ) electron energy distributions (EEDs) instead of the M-B distribution in photoionization models could solve these longstanding problems.

2.1.2 The κ distribution

The suggestion that the electron velocity (or energy) distribution may be non-Maxwellian dates back to the 1930s, when Hagihara (1939a) and Hagihara (1939b) argued that the velocity distributions in PNe may show significant departures from a M-B distribution. This was refuted by Bohm and Aller (1947) who claimed that any deviation of electron velocities from a M-B distribution would be very small and could be neglected.

Later, empirical κ distributions were used to describe magnetospheric electron observations (e.g., Binsack, 1966; Olbert, 1968; Vasyliunas, 1968) and afterwards they were measured in several solar system plasmas. κ distributions are present in the solar wind (e.g., Gloeckler et al., 1992; Maksimovic et al., 1997; Pierrard and Pieters, 2014; Moncuquet et al., 2020), in the solar corona and solar flares (e.g., Dudík et al., 2017; Oka et al., 2018), in the outer heliosphere and the inner heliosleath (e.g., Decker and Krimigis, 2003; Heerikhuisen et al., 2008; Scherer et al., 2022), in planetary magnetospheres (e.g., Dialynas et al., 2009; Espinoza et al., 2018; Kirpichev et al., 2021), including the magnetosheath (e.g., Binsack, 1966; Olbert, 1968; Ogasawara et al., 2013; Ergun et al., 2020), and magnetospheres of planetary moons (e.g., Jurac et al., 2002; Moncuquet et al., 2002). Despite the evidence that κ distributions are prevalent in solar system plasmas, the possibility of the existence of κ distributions in extra-solar gaseous nebulae has only recently been explored: Nicholls et al. (2012) used the κ distribution in order to resolve longstanding discrepancies in the measurements of abundances and temperatures in H II regions and PNe.

κ distributions describe stationary state systems out of thermal equilibrium. The κ distribution has a Maxwellian-like core and a high-energy power-law tail. In these systems there are more particles with high energies than in a system in thermal equilibrium. Following Vasyliunas (1968) and Nicholls et al. (2012), the κ energy distribution can be written as:

$$f_\kappa(E)dE = \frac{2n_e}{\sqrt{\pi}} \frac{\Gamma(\kappa+1)}{(\kappa-3/2)^{\frac{3}{2}}\,\Gamma(\kappa-1/2)} \times \frac{\sqrt{E}}{(k_BT_\kappa)^{3/2}\left(1+E/\left[(\kappa-3/2)k_BT_\kappa\right]\right)^{\kappa+1}}\,dE\,, \tag{2.4}$$

where n_e is the electron density, Γ is the gamma function, k_B is the Boltzmann constant, T_κ is the non-equilibrium temperature that characterizes the mean kinetic energy ($T_\kappa = < E > /(1.5k_B)$) and κ is a parameter that characterizes the distribution and varies from $3/2 < \kappa \leq \infty$. The κ index measures the departure from an equilibrium distribution; as κ increases the fraction of high energy electrons decreases (see Figure 2.2). At the limit $\kappa \rightarrow \infty$, the κ energy distribution reduces to the M-B distribution (equation 2.3).

Compared to the M-B distribution that reaches its peak at $E = (1/2)k_BT_U$, κ distributions reach their peaks at lower energies ($E = (1/2)k_BT_U(2\kappa - 3)/(2\kappa + 1)$), have fewer electrons at intermediate energies and have an excess of electrons at high energies (high energy power-law tail; see Figure 2.2). Thus, generally the κ distribution behaves has a M-B distribution would if it had a lower peak temperature but with a high energy excess. For a given temperature, the fraction of high-energy electrons increases with decreasing κ.

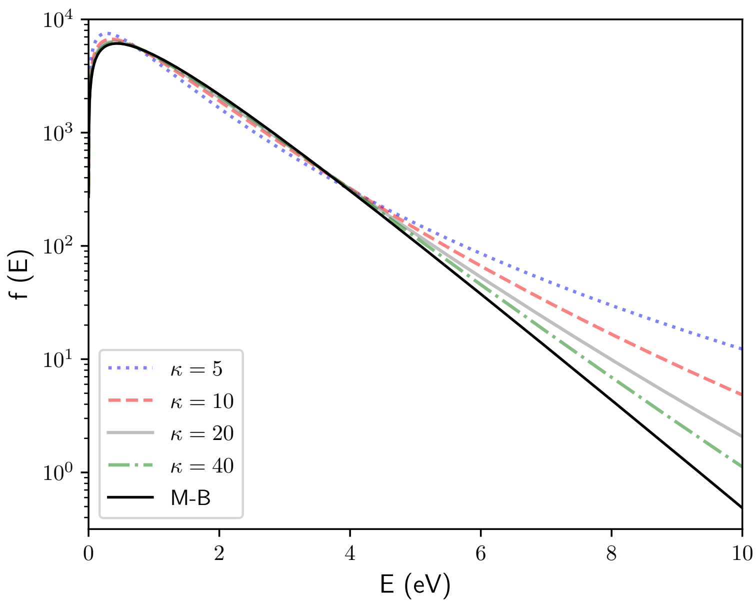

Figure 2.2: κ electron energy distributions for κ=5, κ=10, κ=20, κ=40 compared to a M-B distribution, all at the same temperature. The y-axis shows the fraction of electrons (f(E)) having energies between 0 and 10 eV (x-axis).

An interesting result from Nicholls et al. (2013) is the effect that a $\kappa = 10$ distribution has on the collisional excitation rate when compared to the M-B distribution, as shown in Figure 2.3. According to Nicholls et al. (2013), Figure 2.3 gives a general description of the effects of a κ distribution on the intensities of collisionally excited lines (CELs). For a κ distribution there is a slight enhancement of the IR emission line intensities (dark grey area), a reduction in the optical transitions (light grey area), and a strong enhancement in the UV population.

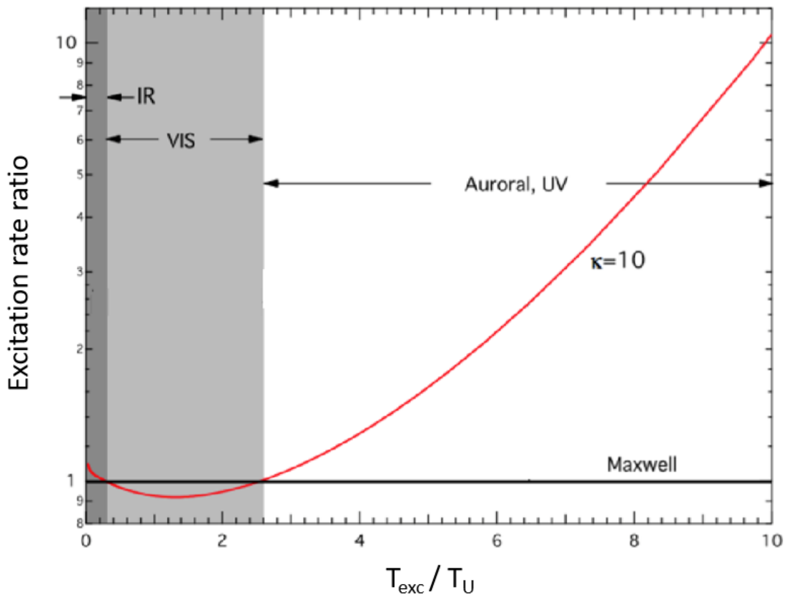

Figure 2.3: Comparison between the collisional excitation rate for a $\kappa = 10$ and the M-B distributions as a function of the excitation threshold energy divided by the kinetic temperature (T_U). Figure 7 in Nicholls et al. (2013).

There were two main potential objections to the use of κ-EEDs in the study of astrophysical systems outside the solar system: the lack of theoretical justification, which is now partly being resolved, since it has been shown that they are consistent with thermodynamics (e.g., Tsallis et al., 1995; Tsallis, 1988; Leubner, 2002; Livadiotis and McComas, 2009; Livadiotis, 2018; Livadiotis and McComas, 2022); and the lack of physical mechanisms capable of generating and maintaining κ-EEDs. To overcome the second objection, several mechanisms have been proposed: accelerations induced by shocks; photoionization (when the source of the ionizing photons has a hard photon spectrum); photoionization of dust, suprathermal atom or ion heating, X-ray ionization, or magnetic reconnection (e.g., Dopita and Sutherland, 2000; Raymond et al., 2010; Nicholls et al., 2012; Bradshaw and Raymond, 2013; Crumley et al., 2019; Arnold et al., 2021). For κ-EEDs to be consequential the rate at which energetic electrons enter the gas has to be of the same order or smaller than the thermalization timescale. In this case the high energy tail of the EED may persist and these electrons may be able to affect the observed spectrum. Otherwise the signature of the κ distribution will disappear.

Nicholls et al. (2012) and Nicholls et al. (2013) compared photoionization models using κ electron energy distributions with those that use the M-B distribution and suggested that using κ distributions could solve the abundance and temperature discrepancies found in H II regions and PNe. Following the work of Nicholls et al. (2012), a number of subsequent studies have addressed the possibility of κ electron energy distributions being present in gaseous nebulae, in place of a M-B distribution (e.g., Binette et al., 2012; Dopita et al., 2013; Dopita et al., 2014; Nicholls et al., 2013; Storey and Sochi, 2013; Storey and Sochi, 2014; Mendoza and Bautista, 2014; Humphrey and Binette, 2014; Ferland et al., 2016; Zhang et al., 2016; Davelaar et al., 2019; Humphrey et al., 2019; Lin and Zhang, 2020; Yao and Zhang, 2022b; Yao and Zhang, 2022a) with varied conclusions. While Nicholls et al. (2012), Binette et al. (2012), Nicholls et al. (2013), Humphrey and Binette (2014), and Lin and Zhang (2020) found that using κ distributions solved some of the problems encountered when attempting to reproduce the emission lines observed in H II regions, PNe and AGN, Storey and Sochi (2013), Mendoza and Bautista (2014), Zhang et al. (2016), Ferland et al. (2016), and Draine and Kreisch (2018) found little or no evidence for the existence of κ distributions in these objects.

Since there are a number of mechanisms that may be capable of generating κ distributions in ionized nebulae, and they are somewhat successful at solving discrepancies observed in H II regions and PNe, it is relevant and timely to explore the possibility of κ-distributed electron energies existing in gaseous nebulae ionized by AGN. Ionized nebulae in active galaxies are probably more predisposed than H II regions and PNe to have κ-distributed electron energies, due to the harder radiation field of the AGN and to the magnetic fields associated with radio jets. Regions ionized by AGN have also lines with a wide range in excitation energy, making them an excellent test for the presence of κ-distributed electron energies.

In this section, we have given a very general, and simplified description of the history of κ electron energies distributions and the mechanisms that can generate them in astrophysical plasmas, but the actual physical formulation of the problem is out of the scope of this thesis. Our goal is to understand how κ-EED affect the results obtained from photoionization models and the recovery of the physical parameters of the ionized nebulae we are studying, to understand whether they should be taken into account when analyzing these types of sources. This study and results are presented in the next sections.

2.2 MAPPINGS 1e models

Photoionization codes calculate the physical conditions of a gas irradiated by an external source of ionization and predict the resulting spectrum. The first photoionization codes were developed in the 60's to study low-density nebulae (Harrington, 1968). Since then, several developments have been made, to include, for example improvements in the atomic processes. Codes can differ in their radiative treatment, geometry, equilibrium conditions, shocks, atomic data or number of emission lines. Some examples of photoionization codes are CLOUDY (Ferland et al., 1998), MAPPINGS III (Sutherland et al., 2013), MAPPINGS 1 (Binette et al., 1985; Ferruit et al., 1997; Binette et al., 2012).

In this work we use the photoionization code MAPPINGS 1e (Binette et al., 1985; Ferruit et al., 1997; Binette et al., 2012) that includes the option of selecting κ distributions of electron energies instead of the equilibrium M-B distribution (see Binette et al., 2012).

2.2.1 Model Parameters

Our photoionization models consider an isochoric, plane-parallel slab of gas of density n_H. The slab of gas is illuminated by a power-law spectrum of ionizing radiation ($S_\nu \propto \nu^\alpha$). The intensity of the radiation relative to the gas density is given by the ionization parameter, U. We adopted ionization-bounded termination and ended the calculation when the ionization fraction of hydrogen drops below 0.01. Our models did not consider depletion of metals into dust.

Our goal is to investigate how line ratio predictions change depending on the adopted electron energy distribution function. To do this, we compute a large grid of photoionization models using M-B or κ electron energy distributions for identical parameters. In addition to models using the M-B distribution, we compute models where the index κ has the values 5, 10, 20, and 40. Nicholls et al. (2012) suggested that for PNe and H II regions a value of κ in the range $10 \lesssim \kappa \lesssim 20$ would be enough to solve the discrepancies. However, we choose a wider range to explore all possibilities and get a more general view of the effect of κ-EEDs. Apart from the EED parameter, the main model parameters that were varied are as follows:

- **Ionization parameter,** U

  The ionization parameter is given by

  $$U = \frac{Q}{4\pi r^2 n_H c}, \tag{2.5}$$

  where Q is the ionizing photon luminosity, r is the distance between the ionized cloud and the ionizing source, c is the speed of light and n_H is the hydrogen gas density. This parameter indicates the intensity of the ionizing radiation as felt by the cloud. The ionization parameter measures the ratio between ionizing photons and particles in the model gas cloud and can be used as a proxy for the ionizing state of the gas.

  The NLR and ENLR can extend for tens of kpc, and U may vary between different regions within a source and also between different sources. Thus, we consider a large range in U and compute sequences of models in which U varies from 10^{-5} to 1.8.

- **Power-law index,** α

  For the power-law index of the ionizing continuum we adopt the values α = -2, -1.5, -1 which are consistent with values adopted in the literature (e.g., Robinson et al., 1987; Villar-Martín et al., 1997; Zheng et al., 1997; Radovich et al., 1998; Groves et al., 2004). The models computed assuming α = -1.5 and α = -2 have a high energy cut-off for the ionizing continuum of 5×10^4 eV, to ensure that the mean ionizing photon energy matches the value derived for radio-loud AGN (e.g., Mathews and Ferland, 1987). Models with an ionizing continuum with α = -1 assume a cut-off energy of 1000 eV to ensure that the mean photon energy matches that of the α = -1.5 power-law.

- **Hydrogen density,** $\mathbf{n_H}$

  For the hydrogen density we adopted n_H = 100, 10^4, 10^6 cm^{-3} following the results from McCarthy et al. (1990), Villar-Martín et al. (1999), Fu and Stockton (2008), Zhang et al. (2013), Kakkad et al. (2018), and Binette et al. (2022). Our models assume constant density in the photoionization region.

  Hydrogen density of 100 cm^{-3} is more adequate to simulate spatially extended, low density gas, outside of the AGN central region. However, we also wanted to test the impact of higher gas density so we have computed models where n_H = 100, 10^4, 10^6 cm^{-3}. We note that the existence of very high densities ($\sim 10^6$ cm^{-3}) in the NLR is not expected, since the large strength of the [O II] λ3727 line, which has a critical density of $\sim 3\times10^3$ cm^{-3}, suggests that the line fluxes have a very high contribution of much lower density gas.

- **Gas metallicity,** Z

  For the metallicity (defined as Z = O/H) we consider $Z/Z_\odot = 0.1$, $Z/Z_\odot = 0.5$, $Z/Z_\odot = 1.0$, $Z/Z_\odot = 2.0$ and $Z/Z_\odot = 3.0$. The gas metallicity is expressed with respect to the solar abundance set of Grevesse et al. (2010). The chemical abundances have been scaled with all metals scaled proportionally to oxygen except nitrogen and carbon. Nitrogen and carbon are scaled quadratically with oxygen (e.g., Henry et al., 2000; Silva et al., 2020; Huang et al., 2023) when $Z \gtrsim 0.3Z_\odot$. Below this metallicity they are scaled linearly (N/H $\propto$ O/H, e.g., Henry et al., 2000).

Table 2.1: Set of chemical abundances used in MAPPINGS Ie. The abundances were obtained using secondary behaviour of N and C.

$Z / Z_\odot$	0.1	0.5	1	2	3
H	1.0	1.0	1.0	1.0	1.0
He	8.5×10^{-2}	8.5×10^{-2}	8.5×10^{-2}	8.5×10^{-2}	8.5×10^{-2}
C	8.1×10^{-6}	6.75×10^{-5}	2.7×10^{-4}	1.08×10^{-3}	2.43×10^{-3}
N	2.04×10^{-6}	1.7×10^{-5}	6.8×10^{-5}	2.72×10^{-4}	6.12×10^{-4}
O	4.9×10^{-5}	2.45×10^{-4}	4.9×10^{-4}	9.8×10^{-4}	1.47×10^{-3}
Ne	8.5×10^{-6}	4.25×10^{-5}	8.5×10^{-5}	1.7×10^{-4}	2.55×10^{-4}
Fe	3.2×10^{-6}	1.6×10^{-5}	3.2×10^{-5}	6.4×10^{-5}	9.6×10^{-5}
Mg	4.0×10^{-6}	2.0×10^{-5}	4.0×10^{-5}	8.0×10^{-5}	1.2×10^{-4}
Si	3.2×10^{-5}	1.6×10^{-5}	3.2×10^{-5}	6.4×10^{-5}	9.6×10^{-5}
S	1.3×10^{-6}	6.5×10^{-6}	1.3×10^{-5}	2.6×10^{-5}	3.9×10^{-5}
Ca	2.2×10^{-7}	1.1×10^{-6}	2.2×10^{-6}	4.4×10^{-6}	6.6×10^{-6}
Ar	2.5×10^{-7}	1.25×10^{-6}	2.5×10^{-6}	5.0×10^{-6}	7.5×10^{-6}

A summary of all the parameters used in the photoionization models is presented in Table 2.2. In total, the grid has (100 U) x (5 Z) x (3 n_H) x (5 κ) = 7500 models.

Table 2.2: Parameters of the photoionization models.

Parameter	Value
U	10^{-5} - 1.8
α	-2, -1.5, -1
$Z / Z_{\odot}$	0.1, 0.5, 1.0, 2.0, 3.0
n_H (cm^{-3})	100, 10^4, 10^6
EED	M-B, κ = 5, κ = 10, κ = 20, κ = 40

2.3 Results of the models

In this section, we compare the results obtained with photoionization models assuming M-B and κ electron energy distributions when different parameters are adopted. Hereafter, we refer to κ / M-B of a given emission line as the quotient between the line flux obtained when a κ distribution is used with respect to the same line flux assuming a M-B distribution. This parameter provides a measure of how the flux of a given line is impacted by the use of the κ EED compared to the case where the M-B EED is used. A value above one indicates the line flux is relatively enhanced by using a κ EED, while a value lower than one would indicate the line flux is relatively reduced by using a κ EED.

In Figures 2.4 to 2.12 we show results from our grid of photoionization models, for emission lines in the IR, optical, and UV wavelength ranges. The figures are organized as follows: each emission line is shown for different model parameters, κ and M-B electron energy distributions. Each panel in the figures corresponds to different assumptions concerning the gas metallicity.

2.3.1 Infrared emission lines

We show our predictions for the following lines: [Ar III] λ9 μm, [Ne V] λ14 μm, [S IV] λ10.5 μm, [Ne II] λ12.8 μm, [Ne III] λ15.6 μm, [Ne V] λ24 μm, [O IV] λ25.9 μm, [O III]

λ52 μm, [N II] λ122 μm, [O I] λ63 μm, [O III] λ88 μm, [C II] λ158 μm, [S III] λ9532 and [S III] λ9069.

In general, our calculations show that the flux of infrared (IR) emission lines is predicted to be weaker for κ distributions. Our results are in agreement with those in Nicholls et al. (2012), Nicholls et al. (2013), and Dopita et al. (2013) who showed that the effect of κ on IR lines is very weak. To illustrate this, we show the ratio between predictions assuming κ and M-B distributions for a selection of IR emission lines typically observed in the NLR of AGN.

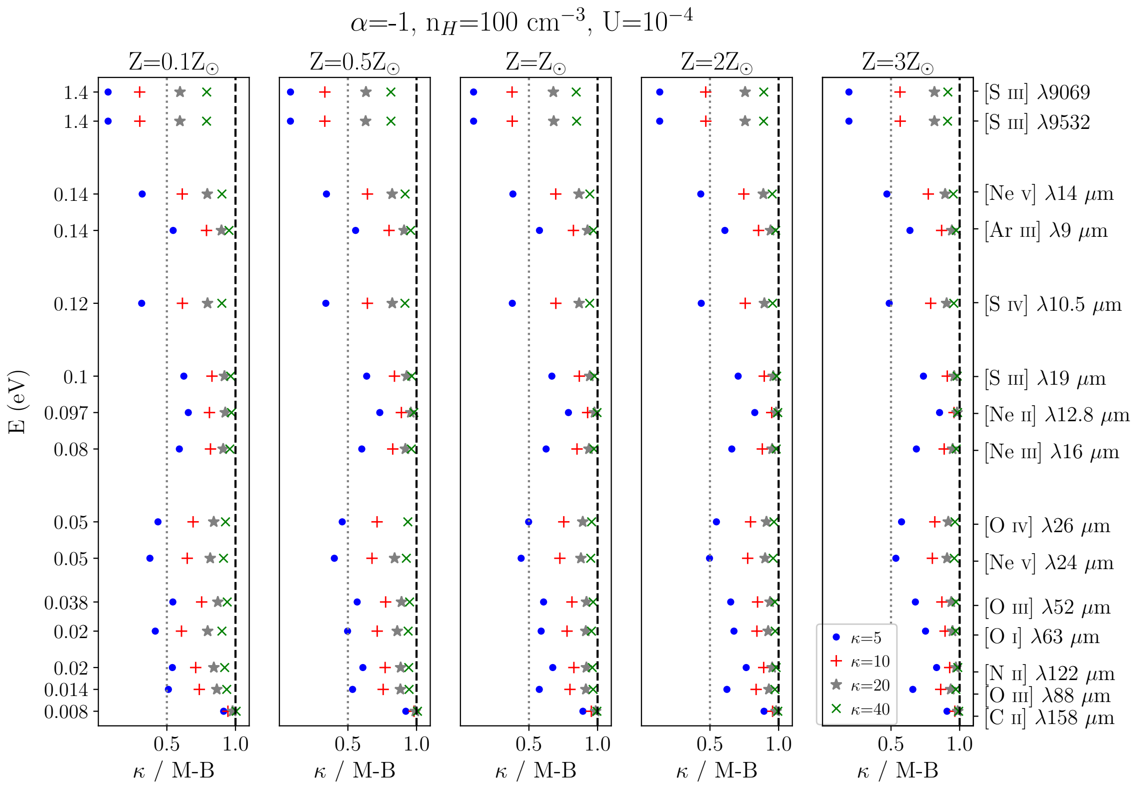

Figure 2.4: Ratios of model fluxes for κ and M-B electron energy distributions, for key IR lines, arranged in order of increasing energy for $U = 1{\times}10^{-4}$. Each panel corresponds to a different value of gas metallicity. Each marker corresponds to a different κ distribution. The grey dotted vertical line shows the position where κ / M-B = 0.5 and the black dashed line marks the position where κ = M-B.

The IR line fluxes calculated for $U = 1\times10^{-4}$ are shown in Figure 2.4. In this figure we show the ratio between predictions assuming κ and M-B distributions for all the lines as a function of the excitation energy of each line. The results cover different values of κ and Z.

Identical results are observed across all emission lines: κ distributions shift the line ratios towards lower values. The shift increases for low values of κ, i.e., for larger deviations from equilibrium. As the metallicity increases, the predictions assuming κ distributions approach the predictions from M-B distributions.

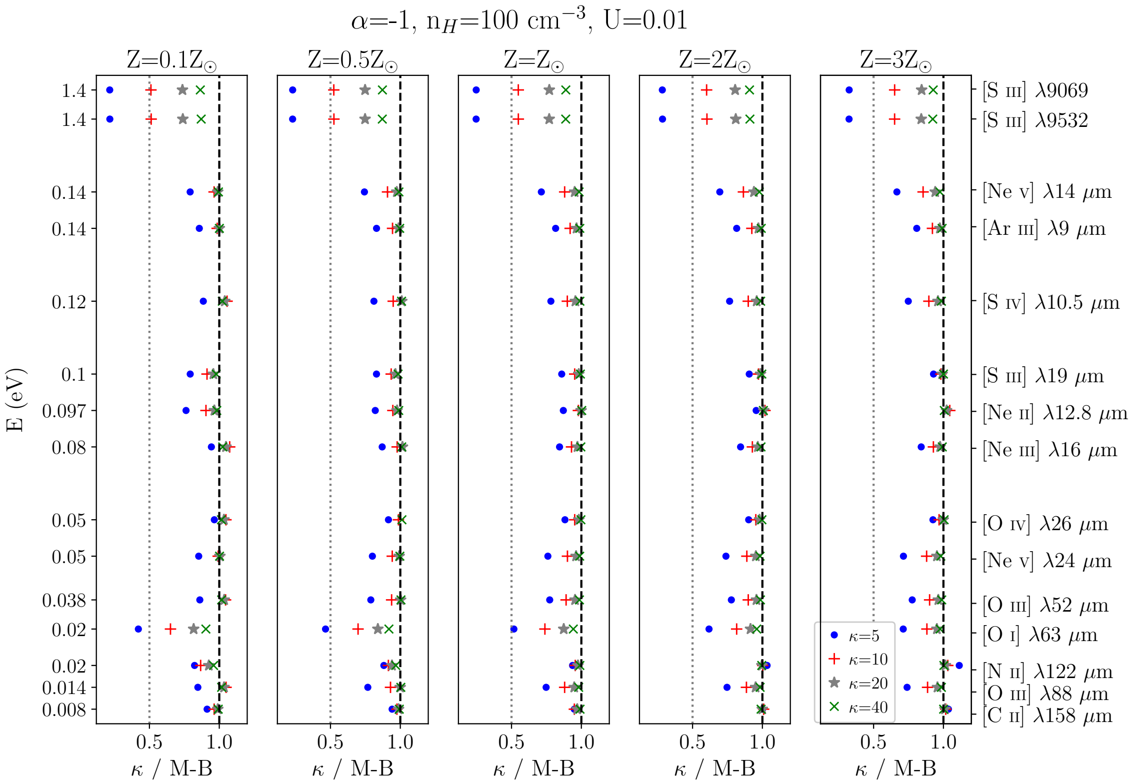

Figure 2.5: Same as Figure 2.4 but with $U = 0.01$.

We obtain similar results for $U = 0.01$, as shown in Figure 2.5. The lines are more intense when a Maxwellian is used. With this ionization parameter, the differences between model predictions become smaller, with the ratio κ / M-B of most lines being shifted closer to unity, when compared to the previous figure.

Finally, the results for U = 1.8 are shown in Figure 2.6, where most of the lines are relatively unaffected by the choice of EED, although there are some slight enhancements when assuming κ distributions with low gas metallicity and κ = 5 (e.g., [N II] λ122 μm, [O I] λ63, [Ne II] λ12.8 μm). [O IV] λ26 μm is also slightly enhanced but only for higher metallicities.

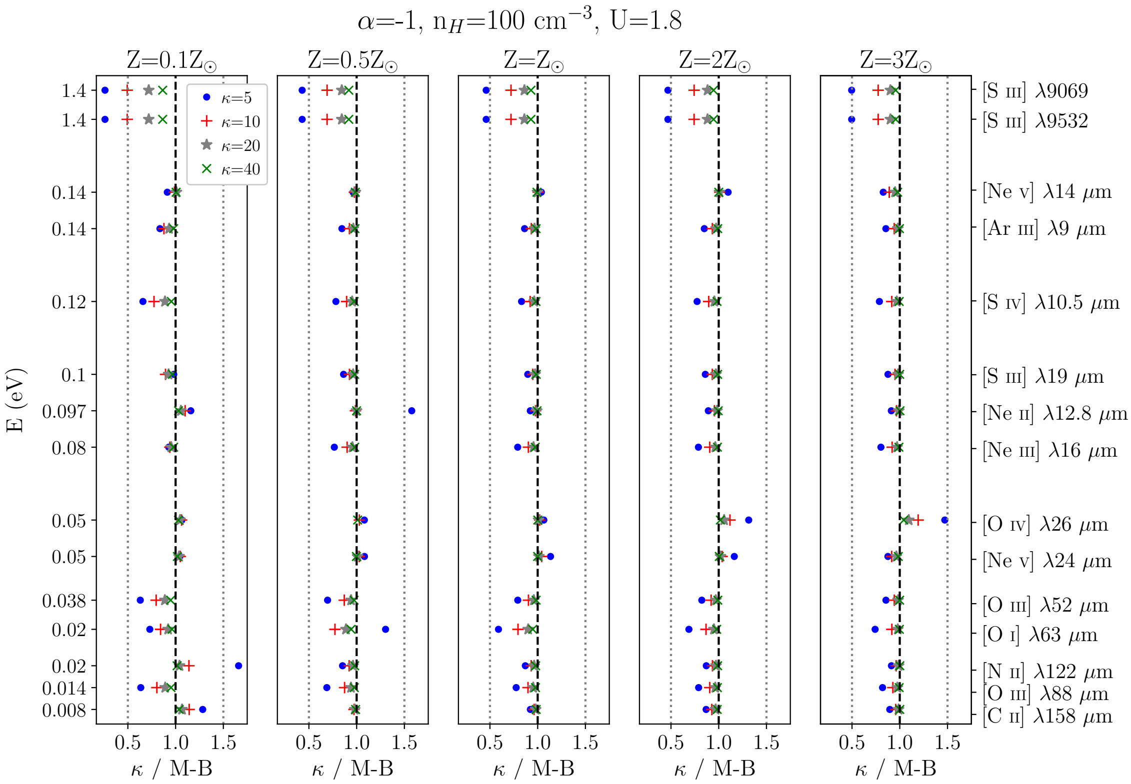

Figure 2.6: Same as Figure 2.4 but with U = 1.8. In this case another grey dotted vertical line was added to mark the position where κ / M-B is 1.5.

In summary, assuming κ distributions of electron energies instead of the M-B distribution moves the IR line fluxes to lower values, except for a small parameter space at low metallicities and with high ionization parameter. Except within a small parameter space with high U (e.g., U = 1.8), the predicted flux ratios are in the range $0.5 \lesssim \kappa$ / M-B < 1 for the majority of IR lines and model parameters.

2.3.2 Optical emission lines

The effect of κ distributions on the emission spectra of *optical* lines is complex. It strongly depends on metallicity and ionization parameter. Figure 2.7 shows the predictions for $U = 1\times10^{-4}$.

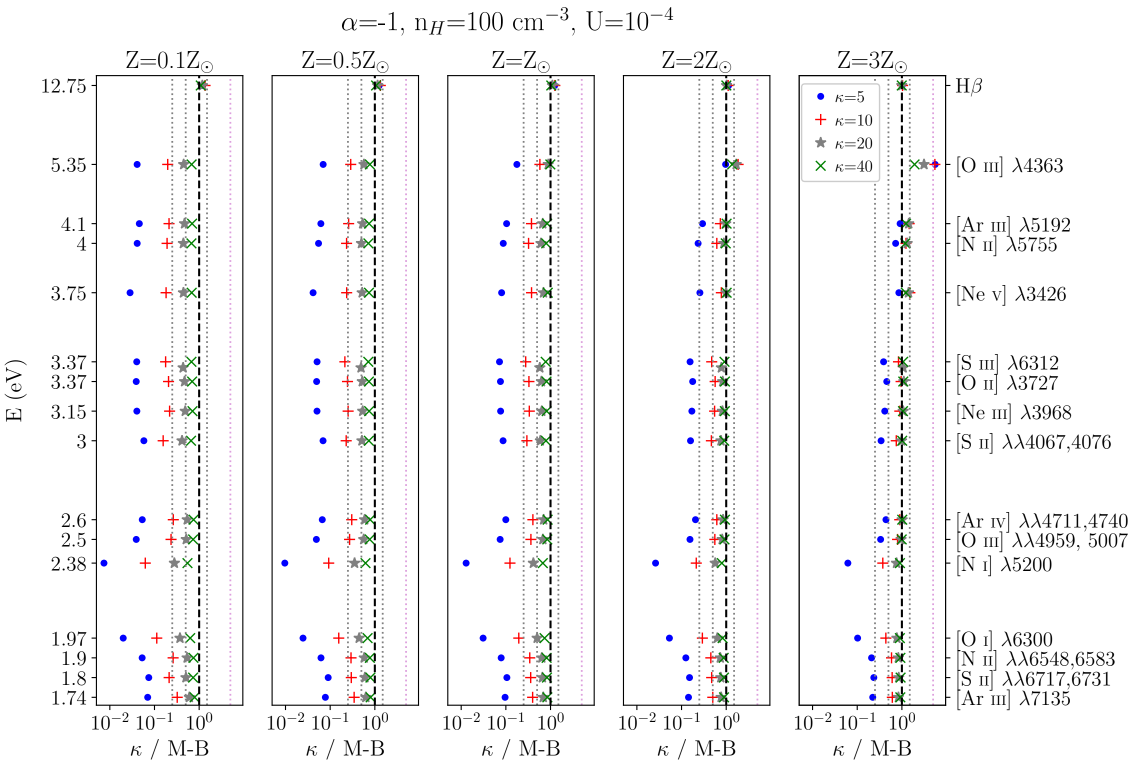

Figure 2.7: Ratios of model flux predictions but with κ and M-B electron energy distributions, for key nebular lines, arranged in order of increasing energy for $U = 1\times10^{-4}$. The grey dotted vertical lines mark the positions where κ / M-B is 0.25, 0.5 and 1.5. The pink dotted line indicates where κ / M-B is 5.

At low metallicities ($Z \lesssim Z_\odot$), the flux predictions from models assuming M-B distributions exceed the flux predictions from the κ models (this is κ / M-B < 1) for all the lines except Hβ, which is very similar for all distributions independently of the metallicity. As the metallicity increases, line fluxes predicted by κ distributions show a slight relative increase (κ / M-B > 1), however the only flux that gets significantly higher when using κ

models is [O III] λ4363. Using this ionization parameter (U = 1×10^{-4}), κ / M-B becomes smaller than 1 for almost all lines considered, with the exception of [O III] λ4363 at high metallicity (3Z$_\odot$).

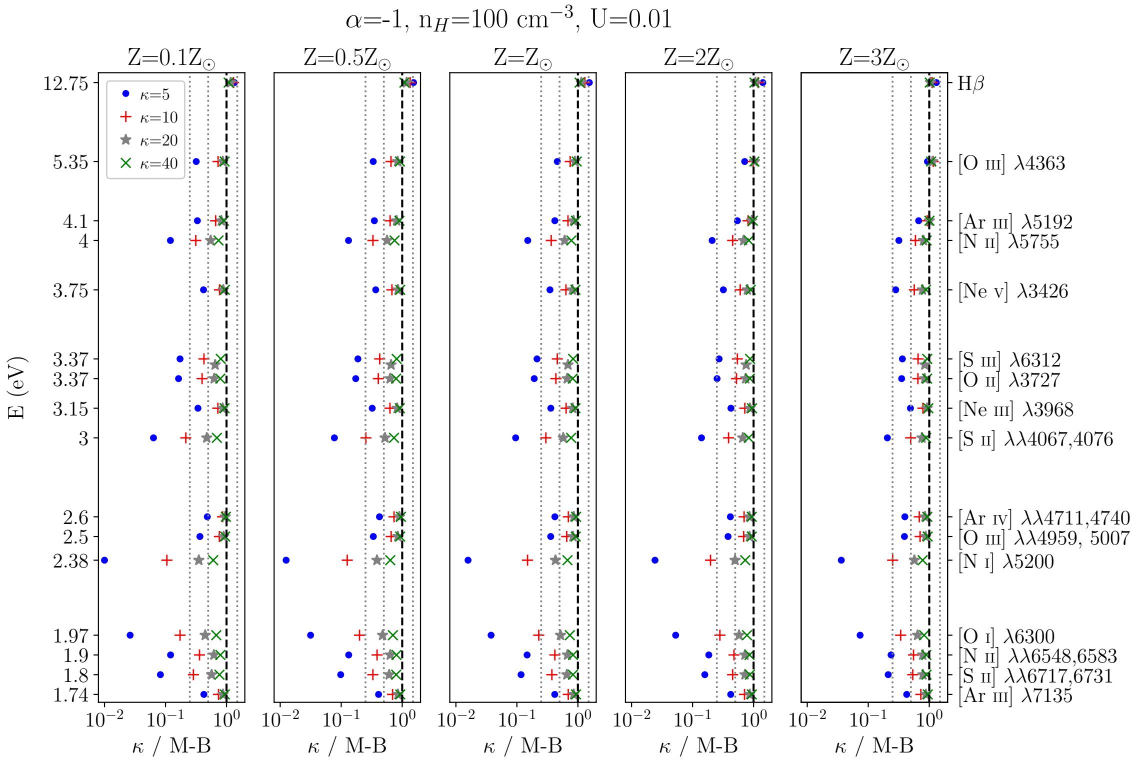

Figure 2.8: Same as Figure 2.7 but with U = 0.01.

In Figure 2.8 the κ / M-B predictions for U = 0.01 are presented. In general, optical line fluxes are not enhanced when assuming κ distributions, with the exception of Hβ. The maximum Hβ_κ / H$\beta_{\text{M-B}}$ is 1.5, reached for κ = 5 and Z = Z$_\odot$. Increasing the metallicity shifts most line fluxes predicted by κ distributions closer to those predicted by a Maxwellian.

The κ / M-B line ratios for U = 1.8 are presented in Figure 2.9. In line with the previous results, the predictions from M-B exceed or are very similar to the predictions from κ models for most line ratios (this is, κ / M-B $\lesssim$ 1). The only exception is [O III] λ4363, for which the increase is > 1 when Z $\gtrsim$ 2Z$_\odot$.

In the optical regime, the impact of κ distributions depends on the metallicity: as the metallicity increases, κ / M-B approaches 1.

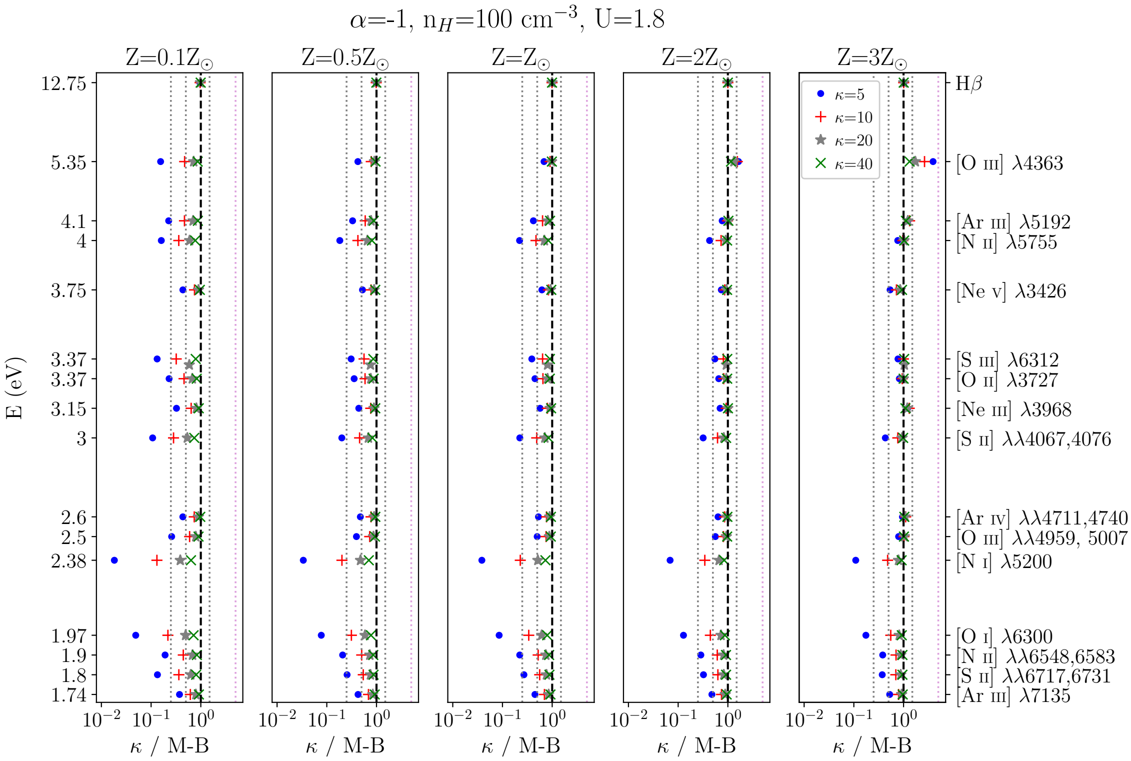

Figure 2.9: Same as Figure 2.7 but with U = 1.8.

2.3.3 UV emission lines

In general, when using κ distributions the UV emission line fluxes are enhanced (κ / M-B > 1) for a wide range of ionization and metallicity parameters. This is primarily due to the fact that the κ distributions place relatively more electrons at energies capable of exciting the UV lines, compared to the M-B distribution.

Figure 2.10 shows the predictions for $U = 1\times10^{-4}$. In comparison with a M-B distribution, κ distributions have high-energy tails, thus lines with high excitation energies are enhanced when κ distributions are assumed. This is particularly obvious for the UV lines with the highest excitation energies. The C III λ977 Å line which has an excitation energy of 12.7 eV, is strongly enhanced by the high-energy tail of κ distributions (see

Figure 2.2). Similar results are obtained for N III λ989 Å which has an excitation energy of 12.5 eV. The C III λ977 and N III λ989 line fluxes are enhanced for κ distributions for all metallicities considered. As the metallicity increases, κ / M-B > 1 for an increasing number of lines.

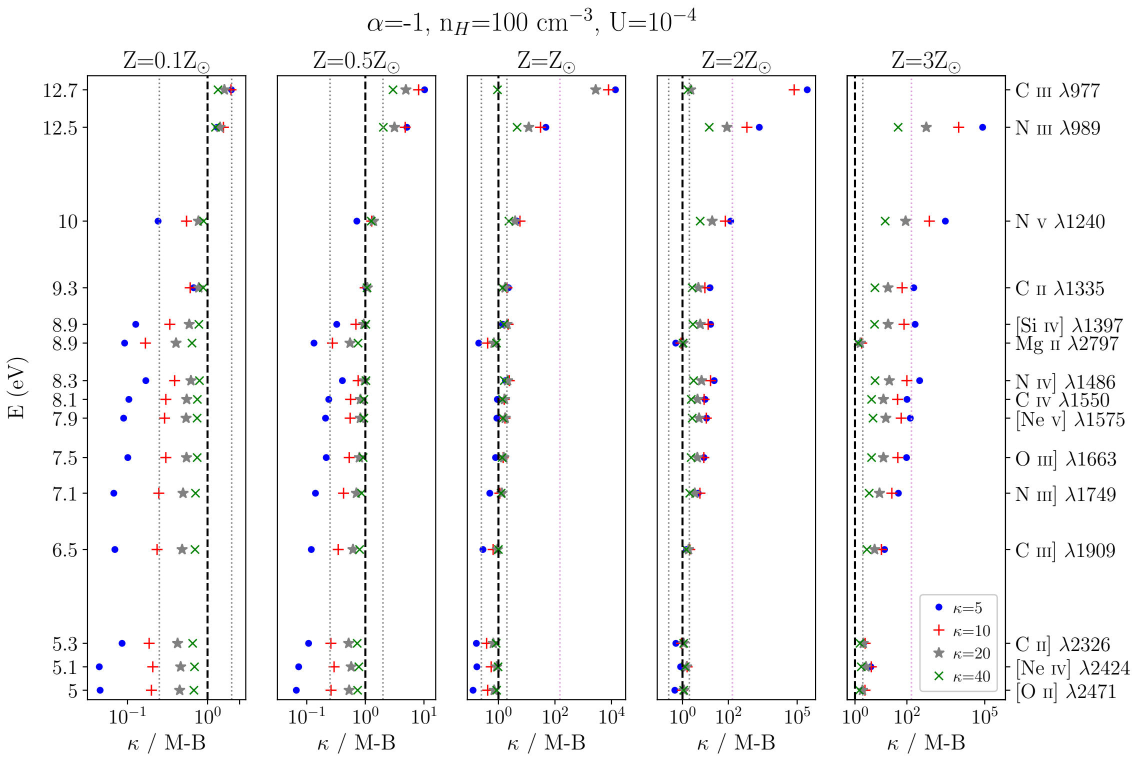

Figure 2.10: Ratios of model fluxes for κ and M-B electron energy distributions, for key nebular lines, arranged in order of increasing energy for $U = 1{\times}10^{-4}$. The grey dotted vertical lines mark the positions where κ / M-B is 0.25, and 2. The dashed line indicates where κ / M-B is 150. Note that at Z = 3Z$_{\odot}$, the ratio for the C IIIλ977 line is not shown, as its flux in the M-B model is too low.

Figure 2.11 shows the predictions for $U = 0.01$. As the ionization parameter increases, the magnitude of the line intensity enhancement from using a κ distributions diminishes. This is clearly seen in the calculated fluxes of C III λ977 and N III λ989, which are still enhanced for all metallicities when U is high, but the enhancement is now much smaller.

The other line fluxes also become less enhanced with increasing ionization parameter. They eventually reach a turnover point and then the enhancement becomes gradually stronger as can be seen in Figure 2.12. This turnover ionization parameter depends on the chosen electron energy distribution and on the emission line in question. For constant ionization parameter, as the metallicity increases we see increases in line fluxes when using κ distributions.

For $U = 1.8$ (Figure 2.12), the impact of κ distributions is strongly dependent on the gas metallicity. For low metallicities, no line fluxes show enhancements when κ distributions are used, and as the metallicity increases, UV lines become enhanced. Almost all ratios are enhanced (κ / M-B > 1) for κ distributions when $Z = 3Z_{\odot}$.

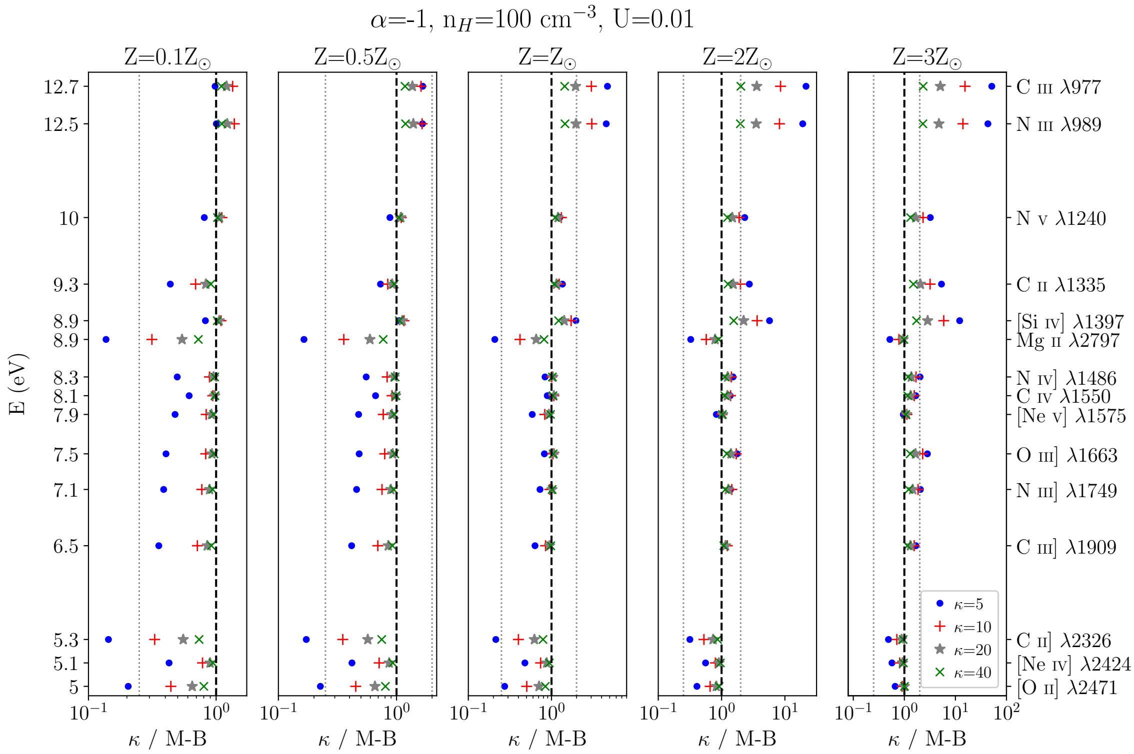

Figure 2.11: Same as Figure 2.10 but with $U = 0.01$.

Although H I Lyα λ1216 is often the most luminous of the UV emission lines, we omitted it from our analysis because it can be strongly affected by the presence of young stars (Villar-Martín et al., 2007a), resonance scattering effects (Villar-Martín et al., 1996), and contamination by O V] $\lambda\lambda$1213.8,1218.3 emission (Humphrey, 2019). These effects make the line unreliable for quantitative analyses of the kind performed herein.

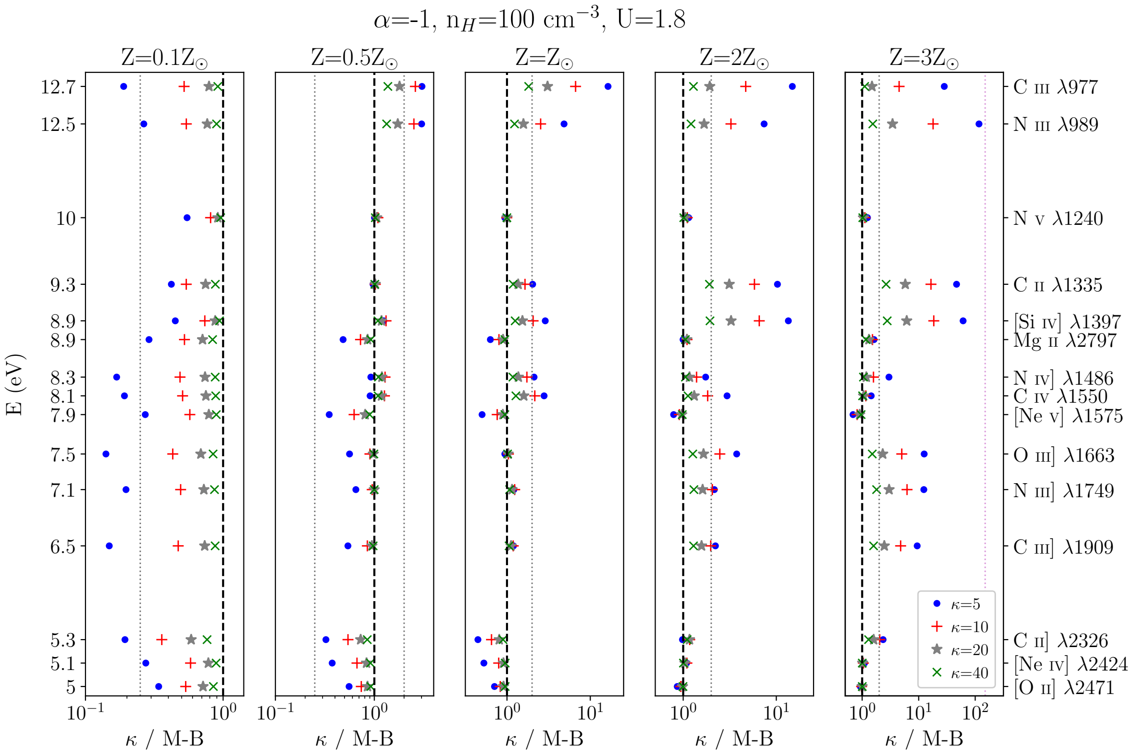

Figure 2.12: Same as Figure 2.10 but with U = 1.8.

Chapter 3

Application of the κ electron distribution models to high-z active galaxies

This chapter focuses primarily on the NLR and ENLR of type 2 AGN at z > 2. These regions are highly ionized, characterized by strong and narrow UV emission lines. After Lyα, the brightest UV lines emitted in these regions are N V $\lambda\lambda$1238,1242, C IV $\lambda\lambda$1548,1550, He II λ1640 and C III] $\lambda\lambda$1907,1909. Hereinafter, we will refer to these emission lines as N V λ1240, C IV λ1550, He II λ1640 and C III] λ1909. Line ratios of these lines are often used to constrain the density, metallicity and ionization properties of the gas in these regions (e.g., De Breuck et al., 2000; Villar-Martín et al., 1996; Villar-Martín et al., 1997; Villar-Martín et al., 2001; Villar-Martín et al., 2007a; Villar-Martín et al., 2008; Humphrey et al., 2008a; Nagao et al., 2006; Matsuoka et al., 2009). The gas in the NLR and the ENLR is believed to be ionized by the radiation field of an AGN (e.g., Osterbrock and Ferland, 2006) since the observed wide range of ionization stages cannot be produced by stars, requiring a source with a harder ionizing spectrum.

3.1 Sample

One of the goals of this work is to understand whether observed emission line ratios measured in the NLR of AGN are better reproduced using the M-B distribution or a κ distribution of electron energies. As a first step we compiled a sample of observed emission line fluxes from the literature. The data was compiled from Humphrey et al. (2008a), Silva et al. (2018), Silva et al. (2020), Solórzano-Iñarrea et al. (2004) and Vernet et al. (2001). It consists of 15 HzRGs, 126 QSO2, and two Seyfert galaxies: NGC 1068 (Kraemer et al., 1998) and NGC 3393 (Diaz et al., 1988). The original QSO2 sample had 144 galaxies but we excluded objects where less than 3 lines were observed. We include two Seyfert galaxies, observed at low redshift because unlike in most of the sample, a large number of emission lines were detected in their observations, including rest-frame UV lines.

In the following section, the predictions of the photoionization models described in Section 2.2.1 are compared with observed emission line ratios.

3.2 Results: diagnostic diagrams

The diagnostic diagrams are shown in Figures 3.1 - 3.5. Each line in the figures represents a sequence in ionization parameter, from U = 1×10^{-3} to U = 1.8, computed assuming a different distribution of electron energies. To make visualization easier, we show U = 1×10^{-3} as the lowest value for the ionization parameter because U = 1×10^{-4} is too low to reproduce the observed line ratios. For the same reason we will only show models computed using a power-law index of -1 and n_H = 100 cm^{-3}. A solid triangle indicates the lowest ionization parameter (U = 1×10^{-3}) and a pentagon indicates the highest ionization parameter for each model (U = 1.8).

Different photoionization models are represented using different colors and patterns. A solid black line represents models computed for a M-B distribution, a blue dashed line represents a κ distribution with κ = 5, the red line represents a κ distribution with κ =

10, magenta shows a κ distribution with κ = 20 and the dash-dotted green line denotes a κ distribution with κ = 40. Different objects of the selected sample are distinguished by different markers and colours: HzRGs are shown as pink stars, QSO2s as gold dots, NGC 1068 is represented by a cyan square and NGC 3393 by a green plus sign.

We start by showing predictions of the photoionization models in the standard [O III] λ5007 / Hβ versus [N II] λ6584 / Hα BPT (Baldwin, Phillips and Terlevich) diagnostic diagram (Baldwin et al., 1981). This diagram has been used for many years as a method to classify galaxies based on the dominant source of ionizing radiation (e.g., Kewley et al., 2001; Kauffmann et al., 2003; Sanders et al., 2023b; Perna et al., 2023).

Only NGC 3393 and a handful of HzRGs have reported measurements for these lines. At low metallicity (Z $\lesssim 0.5Z_\odot$), the models predict too low [O III] λ5007 / Hβ and [N II] λ6584 / Hα compared to the observations. The fit improves with increasing metallicity. When compared to the M-B distribution, κ distributions shift the ratios [O III] λ5007 / Hβ and [N II] λ6584 / Hα towards lower values for a given U.

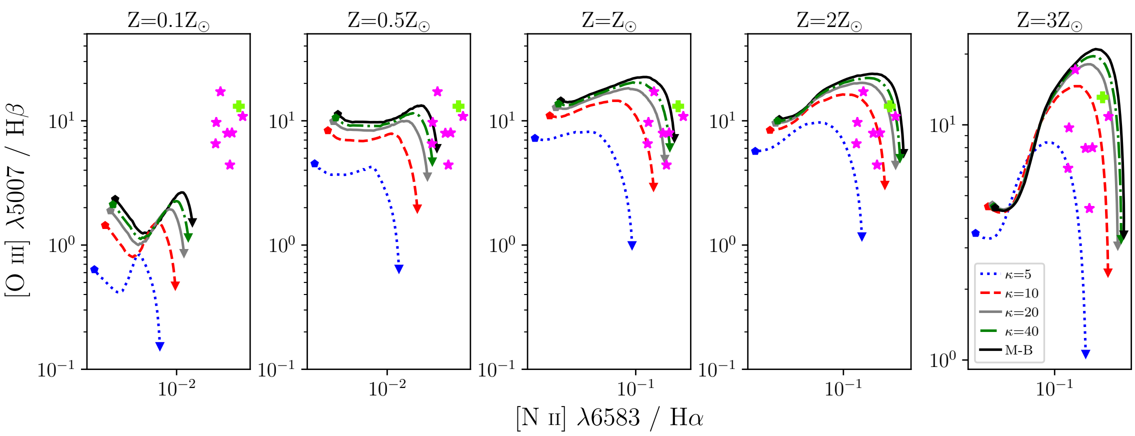

Figure 3.1: Comparison of the observed emission line ratios from the selected samples: HzRGs (pink stars) and NGC 3393 (green plus) with photoionization models using a power law index α = -1 and n_H = 100 cm^{-3}. Curves with different colors represent models computed assuming different electron energy distributions. The ionization parameter sequences increase from the triangle ($U = 1 \times 10^{-3}$) to the pentagon (U = 1.8) symbols.

In Figure 3.2 we show the diagnostic diagram N V λ1240 / He II λ1640 vs. N V λ1240 / C IV λ1550, often used as an abundance indicator (e.g., Hamann and Ferland, 1992; Hamann and Ferland, 1993; Villar-Martín et al., 2001). The shape of the curves is similar for models computed assuming κ and M-B distributions.

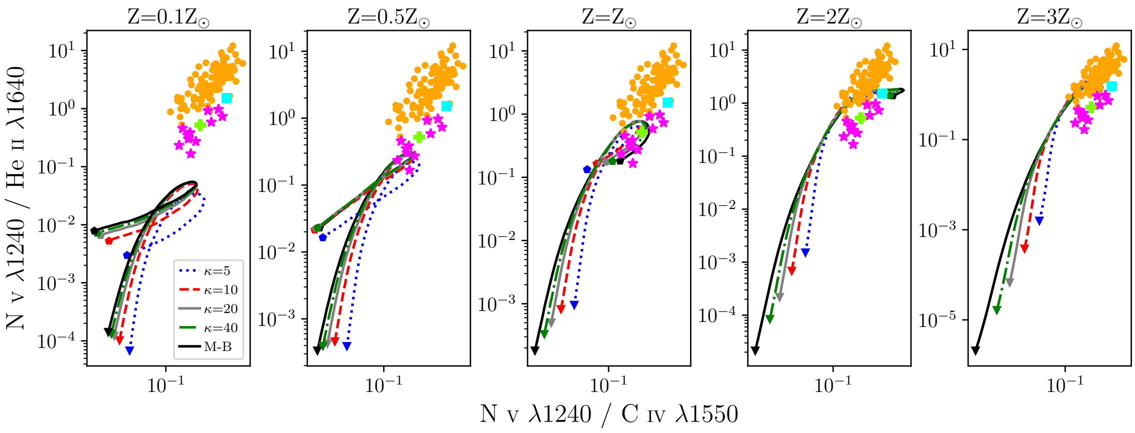

Figure 3.2: Diagnostic diagram N V λ1240 / He II λ1640 versus N V λ1240 / C IV λ1550. HzRGs are represented by pink stars, QSO2s by gold dots, NGC 1068 by a cyan square and NGC 3393 by a green plus.

Photoionization models assuming $Z = 0.1\ Z_{\odot}$ predict N V λ1240 / He II λ1640 ratios that are too low to reproduce any of the observations, independently of the electron energy distribution assumed. As the metallicity increases, the predicted N V λ1240 / He II λ1640 and N V λ1240 / C IV λ1550 ratios increase. At high metallicity ($Z \sim 3Z_{\odot}$) the models start to generate line ratios similar to those observed. For the same ionization parameter and $Z > 0.5Z_{\odot}$ κ distributions predict higher N V λ1240 / He II λ1640 than a M-B. This is especially clear for the low end of the ionization parameter sequences.

The diagnostic diagram showing C IV λ1550 / He II λ1640 as a function of C IV λ1550 / C III] λ1909 is presented in Figure 3.3. At low gas metallicity, and when compared to the M-B distribution, κ distributions shift the ratio C IV λ1550 / He II λ1640 to lower values. This situation reverses as the metallicity increases (and also for $Z = Z_{\odot}$ and high ionization parameter).

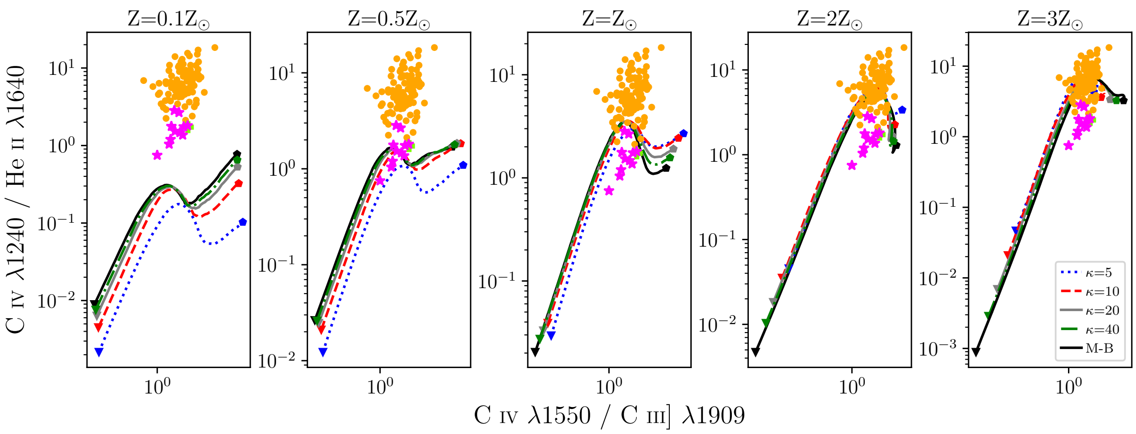

Figure 3.3: Diagnostic diagram C IV λ1550 / He II λ1640 as a function of C IV λ1550 / C III] λ1909. Symbols and lines as in Figure 3.1.

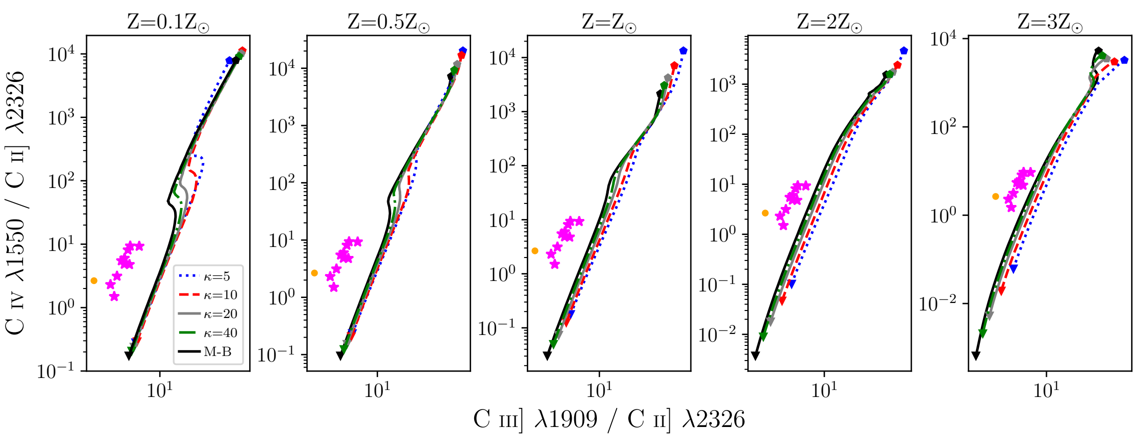

Figure 3.4: Diagnostic diagram C IV λ1550 / C II] λ2326 as a function of C III] λ1909 / C II] λ2326. Symbols and lines as in 3.1. Only one QSO2 had a reported C II] λ2326 measurement at the time of writing.

Figure 3.4 shows the predictions for the diagnostic diagram C IV λ1550 / C II] λ2326 as a function of C III] λ1909 / C II] λ2326. Compared to M-B distributions, the κ distributions predict higher C III] λ1909 / C II] λ2326 ratios. The data points lie far from the photoionization model predictions for all the parameter space considered. Compared to M-B distributions κ distributions produce a slightly inferior fit to the data.

Finally, the temperature diagnostic diagram [O III] λ5007 / Hβ vs. [O III] λ4363 / [O

III] λ5007 is presented in Figure 3.5.

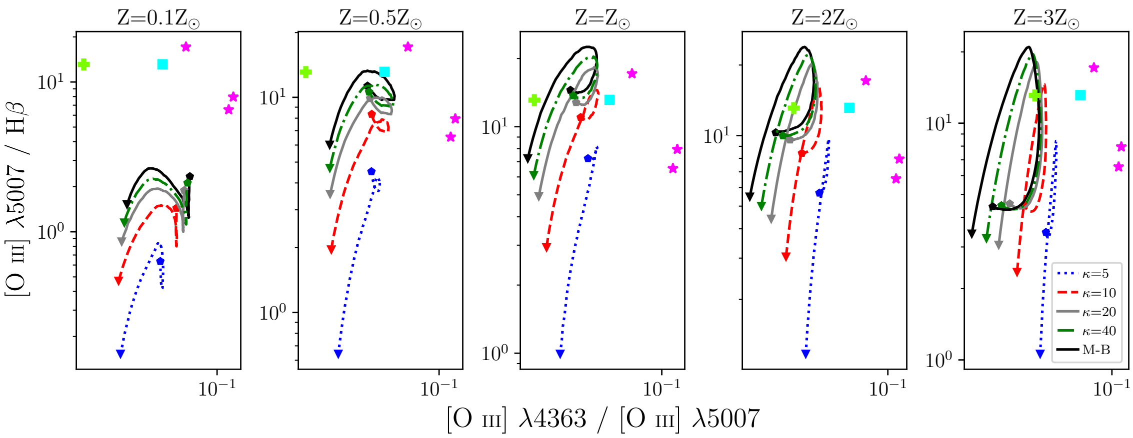

Figure 3.5: Diagram [O III] λ5007 / Hβ vs. [O III] λ4363 / [O III] λ5007.

Only the Seyfert galaxies and some HzRGs have detections of these lines. The predicted [O III] λ4363 / [O III] λ5007 ratios are too low to reproduce most of the observed line ratios. At high metallicities, $\kappa = 5$ distributions produce higher [O III] λ4363 / [O III] λ5007 than the M-B distributions but the ratio is still low compared to the observations. This is the long standing T_e problem of active galaxies (e.g., Tadhunter et al., 1989; Binette et al., 1996; Richardson et al., 2014).

3.3 Results: Models vs. observations

We created a Python code to find the best fitting model for each galaxy, using a brute-force χ^2 minimization. The code considers every possible line ratio from the data, and compares it with ratios calculated for the different photoionization models. The result is the best fit for each object. All possible line ratios from lines detected in each galaxy were used and all ratios are given equal weighting.

The parameters of the best-fitting models are shown in Tables 3.1, 3.2, and 3.3. For each object, in the first row we present the best-fitting M-B model, and in the second row the best-fitting κ-distribution model.

To simplify, we will henceforth adopt line notations that use only the chemical element and spectrum numeral, e.g., N V λ1240 becomes simply N V , and Si IV/ O IV] λ1402 becomes Si IV/ O IV]. Note that some line notations are not abbreviated, particularly in cases where their abbreviation is ambiguous (e.g., He II λ4686)

3.3.1 Seyfert 2 galaxies

In Table 3.1 the lines used in the minimization for the Seyfert 2 galaxies are presented.

Table 3.1: Best fit model parameters for a M-B distribution (first row) and the best fitting κ distribution (second row). (1) Object; (2) electron energy distribution; (3) spectral index of the ionizing continuum; (4) ionization parameter; (5) metallicity; (6) hydrogen density in cm^{-3}; (7) χ^2; (8) lines used in the fitting.

Object	EED	α	U	Z	n_H	χ^2	Emission lines used
	M-B	-1	0.004	$2Z_\odot$	10^4	4.2	N V , Si IV/O IV], N IV], C IV , He II, O III], N III], C III]+Si III] λ1892, [Ne IV], [O II] λ2470, Mg II ,
NGC 1068							[Ne V] $\lambda\lambda$3346,3426, [O II] λ3727, [Ne III] $\lambda\lambda$3869,3967, [S II] λ4072, [O III] λ4363, He II λ4686, Hβ,
	κ = 40	-1	0.0106	$2Z_\odot$	10^4	4.6	[O III] λ5007, [O I], [N II] $\lambda\lambda$6548,6584, Hα, [S II] $\lambda\lambda$6716,6731
	M-B	-1.5	0.009	$3Z_\odot$	100	8.1	N V , C IV , He II, C III], [Ne IV], Mg II , [O II] λ3727, [Ne III] λ3869,
NGC 3393							[Ne III] λ3969, [O III] λ4363, He II λ4686, [Ar IV] λ4740, [O III] $\lambda\lambda$4959,5007, [N I], [N II] λ6548,
	κ = 10	-1	0.007	$2Z_\odot$	100	6.3	Hα, [N II] λ6584, [S II] $\lambda\lambda$6717,6731, [Ar III]

In the case of NGC 1068, the best-fitting κ distribution model and the M-B model both have similar parameters, α = -1, $n_H = 10^4$ and $Z = 2Z_\odot$, with the exception of the ionization parameter, which is a factor of ~ 2 higher when a κ distribution is assumed ($U_{\text{M-B}}$ = 0.004, U_κ = 0.01). For the Seyfert galaxy NGC 3393, the situation is different: in this case, the best-fitting κ model and the M-B model have different parameters, with the exception of the gas density, for which the two values are similar.

3.3.2 HzRGs

Table 3.2 presents the parameters of the best-fitting photoionization models for the HzRGs.

Table 3.2: Best-fit model parameters for the HzRGs, assuming a M-B distribution (first row) and the best fitting κ distribution (second row). (1) Object; (2) electron energy distribution; (3) spectral index of the ionizing continuum; (4) ionization parameter; (5) metallicity; (6) hydrogen density in cm^{-3}; (7) χ^2; (8) lines used in the fitting.

Object	EED	α	U	Z	n_H	χ^2	Emission lines used
TXS 0211-122	M-B	-1	0.003	$Z_\odot$	100	24.2	N V , C IV , Si IV+O IV], Si IIλ1309, N IV], He II, O III], C III], [Ne IV], [Ne V] λ3426, [O II] λ3727, [Ne III] λ3869, [O III] λ4363, He II λ4686, [O III] λ4960, [O III] λ5007, [O I], [N II] λ6548, Hα, [N II] λ6583, [S II] $\lambda\lambda$6716,6731, Hβ
	κ = 10	-1	0.004	$2Z_\odot$	100	19.96	
MRC 0406-242	M-B	-1	0.0028	$2Z_\odot$	100	2.2	N V , Si IV+O IV], N IV], C IV , He II λ1640, OIII], C III], C II], [Ne IV], [Ne V] λ3426, [O II] λ3727, [Ne III] λ3869, He II λ4686, [O III] λ5007, Hβ
	κ = 40	-1	0.0045	$2Z_\odot$	100	2.5	
PKS 0529-549	M-B	-1	0.003	$Z_\odot$	100	2.9	[Ne V] λ3426, [O II] λ3727, [Ne III] λ3869, [O III] λ4363, He II λ4686, [O III] λ4960, [O III] λ5007, [O I], [N II] λ6548, Hα, [N II] λ6583, [S II] $\lambda\lambda$6716,6731, Hβ
	κ = 10	-1	0.006	$2Z_\odot$	100	2.6	
TXS 0828+193	M-B	-1	0.0045	$0.5Z_\odot$	10^4	15.17	N V , Si IV+O IV], Si IIλ1309, C II, N IV], C IV , [Ne V] λ1575, [Ne IV] λ1602, He II λ1640, O III], N III], Si III], C III], C II], [Ne IV], [Ne V] λ3426, [O II] λ3727, [O III] λ4363, He II λ4686, [O III] λ5007, Hβ
	κ = 5	-1	0.005	$0.5Z_\odot$	100	11.48	
MRC 1138-262	M-B	-1.5	0.002	$3Z_\odot$	100	0.8	[O II] λ3727, [Ne III] λ3869, He II λ4686, [O III] λ4960, [O III] λ5007, [O I] λ6300, [N II] λ6548, Hα, [N II] λ6583, [S II] $\lambda\lambda$6716,6731, Hβ
	κ = 10	-1	0.0008	$Z_\odot$	10^4	0.7	
4C-00.54	M-B	-1.5	0.01	$Z_\odot$	100	7.2	N V , Si IV+O IV], C II, C IV , He II λ1640, O III], C III], C II], [Ne IV], [O II] λ3727, [O III] λ4363, He II λ4686, [O III] λ4960, [O III] λ5007, [O I], [N II] λ6548, Hα, [N II] λ6583, [S II] $\lambda\lambda$6716,6731, Hβ
	κ = 40	-1.5	0.015	$2Z_\odot$	100	6.5	
USS 1558-003	M-B	-1	0.0035	$Z_\odot$	100	5.3	N V , Si IV+O IV], N IV], C IV , He II λ1640, O III], C III], C II], [Ne V] λ3426, [O II] λ3727, [Ne III] λ3869, He II λ4686, [O III] λ4960, [O III] λ5007, [O I], [N II] λ6548, Hα, [N II] λ6583, [S II] $\lambda\lambda$6716,6731, Hβ
	κ = 10	-1	0.005	$Z_\odot$	100	3.4	
4C+40.36	M-B	-1	0.0017	$Z_\odot$	10^4	15.7	N V , Si IV+O IV], Si II, C II, N IV], C IV , He II λ1640, O III], N III], C III], C II], [Ne IV], [O II] λ2471, [O II] λ3727, [Ne III] λ3869, He II λ4686, [O III] λ5007, [O I], [N II] λ6548, Hα, [N II] λ6583, [S II] $\lambda\lambda$6716,6731, Hβ
	κ = 10	-1	0.003	$2Z_\odot$	100	11.4	
4C+23.56	M-B	-1.5	0.004	$2Z_\odot$	100	6.6	N V , Si IV+O IV], N IV], C IV , He II λ1640, O III], C III], C II], [Ne IV], [Ne V] λ3426, [O II] λ3727, [Ne III] λ3869, He II λ4686, [O III] λ4960, [O III] λ5007, [O I], [N II] λ6548, Hα, [N II] λ6583, [S II] $\lambda\lambda$6716,6731, Hβ
	κ = 40	-1.5	0.0065	$2Z_\odot$	100	7.5	
0850-206	M-B	-1	0.004	$0.5Z_\odot$	100	4.93	He II λ1640, N III], Si III], C III], C II], [Ne IV], [O II] λ2471, Mg II , [Ne V] λ3346, [Ne V] λ3426, [O II] λ3727
	κ = 40	-1	0.006	$0.5Z_\odot$	100	5.7	
1303+091	M-B	-1	0.0035	$Z_\odot$	10^4	1.8	C IV , He II λ1640, O III], Si III], C III], C II], [Ne IV], [O II] λ2471, Mg II , [Ne V] λ3346, [Ne V] λ3426
	κ = 40	-1	0.0045	$Z_\odot$	10^4	2.1	
4C+03.24	M-B	-1	0.0065	$2Z_\odot$	10^6	3.8	N V , C II, Si IV+O IV], C IV , He II λ1640
	κ = 5	-1	0.0065	$3Z_\odot$	10^6	1.5	
0731+438	M-B	-1	0.0045	$0.5Z_\odot$	10^4	10.2	N V , Si II, C II, Si IV+O IV], N IV], C IV , He II λ1640, O III], Si III] $\lambda\lambda$1882,1892, C III], C II], [Ne IV] λ2422
	κ = 5	-1	0.0045	$Z_\odot$	100	5.98	
4C+48.48	M-B	-1	0.01	$2Z_\odot$	100	2.44	N V , C II, Si IV+O IV], N IV], C IV , He II λ1640, O III], C III], C II], [Ne IV] λ2422
	κ = 40	-1	0.012	$2Z_\odot$	100	2.26	
MRC 0943-242	M-B	-1	0.0035	$Z_\odot$	100	2.2	N V , C IV , He II λ1640, C III], C II], [Ne IV], Mg II , [Ne V] λ3426, [O II] λ3727, [Ne III] λ3869, [O III] λ4363, [O III] λ4960, [O III] λ5007
	κ = 40	-1	0.0065	$Z_\odot$	100	2.4	

The best fitting distribution varies from object to object. Five of the HzRGs are best fitted by a M-B distribution, and the other ten are best fitted by κ distributions, with varying κ indices (see Figure 3.6).

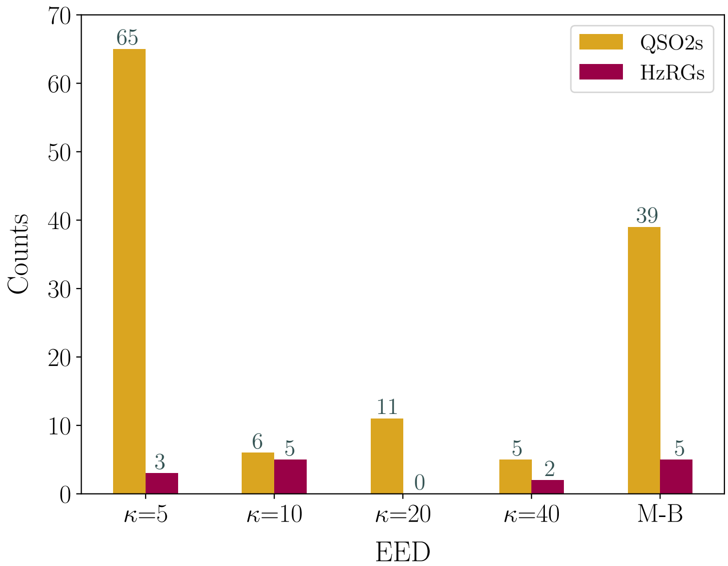

Figure 3.6: Number of objects (HzRGs and QSO2s) according to the best fitting electron energy distribution.

In Figure 3.7 we show the distribution of HzRGs with respect to the discrepancy in the model parameters between the best-fitting κ and M-B EED models. Here, the discrepancy is expressed as the ratio between the value of the parameter in the best-fitting κ distribution model, and the value of same the parameter in parameter in the best-fitting M-B model.

In general, the HzRGs are best fitted by photoionization models with α = -1. The decision to adopt either a κ or M-B distribution has no apparent impact on the inferred spectral index, α, in most HzRGs (14/15 or 93%; Figure 3.7, panel (a)).

Panel (b) of Figure 3.7 shows how the choice of EED affects the predicted gas density. Assuming a κ distribution instead of a M-B has no apparent impact on the inferred density in 73% of the HzRGs. In these sources, the best-fitting κ and the M-B models both have n_H = 100 cm^{-3}.

Panel (c) of Figure 3.7 presents the results for the metallicity. In 93% of the HzRGs (14 sources), κ models produce identical or higher Z than the M-B models. The metallicities of the best-fitting κ and M-B models are consistent in 53% of cases ($Z_\kappa / Z_{\text{M-B}} = 1$).

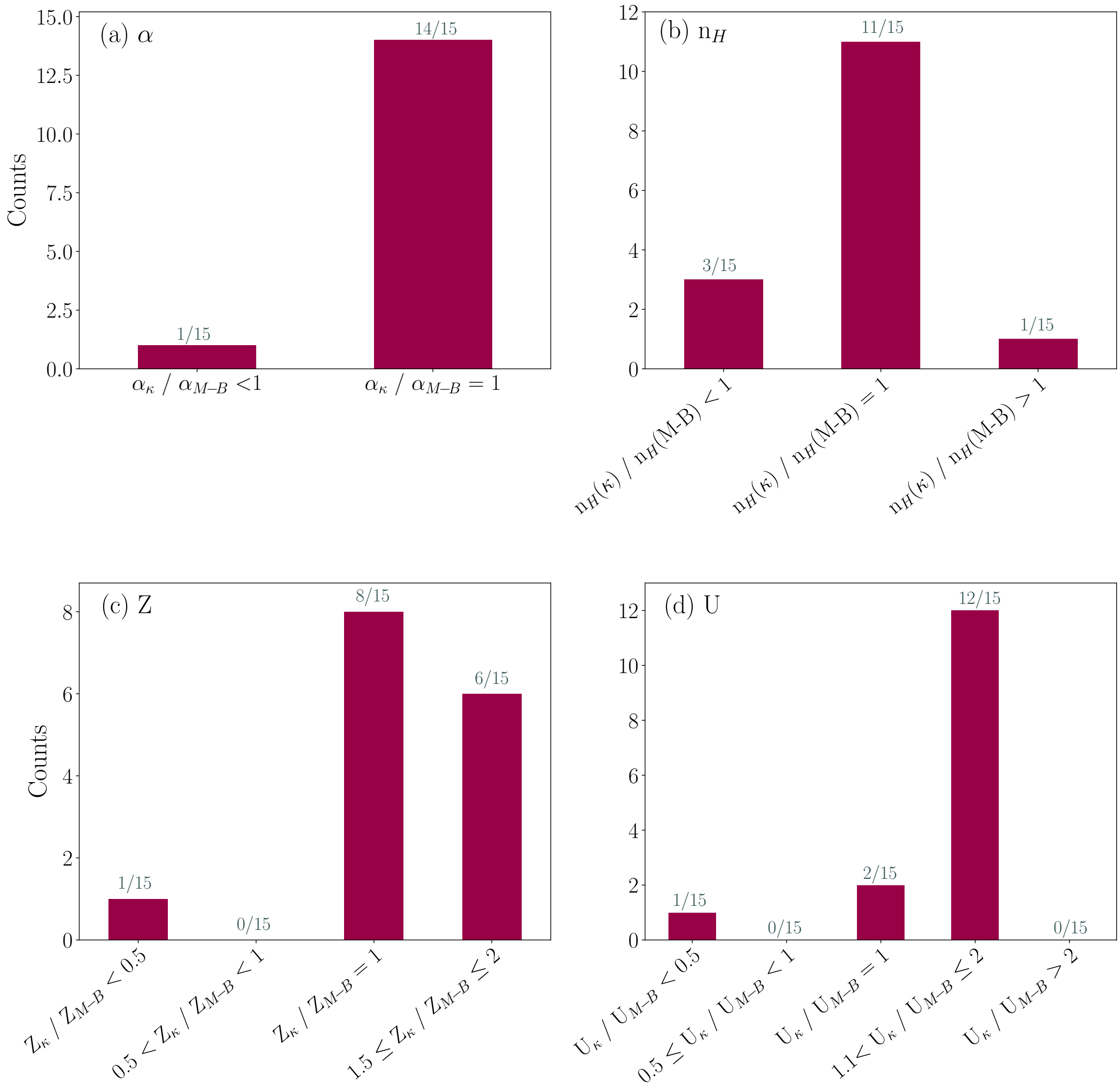

Figure 3.7: HzRGs binned according to discrepancy in (a) α, (b) n_H, (c) Z, and (d) U between κ and M-B distributions.

In 40% of the HzRGs, the metallicity value of the best-fitting κ model is a factor of 1.5 to 2 higher than in the best-fitting M-B model. In the case of only one of the HzRGs did we find a large discrepancy in the metallicity value (Z_κ / $Z_{\text{M-B}} < 0.5$).

Figure 3.7, panel (d) presents the ratio U_κ / $U_{\text{M-B}}$. In 93% of cases (14 HzRGs), the best fitting κ distribution model has an ionization parameter value that is 1.1 to 2 times higher than the value in the best-fitting M-B model. A large discrepancy in this parameter (U_κ / $U_{\text{M-B}} < 0.5$) between the two best-fitting models is found for one HzRG.

3.3.3 Type 2 quasars at z > 2

The best fitting parameters for the QSO2s are presented in Tables 3.3.

Table 3.3: Best fit model parameters for the QSO2s. The first row shows the parameters when a M-B distribution is used and the second row shows the best fitting κ distribution and its parameters. (1) Object; (2) electron energy distribution; (3) spectral index of the ionizing continuum; (4) ionization parameter; (5) metallicity; (6) hydrogen density in cm^{-3}; (7) χ^2; (8) lines used in the fitting.

Object	EED	α	U	Z	n_H	χ^2	Emission lines used
SDSS J011506.65	M-B	-1	0.0065	$Z_\odot$	10^4	22.2	N V , O I, Si IV+O IV], C IV , He II, Si III], C III]
	$\kappa = 5$	-1	0.005	$3Z_\odot$	10^4	17.5	
SDSS J022051.68	M-B	-1	0.012	$Z_\odot$	10^4	20.4	N V , O I, Si IV+O IV], C IV , He II, N III], C III]
	$\kappa = 5$	-1	0.0106	$2Z_\odot$	10^4	16.6	
SDSS J075119.09	M-B	-1	0.0065	$Z_\odot$	10^4	15.7	N V , O I, Si IV+O IV], C IV , He II, C III]
	$\kappa = 5$	-1	0.005	$3Z_\odot$	10^4	10.9	
SDSS J091025.50	M-B	-1	0.012	$Z_\odot$	10^4	17.6	O VI +C II, N V , O I, Si IV+O IV], N IV], C IV , He II, N III], C III]
	$\kappa = 5$	-1	0.012	$Z_\odot$	10^4	14.6	
SDSS J023337.89	M-B	-1	0.004	$0.1Z_\odot$	100	9.5	N V , O I, C IV
	$\kappa = 5$	-1	0.004	$3Z_\odot$	100	5.9	
SDSS J074725.50	M-B	-1	0.036	$Z_\odot$	100	0.24	O VI +C II, N V , C IV , He II, O III], C III]
	$\kappa = 5$	-1	0.036	$Z_\odot$	100	0.1	
SDSS J080428.80	M-B	-1	0.008	$Z_\odot$	100	22.2	N V ,OI, Si IV+O IV], C IV , He II, C III]
	$\kappa = 5$	-1	0.008	$2Z_\odot$	100	16.8	
SDSS J080826.02	M-B	-1	0.00276	$2Z_\odot$	10^4	10.8	O I, Si IV+O IV], C IV , He II, O III], C III]
	$\kappa = 5$	-1	0.0035	$3Z_\odot$	100	8.2	
SDSS J081812.72	M-B	-1	0.008	$Z_\odot$	10^4	25.5	N V , O I, C IV , He II, O III], C III]
	$\kappa = 5$	-1	0.008	$Z_\odot$	10^4	20.7	

Tables 3.3 - - *Continued*

Object	EED	α	U	Z	n_H	χ^2	Emission lines used
SDSS J082550.58	M-B	-1	0.0136	$0.5Z_\odot$	10^4	28.6	O VI +C II, N V , O I, Si IV+O IV], C IV , He II, C III]
	$\kappa = 5$	-1	0.015	$Z_\odot$	10^4	27.1	
SDSS J083246.92	M-B	-1	0.0035	$0.1Z_\odot$	10^6	16.01	N V , O I, C IV , [Ne IV] λ1602, C III], [Ne IV] λ2422
	$\kappa = 5$	-1	0.0035	$0.1Z_\odot$	10^6	9.4	
SDSS J083851.81	M-B	-1	0.008	$0.5Z_\odot$	10^4	25.8	O VI +C II, N V , O I, C IV , He II, C III]
	$\kappa = 5$	-1	0.008	$Z_\odot$	10^4	22.97	
SDSS J094308.14	M-B	-1	0.0058	$Z_\odot$	100	35.02	N V , O I, Si IV+O IV], C IV , He II, O III], C III]
	$\kappa = 5$	-1	0.0058	$Z_\odot$	100	25.5	
SDSS J094826.45	M-B	-1	0.0058	$Z_\odot$	10^4	20.9	N V , O I, Si IV+O IV], C IV , He II, O III], C III], Mg II
	$\kappa = 5$	-1	0.005	$3Z_\odot$	10^4	11.9	
SDSS J100210.53	M-B	-1	0.015	$Z_\odot$	100	39.6	O VI +C II, N V , O I, Si IV+O IV], C IV , He II, O III], C III]
	$\kappa = 5$	-1	0.015	$2Z_\odot$	100	28.98	
SDSS J084949.57	M-B	-1	0.009	$Z_\odot$	100	26.4	O VI +C II, N V , O I, C IV , He II, O III]
	$\kappa = 5$	-1	0.004	$3Z_\odot$	10^4	13.2	
SDSS J113351.03	M-B	-1	0.005	$0.5Z_\odot$	10^4	11.4	O VI +C II, N V , O I, C IV , He II, O III], Si III], C III]
	$\kappa = 5$	-1	0.0035	$3Z_\odot$	10^4	8.5	
SDSS J104133.36	M-B	-1	0.008	$Z_\odot$	10^4	20.99	N V , O I, Si IV+O IV], C IV , He II, C III], Mg II
	$\kappa = 5$	-1	0.00736	$3Z_\odot$	10^4	16.1	
SDSS J105324.11	M-B	-1	0.0136	$Z_\odot$	100	19.5	N V , O I, Si IV+O IV], C IV , He II, OIII], C III], Mg II
	κ=5	-1	0.012	$2Z_\odot$	100	14.1	
SDSS J115335.78	M-B	-1	0.0106	$Z_\odot$	100	13.5	O VI +C II, N V , O I, Si IV+O IV], N IV], C IV , He II, O III], C III]
	$\kappa = 5$	-1	0.0106	$Z_\odot$	100	11.3	
SDSS J115411.95	M-B	-1	0.009	$Z_\odot$	10^4	23.1	O VI +C II, N V , O I, C IV , He II, O III], C III]
	$\kappa = 5$	-1	0.009	$2Z_\odot$	10^4	19.1	
SDSS J114856.13	M-B	-1	0.0065	$Z_\odot$	10^4	21.03	N V , O I, C IV , He II, C III], Mg II
	$\kappa = 5$	-1	0.0058	$3Z_\odot$	10^4	16.5	
SDSS J115510.34	M-B	-1	0.009	$0.5Z_\odot$	10^4	20.1	N V , O I, C IV , He II, Si III], CIII], Mg II
	$\kappa = 5$	-1	0.0065	$3Z_\odot$	10^4	18.4	
SDSS J140625.75	M-B	-1	0.012	$Z_\odot$	100	31.03	O VI +C II, N V , O I, C IV , He II, O III], C III]
	$\kappa = 5$	-1	0.014	$2Z_\odot$	100	23.7	
SDSS J141114.21	M-B	-1	0.007	$0.1Z_\odot$	100	17.7	O VI +C II, N V , O I, C IV , Si III, C III]
	$\kappa = 5$	-1	0.007	$0.1Z_\odot$	100	13.04	
SDSS J122214.45	M-B	-1.5	0.156	$2Z_\odot$	100	0.05	O VI +C II, N V , C IV , He II, C III]
	$\kappa = 20$	-1.5	0.02	$3Z_\odot$	100	0.07	
SDSS J012552.08	M-B	-1	0.066	$2Z_\odot$	10^6	2.0	O VI +C II, N V , Si IV+O IV], C IV , He II, C III]
	$\kappa = 40$	-1	0.1	$2Z_\odot$	10^6	2.0	
SDSS J091301.33	M-B	-1.5	0.138	$2Z_\odot$	10^4	0.07	O VI +C II, N V , C IV , C III]
	$\kappa = 5$	-1	0.04	$2Z_\odot$	10^6	0.02	

Tables 3.3 - - *Continued*

Object	EED	α	U	Z	n_H	χ^2	Emission lines used
SDSS J141853.65	M-B	-1	0.002	$Z_\odot$	10^4	8.2	O I, C IV , He II, O III], Si III], C III]
	$\kappa = 5$	-1	0.002	$2Z_\odot$	10^4	6.3	
SDSS J144441.05	M-B	-1	0.12	$3Z_\odot$	10^4	2.5	N V , C IV , He II, C III]
	$\kappa = 5$	-1	1.2	$2Z_\odot$	10^6	2.4	
SDSS J151747.00	M-B	-1	0.007	$0.5Z_\odot$	10^4	10.7	O VI +C II, N V , O I, C IV , He II, O III], C III]
	$\kappa = 5$	-1	0.0065	$Z_\odot$	10^4	8.2	
SDSS J151815.55	M-B	-1	0.0106	$Z_\odot$	10^4	50.3	O VI +C II, N V , O I, C IV , [Ne IV] λ1602, He II, O III], C III]
	$\kappa = 5$	-1	0.0106	$2Z_\odot$	10^4	44.07	
SDSS J152051.00	M-B	-1	0.008	$Z_\odot$	100	12.1	O VI +C II, N V , O I, Si IV+O IV], N IV], C IV , He II, O III], C III]
	$\kappa = 5$	-1	0.008	$Z_\odot$	100	9.6	
SDSS J152105.83	M-B	-1	0.0045	$Z_\odot$	10^4	6.9	N V , O I, Si IV+O IV], N IV], C IV , He II, O III], Si III], C III]
	$\kappa = 5$	-1	0.004	$2Z_\odot$	10^4	5.7	
SDSS J100345.59	M-B	-1	0.41	$2Z_\odot$	10^4	0.008	N V , C IV , C III]
	$\kappa = 5$	-1	0.37	$3Z_\odot$	100	0.0001	
SDSS J161343.40	M-B	-1	0.009	$Z_\odot$	10^4	19.3	O VI +C II, N V , O I, C IV , He II, O III], C III]
	$\kappa = 5$	-1	0.009	$Z_\odot$	10^4	15.5	
SDSS J162327.66	M-B	-1	0.012	$Z_\odot$	10^4	23.1	N V , O I, Si IV+O IV], C IV , [Ne IV] λ1602, He II, O III], Si III], C III], [Ne IV] λ2422
	$\kappa = 5$	-1	0.012	$Z_\odot$	10^4	22.2	
SDSS J165525.54	M-B	-1	0.009	$Z_\odot$	10^4	32.2	O VI +C II, N V , O I, Si IV+O IV], C IV , He II, O III], C III]
	$\kappa = 5$	-1	0.0106	$2Z_\odot$	10^4	21.2	
SDSS J170558.64	M-B	-1	0.007	$Z_\odot$	10^4	14.1	N V , O I, Si IV+O IV], C IV , He II, N III], Si III], C III], Mg II
	$\kappa = 5$	-1	0.0065	$3Z_\odot$	10^4	12.4	
SDSS J150451.51	M-B	-1	0.007	$Z_\odot$	10^4	25.4	O VI +C II, N V , O I, Si IV+O IV], C IV , He II, C III]
	$\kappa = 5$	-1	0.005	$3Z_\odot$	10^4	19.6	
SDSS J230451.68	M-B	-1	0.012	$Z_\odot$	10^4	33.1	O VI +C II, N V , O I, Si IV+O IV], C IV , He II, N III]
	$\kappa = 5$	-1	0.012	$3Z_\odot$	10^4	23.2	
SDSS J234612.64	M-B	-1	0.005	$0.1Z_\odot$	100	11.4	N V , O I, C IV , Si III], C III], Mg II
	$\kappa = 5$	-1	0.005	$0.1Z_\odot$	100	5.7	
SDSS J214609.96	M-B	-1	0.0058	$0.1Z_\odot$	100	57.9	O VI +C II, O I, C IV , C III]
	$\kappa = 5$	-1	0.0058	$0.1Z_\odot$	100	33.9	
SDSS J220126.11	M-B	-1	0.0065	$0.1Z_\odot$	100	18.4	N V , O I, C IV , C III]
	$\kappa = 5$	-1	0.0065	$0.1Z_\odot$	100	12.7	
SDSS J155200.53	M-B	-1	0.002	$2Z_\odot$	10^4	16.9	O I, C IV , He II, O III], Si III], C III]
	$\kappa = 5$	-1	0.002	$3Z_\odot$	10^4	11.9	
SDSS J160103.85	M-B	-1	0.0058	$Z_\odot$	10^4	16.6	N V , O I, C IV , He II, Si III], CIII], Mg II
	$\kappa = 5$	-1	0.005	$3Z_\odot$	10^4	12.6	
SDSS J223348.09	M-B	-1	0.0065	$0.1Z_\odot$	10^6	19.4	N V , O I, Si IV+O IV], C IV , [Ne IV] λ1602, Si III], C III], [Ne IV] λ2422
	$\kappa = 5$	-1	0.0065	$0.1Z_\odot$	10^6	15.4	
SDSS J075656.49	M-B	-1	0.007	$0.5Z_\odot$	10^4	21.95	O VI +C II, N V , O I, Si IV+O IV], C IV , [Ne IV] λ1602,
	$\kappa = 40$	-1	0.0106	$0.5Z_\odot$	10^4	22.8	He II, N III], Si III], C III], [Ne IV] λ2422
SDSS J112230.35	M-B	-1	0.108	$Z_\odot$	10^6	1.6	N V , Si IV+O IV], C IV , [Ne IV] λ1602,
	$\kappa = 40$	-1	0.06	$0.5Z_\odot$	10^6	1.6	He II, C III], [Ne IV] λ2422

Tables 3.3 - - *Continued*

Object	EED	α	U	Z	n_H	χ^2	Emission lines used
SDSS J212951.40	M-B	-1	0.0065	$0.1Z_\odot$	100	17.6	O VI +C II, N V , O I, C IV , N III], Si III], C III]
	$\kappa = 5$	-1	0.0065	$0.1Z_\odot$	100	12.6	
SDSS J120835.95	M-B	-1	0.4	$3Z_\odot$	10^6	0.05	N V , C IV , C III]
	$\kappa = 5$	-1.5	1.8	$3Z_\odot$	100	0.004	
SDSS J074251.43	M-B	-1.5	0.05	$Z_\odot$	100	0.02	O VI +C II, N V , C IV , C III]
	$\kappa = 5$	-1.5	0.096	$2Z_\odot$	10^4	0.004	
SDSS J082530.67	M-B	-1	0.25	$2Z_\odot$	10^6	0.09	N V , C IV , He II, C III]
	$\kappa = 10$	-1	0.37	$3Z_\odot$	10^4	0.1	
SDSS J100133.85	M-B	-1	0.2	$3Z_\odot$	10^6	0.04	N V , C IV , He II, C III]
	$\kappa = 10$	-1	0.176	$3Z_\odot$	10^6	0.008	
SDSS J133927.80	M-B	-1	0.0065	$0.5Z_\odot$	10^4	11.1	N V , O I, N IV], C IV , [Ne IV] λ1602, He II, O III], Si III], C III], [Ne IV] λ2422
	$\kappa = 10$	-1	0.0065	$0.5Z_\odot$	10^4	11.1	
SDSS J150145.46	M-B	-1	0.29	$3Z_\odot$	10^6	0.2	N V , C IV , He II, C III]
	$\kappa = 10$	-1	0.29	$3Z_\odot$	10^4	0.2	
SDSS J123742.37	M-B	-1	0.25	$2Z_\odot$	10^6	0.0002	N V , C IV , C III]
	$\kappa = 10$	-1	0.37	$3Z_\odot$	10^4	8E-6	
SDSS J114542.07	M-B	-1	0.066	$3Z_\odot$	10^6	2.6	O VI +C II, N V , Si IV+O IV], N IV], C IV , He II, O III], N III], C III]
	$\kappa = 10$	-1	0.059	$3Z_\odot$	10^4	2.5	
SDSS J131659.84	M-B	-1.5	0.22	$2Z_\odot$	10^4	0.006	O VI +C II, N V , C IV , C III]
	$\kappa = 10$	-1.5	0.138	$2Z_\odot$	100	0.002	
SDSS J213843.08	M-B	-1.5	0.14	$Z_\odot$	10^4	0.2	O VI +C II, N V , C IV , He II, O III], C III]
	$\kappa = 10$	-1	0.05	$Z_\odot$	10^4	0.2	
SDSS J104722.99	M-B	-1	0.08	$3Z_\odot$	10^6	0.56	O VI +C II, N V , C IV , C III]
	$\kappa = 10$	-1.5	0.2	$3Z_\odot$	10^4	0.57	
SDSS J161058.48	M-B	-1.5	0.3	$3Z_\odot$	10^4	0.003	N V , C IV , C III]
	$\kappa = 10$	-1	0.2	$2Z_\odot$	100	0.0006	
SDSS J004423.20	M-B	-1	0.022	$2Z_\odot$	10^6	0.4	N V , C IV , He II, O III], C III]
	$\kappa = 10$	-1.5	0.86	$2Z_\odot$	10^6	0.3	
SDSS J221601.21	M-B	-1	0.3	$2Z_\odot$	10^4	0.0003	N V , C IV , C III]
	$\kappa = 20$	-1	1.1	$3Z_\odot$	10^4	0.0001	
SDSS J163343.85	M-B	-1	0.0065	$Z_\odot$	10^4	16.7	O VI +C II, N V , O I, C IV , [Ne IV] λ1602, He II, Si III], C III], [Ne IV] λ2422
	$\kappa = 20$	-1	0.00736	$Z_\odot$	10^4	16.2	
SDSS J115947.86	M-B	-1	0.25	$3Z_\odot$	10^4	0.2	N V , C IV , He II, C III]
	$\kappa = 20$	-1	0.156	$3Z_\odot$	10^4	0.1	
SDSS J103249.55	M-B	-1	0.0065	$Z_\odot$	10^4	18.8	N V , O I, Si IV+O IV], C IV , [Ne IV] λ1602, He II, SiIII], C III], [Ne IV] λ2422, Mg II
	$\kappa = 20$	-1	0.00736	$Z_\odot$	10^4	18.1	
SDSS J091357.87	M-B	-1	0.2	$3Z_\odot$	10^4	0.35	O VI +C II, N V , C IV , He II, C III]
	$\kappa = 20$	-1	0.156	$3Z_\odot$	10^4	0.3	
SDSS J151544.01	M-B	-1	0.25	$2Z_\odot$	10^6	0.56	N V , Si IV+O IV], N IV], C IV , He II, O III], C III]
	$\kappa = 20$	-1	0.096	$2Z_\odot$	100	0.6	
SDSS J161447.97	M-B	-1	0.046	$Z_\odot$	10^4	0.27	N V , C IV , He II, O III], C III]
	$\kappa = 20$	-1	0.05	$Z_\odot$	10^4	0.26	
SDSS J162500.57	M-B	-1	0.4	$3Z_\odot$	10^4	0.0008	N V , C IV , He II
	$\kappa = 20$	-1	0.29	$3Z_\odot$	10^4	0.0002	

Tables 3.3 - - *Continued*

Object	EED	α	U	Z	n_H	χ^2	Emission lines used
SDSS J105344.18	M-B	-1	0.075	$3Z_\odot$	10^4	0.4	O VI +C II, N V , C IV , He II, C III]
	κ = 20	-1.5	0.176	$3Z_\odot$	10^4	0.38	
SDSS J081257.15	M-B	-1	0.03	$Z_\odot$	100	0.25	N V , C IV , He II, C III]
	κ = 20	-1.5	1.8	$2Z_\odot$	10^4	0.05	
SDSS J162651.76	M-B	-1	0.032	$Z_\odot$	10^6	0.02	N V , C IV , He II, C III]
	κ = 20	-1.5	0.2	$2Z_\odot$	10^4	0.003	
SDSS J212055.57	M-B	-1	0.0058	$Z_\odot$	10^4	13.5	N V , O I, Si IV+O IV], C IV , [Ne IV] λ1602, He II, Si III], C III], [Ne IV] λ2422, Mg II
	κ = 20	-1	0.0065	$Z_\odot$	10^4	13.1	
SDSS J160158.53	M-B	-1	0.1	$3Z_\odot$	10^6	0.19	O VI +C II, N V , C IV , He II, C III]
	κ = 40	-1	0.1	$3Z_\odot$	10^6	0.22	
SDSS J020728.19	M-B	-1	0.008	$Z_\odot$	10^4	12.6	O VI +C II, N V , O I, Si IV+O IV], C IV , He II, O III], N III], Si III], C III]
	κ = 40	-1	0.012	$Z_\odot$	10^4	12.5	
SDSS J083031.86	M-B	-1	0.0065	$0.1Z_\odot$	10^6	1.9	O VI +C II, N V , C IV , [Ne IV] λ1602, Si III], C III], [Ne IV] λ2422
	κ = 40	-1	0.01	$0.1Z_\odot$	10^6	2.06	
SDSS J162025.94	M-B	-1	0.0136	$0.5Z_\odot$	10^6	4.9	N V , C IV , [Ne IV] λ1602, He II, O III], Si III], C III], [Ne IV] λ2422, Mg II
	κ = 40	-1	0.02	$0.5Z_\odot$	10^6	5.3	
SDSS J162806.01	M-B	-1	0.009	$0.5Z_\odot$	10^6	8.3	N V , C IV , He II, Si III], C III]
	κ = 40	-1	0.02	$0.5Z_\odot$	10^6	9.1	
SDSS J170110.12	M-B	-1	0.04	$3Z_\odot$	10^6	2.6	O VI +C II, N V , Si IV+O IV], C IV , He II, O III], N III], C III]
	κ = 40	-1	0.05	$3Z_\odot$	10^6	2.7	
SDSS J171908.90	M-B	-1	0.02	$Z_\odot$	10^6	0.009	N V , C IV , He II, O III] C III]
	κ = 40	-1	0.03	$Z_\odot$	10^6	0.008	
SDSS J225607.63	M-B	-1	0.05	$3Z_\odot$	10^4	0.7	O VI +C II, N V , C IV , He II
	κ = 40	-1	0.05	$3Z_\odot$	10^4	0.7	
SDSS J215341.33	M-B	-1	0.2	$2Z_\odot$	100	0.5	N V , Si IV+O IV], C IV , He II, C III]
	κ = 40	-1	0.176	$2Z_\odot$	100	0.6	
SDSS J213557.35	M-B	-1	0.036	$0.5Z_\odot$	10^6	2.4	N V , C IV , [Ne IV] λ1602, He II, C III], [Ne IV] λ2422
	κ = 40	-1	0.08	$0.5Z_\odot$	10^6	2.5	
SDSS J114703.82	M-B	-1.5	0.04	$2Z_\odot$	10^6	1.4	
	κ = 40	-1.5	0.5	$2Z_\odot$	10^4	1.6	N V , C IV , He II, C III], Mg II
SDSS J090612.64	M-B	-1.5	0.096	$2Z_\odot$	10^4	2.0	N V , C IV , He II, C III], Mg II
	κ = 40	-1.5	0.29	$3Z_\odot$	10^4	2.4	
SDSS J073637.54	M-B	-1.5	0.036	$2Z_\odot$	10^6	1.2	N V , C IV , He II, C III], Mg II
	κ = 40	-1.5	0.176	$2Z_\odot$	10^6	1.6	
SDSS J003605.26	M-B	-1.5	0.53	$2Z_\odot$	10^4	0.2	N V , C IV , C III]
	κ = 40	-1.5	1.8	$3Z_\odot$	10^4	0.1	
SDSS J153306.06	M-B	-1	0.012	$Z_\odot$	10^4	18.9	O VI +C II, N V , O I, Si IV+O IV], C IV , He II, O III], N III], Si III], C III]
	κ = 40	-1	0.015	$Z_\odot$	10^4	19.2	
SDSS J222946.61	M-B	-1	0.008	$Z_\odot$	10^6	8.2	N V , C IV , He II, Si III], C III]
	κ = 40	-1	0.0136	$Z_\odot$	10^6	9.01	
SDSS J001040.82	M-B	-1	0.0106	$0.5Z_\odot$	10^6	4.98	O VI +C II, N V , Si IV+O IV], C IV , [Ne IV] λ1602, He II, Si III], C III], [Ne IV] λ2422
	κ = 40	-1	0.0173	$0.5Z_\odot$	10^6	5.4	
SDSS J001814.72	M-B	-1	0.0196	$Z_\odot$	10^4	0.13	O VI +C II, C IV , He II, C III]
	κ = 40	-1	0.028	$Z_\odot$	10^4	0.15	

Tables 3.3 - - *Continued*

Object	EED	α	U	Z	n_H	χ^2	Emission lines used
SDSS J023519.66	M-B	-1	0.14	$3Z_\odot$	100	1.9	O VI +C II, N V , C IV
	$\kappa = 40$	-1	0.12	$3Z_\odot$	100	1.98	
SDSS J024525.95	M-B	-1	0.05	$2Z_\odot$	10^4	0.68	O VI +C II, N V , C IV , He II, O III], C III]
	$\kappa = 40$	-1	0.059	$2Z_\odot$	10^4	0.7	
SDSS J073851.85	M-B	-1	0.138	$2Z_\odot$	10^4	0.04	N V , C IV , He II, O III], C III]
	$\kappa = 40$	-1	0.075	$2Z_\odot$	10^4	0.048	
SDSS J025339.00	M-B	-1	0.096	$2Z_\odot$	10^6	0.9	O VI +C II, N V , Si IV+O IV], C IV , He II, C III]
	$\kappa = 40$	-1	0.108	$2Z_\odot$	10^6	0.9	
SDSS J082920.43	M-B	-1	0.08	$2Z_\odot$	10^6	0.2	N V , Si IV+O IV], C IV , C III]
	$\kappa = 40$	-1	0.22	$2Z_\odot$	10^6	0.3	
SDSS J095819.35	M-B	-1	0.008	$Z_\odot$	10^6	8.4	O VI +C II, N V , C IV , He II, O III], Si III], C III]
	$\kappa = 40$	-1	0.015	$Z_\odot$	10^6	8.9	
SDSS J101448.79	M-B	-1	0.2	$2Z_\odot$	10^6	0.3	N V , N IV], C IV , He II, C III]
	$\kappa = 40$	-1	0.29	$2Z_\odot$	10^6	0.4	
SDSS J112343.18	M-B	-1	0.08	$0.1Z_\odot$	10^4	1.98	N V , C IV , C III], Mg II
	$\kappa = 40$	-1	0.07	$0.1Z_\odot$	100	2.4	
SDSS J114753.29	M-B	-1	0.01	$0.1Z_\odot$	10^6	0.99	N V , C IV , C III], Mg II
	$\kappa = 40$	-1	0.06	$0.1Z_\odot$	10^6	1.5	
SDSS J125733.12	M-B	-1	0.0065	$0.1Z_\odot$	10^4	2.9	O VI +C II, N V , C IV , Mg II
	$\kappa = 40$	-1	0.012	$0.1Z_\odot$	10^4	3.05	
SDSS J124302.62	M-B	-1	0.00736	$0.5Z_\odot$	10^6	4.5	N V , SIV+OIV], C IV , He II, O III], Si III], C III], Mg II
	$\kappa = 40$	-1	0.0136	$0.5Z_\odot$	10^6	4.7	
SDSS J133059.32	M-B	-1	0.25	$3Z_\odot$	10^4	0.4	N V , C IV , He II, C III]
	$\kappa = 40$	-1	0.2	$3Z_\odot$	10^4	0.35	
SDSS J133417.04	M-B	-1	0.066	$2Z_\odot$	10^6	0.3	N V , Si IV+O IV], N IV], C IV , He II, O III], C III]
	$\kappa = 40$	-1	0.1	$2Z_\odot$	10^6	0.34	
SDSS J155108.96	M-B	-1	0.009	$0.5Z_\odot$	10^6	6.0	N V , N IV], C IV , [Ne IV] λ1602, He II, Si III], C III], [Ne IV] λ2422
	$\kappa = 40$	-1	0.017	$0.5Z_\odot$	10^6	6.5	
SDSS J155725.27	M-B	-1	0.025	$Z_\odot$	10^6	5.5	O VI +C II, N V , Si IV+O IV], C IV , [Ne IV] λ1602, He II, C III], [Ne IV] λ2422
	$\kappa = 40$	-1	0.04	$Z_\odot$	10^6	5.8	
SDSS J004600.48	M-B	-1.5	0.04	$2Z_\odot$	10^6	2.01	N V , Si IV+O IV], C IV , He II, C III], Mg II
	$\kappa = 40$	-1.5	0.096	$2Z_\odot$	10^6	2.1	
SDSS J004728.77	M-B	-1.5	0.37	$3Z_\odot$	10^4	0.002	O VI +C II, N V , C IV
	$\kappa = 40$	-1	0.12	$3Z_\odot$	10^4	0.0003	
SDSS J224532.92	M-B	-1.5	0.2	$2Z_\odot$	100	0.12	O VI +C II, N V , C IV , C III]
	$\kappa = 40$	-1.5	0.08	$2Z_\odot$	100	0.16	
SDSS J161353.27	M-B	-1.5	0.05	$2Z_\odot$	10^4	5.5	O VI +C II, C IV , He II, C III], C II]
	$\kappa = 40$	-1.5	0.156	$3Z_\odot$	10^4	6	
SDSS J125154.02	M-B	-1.5	0.156	$3Z_\odot$	100	0.26	O VI +C II, N V , C IV
	$\kappa = 40$	-1.5	0.176	$3Z_\odot$	100	0.28	
SDSS J023210.88	M-B	-1.5	0.015	$Z_\odot$	100	8.2	N V , C IV , C III], Mg II
	$\kappa = 40$	-1	0.066	$0.1Z_\odot$	10^6	11.8	

Tables 3.3 - - *Continued*

Object	EED	α	U	Z	n_H	χ^2	Emission lines used
SDSS J081950.96	M-B	-1	0.01	$0.5Z_\odot$	10^4	12.1	O VI +C II, N V , O I, Si IV+O IV], C IV , He II, C III]
	$\kappa = 5$	-1	0.01	$Z_\odot$	10^4	10.7	
SDSS J084005.00	M-B	-1	0.0058	$Z_\odot$	10^4	10.7	N V , O I, Si IV+O IV], N IV], C IV , He II, O III], Si III], C III]
	$\kappa = 5$	-1	0.0045	$3Z_\odot$	10^4	8.6	
SDSS J095118.93	M-B	-1	0.0065	$Z_\odot$	10^4	15.6	N V , O I, Si IV+O IV], C IV , [Ne IV] λ1602, He II, C III], [Ne IV] λ2422, Mg II
	$\kappa = 5$	-1	0.0065	$Z_\odot$	10^4	13.2	
SDSS J100250.98	M-B	-1	0.0136	$Z_\odot$	10^4	23.1	O VI +C II, N V , O I, C IV , He II, O III], C III]
	$\kappa = 5$	-1	0.0136	$2Z_\odot$	10^4	18.4	
SDSS J150549.73	M-B	-1	0.017	$Z_\odot$	100	17.1	O VI +C II, N V , O I, Si IV+O IV], C IV , He II, O III], N III], C III]
	$\kappa = 5$	-1	0.015	$Z_\odot$	10^4	14.03	
SDSS J100916.93	M-B	-1	0.017	$Z_\odot$	10^4	21.6	O VI +C II, N V , O I, Si IV+O IV], C IV , He II, N III], C III]
	$\kappa = 5$	-1	0.017	$Z_\odot$	10^4	19.6	
SDSS J125148.53	M-B	-1	0.008	$Z_\odot$	100	19.7	N V , O I, Si IV+O IV], C IV , He II, O III], C III], Mg II
	$\kappa = 5$	-1	0.008	$2Z_\odot$	100	13.7	
SDSS J135531.46	M-B	-1	0.009	$0.5Z_\odot$	10^4	16.6	O VI +C II, N V , O I, Si IV+O IV], C IV , [Ne IV] λ1602, He II, O III], C III], [Ne IV] λ2422
	$\kappa = 5$	-1	0.009	$Z_\odot$	10^4	13.6	
SDSS J160900.01	M-B	-1	0.009	$Z_\odot$	100	19.97	O VI +C II, N V , O I, Si IV+O IV], N IV], C IV , He II, O III], C III], Mg II
	$\kappa = 5$	-1	0.009	$Z_\odot$	10^4	15.5	
SDSS J161059.96	M-B	-1	0.0058	$Z_\odot$	100	19.2	N V , O I, Si IV+O IV], C IV , He II, O III], C III], Mg II
	$\kappa = 5$	-1	0.0065	$2Z_\odot$	100	12.7	
SDSS J162812.51	M-B	-1	0.005	$Z_\odot$	10^4	11.1	N V , O I, Si IV+O IV], N IV], C IV , He II, O III], N III], C III], Mg II
	$\kappa = 5$	-1	0.0045	$3Z_\odot$	10^4	8.4	
SDSS J013747.84	M-B	-1	0.004	$0.1Z_\odot$	100	5.7	O VI +C II, N V , O I, C IV ,
	$\kappa = 5$	-1	0.003	$3Z_\odot$	100	2.9	
SDSS J014607.15	M-B	-1	0.0106	$Z_\odot$	10^4	46.1	O VI +C II, N V , O I, N IV], C IV , He II, C III]
	$\kappa = 5$	-1	0.0106	$2Z_\odot$	10^4	37.99	
SDSS J015700.14	M-B	-1	0.156	$3Z_\odot$	10^6	0.7	O VI +C II, N V , C IV , He II, C III]
	$\kappa = 5$	-1	0.156	$3Z_\odot$	10^6	0.7	
SDSS J020245.82	M-B	-1	0.23	$3Z_\odot$	10^4	0.003	C IV , He II, C III]
	$\kappa = 5$	-1	0.37	$2Z_\odot$	10^6	0.002	
SDSS J020643.64	M-B	-1	0.0058	$Z_\odot$	10^4	23.2	O VI +C II, N V , O I, C IV , He II, O III], Si III], C III]
	$\kappa = 5$	-1	0.0045	$3Z_\odot$	10^4	14.8	
SDSS J081452.04	M-B	-1	0.009	$0.1Z_\odot$	100	21.2	O VI +C II, N V , O I, C IV , C III]
	$\kappa = 5$	-1	0.009	$0.1Z_\odot$	100	15.6	

The QSO2s are generally better fitted by κ-distribution models (87 in 126 objects, see Figure 3.6). Of these, 65 (52%) sources are best fitted by a κ model with $\kappa = 5$. In contrast, only 38 of the QSO2s (31%) are better-fitted by a M-B model.

Figure 3.8 presents the QSO2s binned according to discrepancy in α (panel (a)), n_H

(panel (b)), Z (panel (c)) and U (panel (d)).

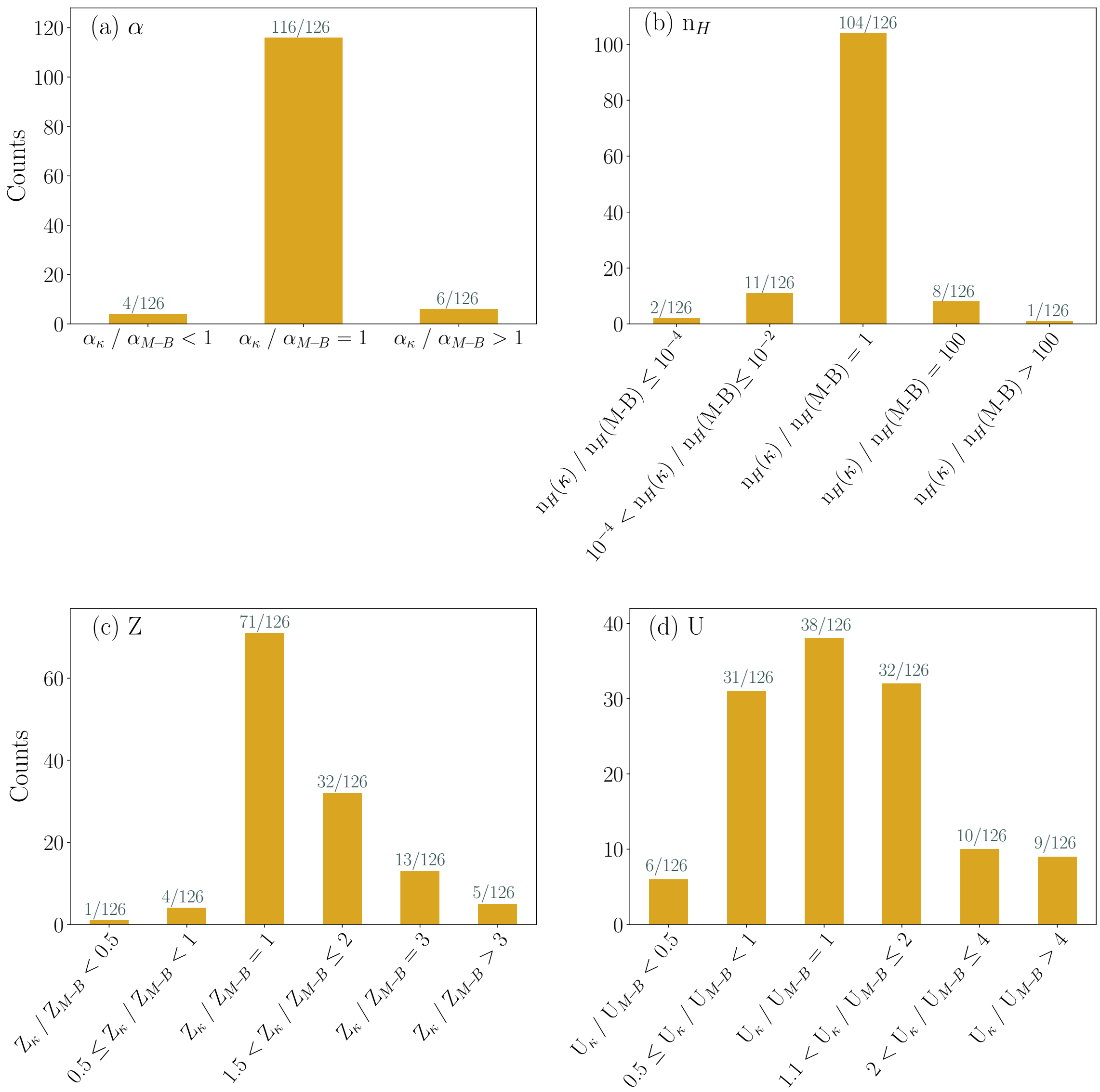

Figure 3.8: QSO2s binned according to discrepancy in (a) α, (b) n_H, (c) Z, and (d) U between κ and M-B distributions.

Similarly to the HzRGs and the Seyfert galaxies, a spectral index of -1 generally gives the best fit to the emission line ratios. The assumption of a κ or M-B distribution has no apparent impact on the inferred spectral index, α, in most of the QSO2s (116/126 or 92%).

Panel (b) of Figure 3.8 presents the ratio $n_H(\kappa)$ / n_H(M-B). Assuming a κ distribution instead of the M-B does not cause significant changes to the derived n_H. For 104 (83%) of the QSO2s the value of n_H is identical in the best-fitting κ and M-B models. Of these 104 objects, 24 are best-fitted by a model with n_H = 100 cm^{-3}, 55 by a model with n_H = 10^4 cm^{-3} and the remaining 25 are best-fitted by a model with n_H = 10^6 cm^{-3}. For the remaining 17% of QSO2s, we find discrepancies in the best n_H values as high as two orders of magnitude.

In panel (c) of Figure 3.8 the ratio Z_κ / $Z_{\text{M-B}}$ is presented. The best-fitting κ models have similar or higher values of Z than the best-fitting M-B models in 96% (121/126) of cases. The best-fit metallicities are consistent (Z_κ / $Z_{\text{M-B}}$ = 1) in 56% of the QSO2s. For 25% of objects, the best-fitting κ distribution model has a metallicity value that is a factor of 1.5 to 2 higher than that in the M-B model. A large discrepancy (Z_κ / $Z_{\text{M-B}} < 0.5$ or Z_κ / $Z_{\text{M-B}} \geq 3$) in the best-fit metallicity occurs for 19 QSO2s (15%).

Panel (d) of Figure 3.8 presents the results for the ionization parameter. The values of U from the best-fitting κ and M-B models differ in 70% (88/26) of QSO2s. The values from the κ models are a factor of 1.1 to 2 times higher than $U_{\text{M-B}}$ in 25% (32/126) of cases. For 37 QSO2s (29%) κ models have a lower ionization parameter than the M-B models. In 25% of these cases, κ models have an ionization parameter that is a factor of 1.1 to 2 times lower than the value in the M-B model. Large discrepancies (U_κ / $U_{\text{M-B}} < 0.5$ or U_κ / $U_{\text{M-B}} > 2$) in the ionization parameter occur for 25 QSO2s (20%).

3.4 Discussion

The physical properties of gaseous nebulae are usually inferred under the assumption that the electrons are in an equilibrium M-B distribution. This is assumed because the energy redistribution through elastic collisions of electrons occurs faster than any other process (e.g., Draine and Kreisch, 2018). However, if the injection of energetic electrons into the gas is continuous and swift enough that the particle distribution does not have time to relax into the classical equilibrium distribution, then κ distributions may arise.

Several mechanisms that may be capable of creating and maintaining κ distributions in photoionized regions have been proposed. These include the injection of a population of supra-thermal electrons by acceleration mechanisms such as magnetic reconnection and development of inertial Alfvén waves, shocks or the injection of high-energy electrons through the photoionization process. Energetic electrons can be produced by the photoionization of dust (Dopita and Sutherland, 2000; van Hoof et al., 2004), and X-ray or EUV photoionization (Shull and van Steenberg, 1985; Petrini and da Silva, 1997; Langer and Pineda, 2015). Active galaxies are objects where shocks, winds and turbulence are known to be present (e.g., Baring, 1991; Humphrey et al., 2008a; Humphrey et al., 2010; Zhang et al., 2013; Silva et al., 2018), and these processes may also be sufficient to accelerate particles creating κ-distributed electron energies. Several other processes, which are plausibly associated with AGN activity, may also be responsible for deviations from equilibrium, such as ionization by cosmic rays (Giammanco and Beckman, 2005; Ferland et al., 2009) or dissipative turbulence internal to the gas clouds (Mignoli et al., 2019).

Thus, several processes may induce κ electron energy distributions in the NLR and our results show that they give a better fit to the overall sample. However, they are not capable of reproducing some line ratios (such as C III] λ1909 / C II] λ2326 or [O III] λ4363 / [O III] λ5007, see Figures 3.4 and 3.5, respectively), which suggests that some additional physics is missing from the models. In our models we neglect shocks and consider only AGN photoionization, but in some sources, shocks may also contribute to the ionization of the NLR gas clouds, as is seen in other AGN (e.g., Wilson and Raymond, 1999; Tadhunter, 2002; Moy and Rocca-Volmerange, 2002; Hashimoto et al., 2011; D'Agostino et al., 2019).

We also note that the application of photoionization models is based on a number of simplifications and assumptions that can affect the resulting spectra. As an approximation, we use a single-slab model that assumes that the ionic species share the same physical conditions. However, for high-z galaxies we use the integrated spectra to derive the physical parameters of the gas and these spectra are, in many cases, spatially integrated over large regions (> 10 kpc) and the physical conditions and sources of excitation may change within these regions. It is also expected that the central regions of the galaxies have higher densities and ionization parameters than the outer regions of the NLR (e.g., Bennert et al., 2006b; Bennert et al., 2006a) so the integrated spectra can potentially be contaminated by regions with different physical conditions, such as high density nuclear regions.

As input parameters, AGN photoionization models require several parameters, such as the spectral index of the ionizing continuum, the hydrogen density, and the initial chemical abundances. However, these parameters are not well constrained by observations. There is also some debate about the inclusion of dust in the models. Our models do not include dust because although dust has been found in the vicinity of AGN (e.g., Laor and Draine, 1993; Radomski et al., 2003), Nagao et al. (2003), Nagao et al. (2006), and Matsuoka et al. (2009) found that dust-free AGN models provide more accurate predictions compared to dusty models. On the other hand, Dopita et al. (2002), Groves et al. (2004), and Revalski et al. (2021) found that dusty models provide more accurate predictions of the observations in NLRs. All of this may explain why our simple photoionization models cannot reproduce all the line ratios in the selected galaxy sample.

In summary, there are many mechanisms taking place in AGN that can give rise to κ distributions, and they should be taken into account when studying the NLR because, as we have seen, models using κ-EEDs give better fits to the line ratios of many sources than models using the equilibrium M-B distribution. However, we should also try to get better constraints of the input parameters to minimize the sources of uncertainty in the photoionization models.

3.5 Conclusions

In this work we have studied the effect of κ-distributed electron energies on the emission line ratios of photoionized nebulae associated with AGN. We also provide best fitting parameters (Z, n_{H}, α and U) for κ and M-B photoionization models for 143 type 2 AGN: 15 HzRGs, 126 QSO2s and two Seyfert galaxies.

We find that the EED used as input in the photoionization models has a strong influence on the output spectra. The impact is particularly strong in some UV and optical emission lines. We also find that the impact of adopting κ distributions is strongly dependent on gas metallicity and ionization parameter. We can summarize our results as follows:

- The fluxes of rest-frame UV lines with high excitation energies (e.g., C IIIλ977, N V λ1240) are greatly enhanced by κ distributions. The enhancement is stronger for lower values of κ, i.e. for stronger deviations from thermal equilibrium.

- In the rest-frame optical, some line fluxes are enhanced when κ distributions are adopted (e.g., [O III] λ4363), but in most cases the line fluxes are fainter in the κ models compared to the M-B models (κ / M-B < 1).

- Using κ distributions results, generally, in a decrease of the predicted rest-frame IR line fluxes. With increasing metallicity and ionization parameter the differences between ratios obtained using M-B distributions and κ distributions decreases.

- We have compared our models against the rest-frame UV to optical emission line ratios of 143 type 2 AGN and found that for a subset of the sources (one of the two studied Seyfert galaxies, 67% of HzRGs and 69% of QSO2s), a photoionization model using κ-EED provides a significantly better fit to the data, which suggests that κ-distributed electron energy distributions may indeed be present in the NLR of some type 2 AGN.

- In most cases (93% of HzRGs and 92% QSO2s), the best-fit spectral index derived from the models does not depend on the adopted EED.

- The assumption of κ-distributed energies instead of the M-B distribution has no impact on the derived gas density in most HzRGs (11/15 or 73%) and QSO2s (104/126 or 83%). Deviations in n_H by a factor as large as $\geq$ 100 are identified in the remaining 17% of QSO2s.

- Regarding the metallicity, the general trend in both HzRGs and QSO2s is that κ models lead to identical (roughly in half of both samples) or higher Z estimates compared to when M-B models are used. More specifically, the predicted metallicities are consistent ($Z_\kappa = Z_{\text{M-B}}$) in 53% of HzRGs (8/15) and 56% of QSO2s (71/126). For the rest of the sample, but for a few exceptions, the best-fitting κ-model has a metallicity that is 1.5 to 2 times higher than in the best-fitting M-B model in 40% HzRGs (6/15) and 25% (32/126) QSO2s. Large discrepancies (a factor > 2) between the metallicity values of the κ and M-B models are found in a small fraction of HzRGs (1/15) and QSO2s (19/126).

- The best-fit ionization parameter for the κ and M-B models differ significantly in most objects (13/15 or 87% of HzRG and 88/126 or 70% of QSO2). HzRGs and QSO2s behave differently in the sense that in general the best-fitting κ models have higher U values ($1.1 < U_\kappa / U_{\text{M-B}} < 2$), while the relative factor $U_\kappa / U_{\text{M-B}}$ is more evenly spread in QSO2s at both sides of $U_\kappa / U_{\text{M-B}} = 1$. Large discrepancies occur for 25 QSO2s (20%, all of which have $U_\kappa / U_{\text{M-B}} > 2$) and one HzRG (with $U_\kappa / U_{\text{M-B}} < 0.5$).

In this work we have found tantalizing evidence for the presence of κ-distributions in the NLR of some AGN, based on the fact that their emission line ratios are better reproduced by photoionization models that use κ-distributed EEDs. However, there is still some controversy surrounding κ distributions and their presence or "survival" in extra-solar photoionized nebulae. Thus, more work is needed to identify and understand physical processes that could establish κ-distributed EEDs in the NLR.

Chapter 4

Gas kinematics and jet-gas interactions in a radio galaxy at z = 3.57

Powerful HzRGs[1] ($z > 2$) represent an interesting phase in the life of what are believed to be the progenitors of massive elliptical galaxies (e.g., Miley and De Breuck, 2008; Collet et al., 2015; Castignani et al., 2019).

HzRGs are bright radio emitters ($L_{500\,\mathrm{MHz}} > 10^{27.5}$ W Hz^{-1}; e.g., De Breuck et al., 2002; Miley and De Breuck, 2008), which has for several decades allowed observers to trace them to high redshifts (up to $z \sim 5.72$; e.g., Saxena et al., 2018). These distant active star-forming galaxies (up to 10^3 $M_\odot$ yr^{-1}; e.g., Reuland et al., 2004; Humphrey et al., 2011; Seymour et al., 2012; Drouart et al., 2014; Falkendal et al., 2019) are amongst the most massive galaxies ($M_* \gtrsim 10^{11-12}$ $M_\odot$; e.g., De Breuck et al., 2002; Rocca-Volmerange et al., 2004; Seymour et al., 2007; De Breuck et al., 2010; Drouart et al., 2016) in the universe, as shown by the Hubble K-z relation (where K is the near-infrared 2.2 μm apparent magnitude; e.g., De Breuck et al., 2002; Rocca-Volmerange et al., 2004; Seymour et al., 2007; De Breuck et al., 2010; Drouart et al., 2016). As such, they are believed to be the progenitors of massive giant elliptical galaxies found in the local Universe (e.g., McLure et al., 2004;

[1]Here, the term HzRGs refers only to high-z narrow-line radio galaxies. We are excluding broad line radio galaxies.

Overzier et al., 2008; De Breuck et al., 2010; Galametz et al., 2012; Wylezalek et al., 2013; Uchiyama et al., 2022). They are also expected to host the most massive black holes at their cores.

Because the central engine (the accretion disk and BLR) is hidden from the line of sight by the obscuring torus, it is possible to study the properties and components of the host without the overwhelming glare of the quasar. In addition, since both radiative (quasar-mode) and mechanical (radio-mode) feedback are likely to be in action, HzRGs are ideal targets to study the co-evolution of massive galaxies and their central SMBHs in the early Universe as well as the role that feedback mechanisms may play in it.

Often located in overdense environments (e.g., Wylezalek et al., 2013; Hatch et al., 2014), HzRGs have been used to pinpoint the location of galaxy protoclusters (e.g., Pentericci et al., 2000; Venemans et al., 2007; Galametz et al., 2010; Hayashi et al., 2012; Cooke et al., 2014). Thus, they are also very interesting systems to investigate how the most massive gravitationally bound structures in the Universe formed (e.g., Venemans et al., 2007; Wylezalek et al., 2013; Husband et al., 2016; Overzier, 2016).

These sources usually show an alignment between the main axis of the radio source and the optical continuum and line emission (e.g., Chambers et al., 1987; McCarthy et al., 1987a; Pentericci et al., 2001), which was one of the first evidences that the AGN interacts with the gas associated with the host galaxy. HzRGs are commonly surrounded by Lyα nebulae that often reach more than 100 kpc in size and sometimes surpass the extension of the radio sources (e.g., Reuland et al., 2003; Villar-Martín et al., 2003).

As mentioned, they tend to be aligned with the radio axis (e.g., Reuland et al., 2003; Villar-Martín et al., 2006). These halos show chemical enrichment ($Z \gtrsim Z_{\odot}$; e.g., Vernet et al., 2001; Humphrey et al., 2008a; Swinbank et al., 2015; Nesvadba et al., 2017b), perturbed kinematics inside the radio structures (FWHM $\gtrsim$ 1000 km s^{-1}; e.g., Reuland et al., 2007; Villar-Martín et al., 2007b) and quiescent motions in the outer parts, beyond the radio source edges (FWHM < 1000 km s^{-1}; e.g., van Ojik et al., 1997; Villar-Martín et al., 2003). All this further highlights the important role played by the interactions between the radio source and the ambient gas and shows the importance of investigating how the mechanical feedback is triggered in the process. As mentioned in Section 1.5, these nebulae are of extreme importance because they trace the conditions of the gas associated with the most massive galaxies in an early cosmic epoch, across different spatial scales, both in the ISM and well into the CGM surrounding the host galaxy.

This chapter presents a detailed study of the Lyα halo that surrounds the radio galaxy 4C+03.24 found at z = 3.57. At this redshift 1″ corresponds to 7.399 kpc. This radio galaxy has been previously studied, so we will start by briefly mentioning the key results from previous works.

4.1 The 4C+03.24 radio galaxy

The radio galaxy 4C+03.24 (also known as USS 1243+036) was first identified in a survey of ultra steep-spectrum radio sources (Röttgering et al., 1994; van Ojik et al., 1997). Follow-up observations were made by van Ojik et al. (1996) who found that the radio source has an integrated power of $P_{4.7\,GHz} \sim 1.1 \times 10^{28}$ W Hz^{-1}, extends over 55 kpc and shows a double radio-source with a sharply bent radio structure on the southern side (see left panel of Figure 4.1).

This galaxy has a low amount of dust ($M_{dust} < 7.7 \times 10^{7}$ M$_{\odot}$; Cimatti et al., 1998) and molecular gas ($M(H_2) = 0.65 \pm 0.22 \times 10^{10}$ M$_{\odot}$; Kolwa et al., 2023) when compared to other HzRGs. It has a star formation rate of $\sim$ 142 M$_{\odot}$ yr^{-1} (Falkendal et al., 2019), and a stellar mass of $\log(M_{*}/M_{\odot}) < 11.27$ (De Breuck et al., 2010).

The radio galaxy is surrounded by a giant Lyα halo that extends over 135 kpc (van Ojik et al., 1996). Both the Lyα emission and the UV continuum are aligned with the main axis of the radio emission and follow closely the bend in the southern radio source (UV emission is shown in the right panel of Figure 4.1; van Ojik et al., 1996; Pentericci et al., 1999). In addition to the extended Lyα emission, this object also shows extended X-ray and rest-frame optical emission line ($\sim$ 60 kpc and 38 kpc, respectively; Smail et al., 2012; Wu et al., 2017; Nesvadba et al., 2017b) that is also aligned with the radio axis.

The giant Lyα nebula is known to show complex morphology and kinematics, both clearly correlated with the radio structures. The emission line has higher surface brightness and is broader (FWHM $\sim$ 1500 km s^{-1}) within the radio structures than beyond (FWHM $\sim$ 250 km s^{-1}). The giant halo has a velocity shear of Δv $\sim$ 450 km s^{-1} (e.g., van Ojik et al., 1996; Ohyama and Taniguchi, 2004).

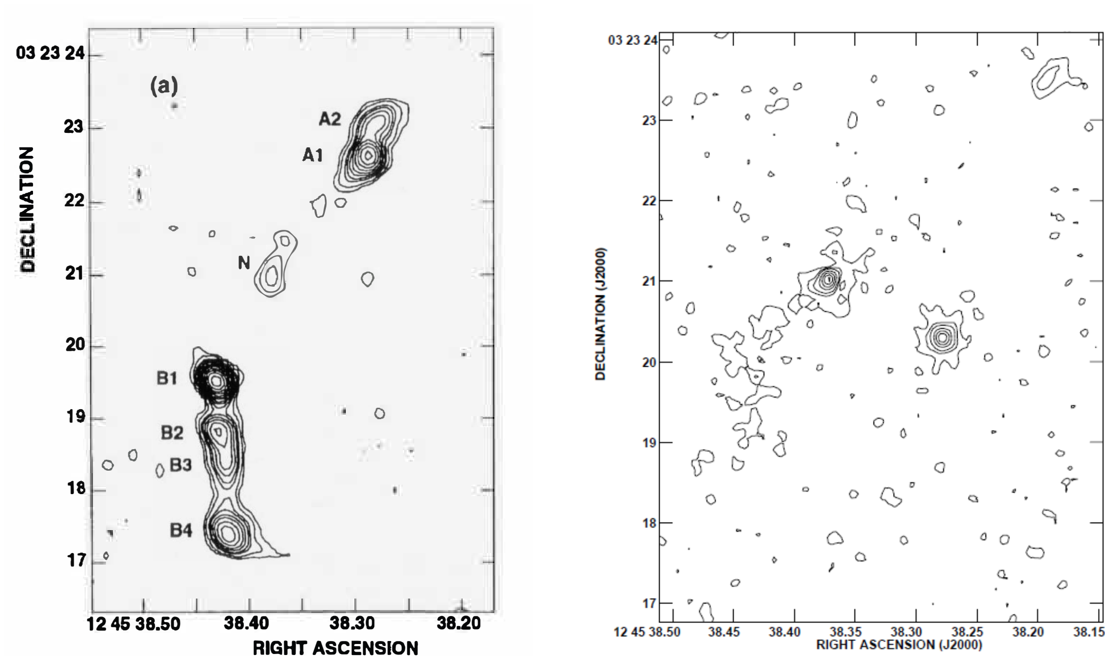

Figure 4.1: Left: 8.3 GHz VLA contours of 4C+03.24 taken from van Ojik et al. (1996); Right: Optical HST contour representation of the rest-frame UV continuum emission observed with the filter F702W with a rest-frame spectral coverage between 1352 Å and 1654 Å. Taken from Pentericci et al. (1999).

Because they will be of great importance in our study, we list in Table 4.1 the different radio components identified by van Ojik et al. (1996) (seen in the left panel of Figure 4.1).

Table 4.1: Radio components of 4C+03.24 identified by van Ojik et al. (1996). "N" corresponds to the "radio core". The other components form the extended radio emission.

Component	R. A. (J2000)	Declination (J2000)
A2	$12^{h}\,45^{m}38.28^{s}$	03º 23′ 23.1″
A1	$12^{h}\,45^{m}38.29^{s}$	03º 23′ 22.6″
N	$12^{h}\,45^{m}38.37^{s}$	03º 23′ 21.0″
B1	$12^{h}\,45^{m}38.43^{s}$	03º 23′ 19.5″
B2	$12^{h}\,45^{m}38.43^{s}$	03º 23′ 18.8″
B3	$12^{h}\,45^{m}38.42^{s}$	03º 23′ 18.4″
B4	$12^{h}\,45^{m}38.42^{s}$	03º 23′ 17.4″

4.2 Observations and data reduction

The radio galaxy 4C+03.24 was observed in the night of 2018 June 17^{th} using the Multi Unit Spectroscopic Explorer (MUSE; Bacon et al., 2010). The data were released from the MUSE WFM-AO comissioning observations at the Very Large Telescope (VLT) under Programme ID 60.A-9100(G). MUSE is an integral field spectrograph, mounted on the UT4 of the VLT at the Paranal Observatory in Chile. The Wide Field Mode with adaptive optics (AO) was used, which provides a $1' \times 1'$ field of view and a sampling of 0.2″ pixel^{-1}. MUSE covers the wavelength range between 4750 Å and 9300 Å, with a gap between ~5800 Å and 5950 Å, because the AO works with sodium lasers that would saturate the detector in that wavelength range. The spectral resolution is $R = \lambda/\Delta\lambda = 1750$ at 4650 Å and 3750 at 9300 Å. The total exposure time on source was 1.25 hr (3 × 1500 s). The airmass during the observations was $\sim 1.25 \pm 0.10$. and the seeing FWHM was in the range 0.61″ - 0.70″.

To reduce the archival MUSE data, the standard ESO MUSE pipeline recipes v2.8.5 (Weilbacher et al., 2020) and the command-line tool ESOREX were used. Each of the individual exposures was bias-subtracted, flat-fielded, twilight and illumination corrected, sky-subtracted and wavelength calibrated using the calibration data taken closest in time to the science frames. The flux calibration of each exposure was done using a spectrophotometric standard star observed during the same night of the science observation. The individual exposures were then combined into a single data cube. Finally, the software ZAP[1] (Soto et al., 2016) was used to suppress sky line residuals that were left from the sky subtraction. The final cube has a spatial pixel scale of 0.2″ and spectral resolution of ~2.5 Å FWHM, at a sampling of 1.25 Å per spectral pixel.

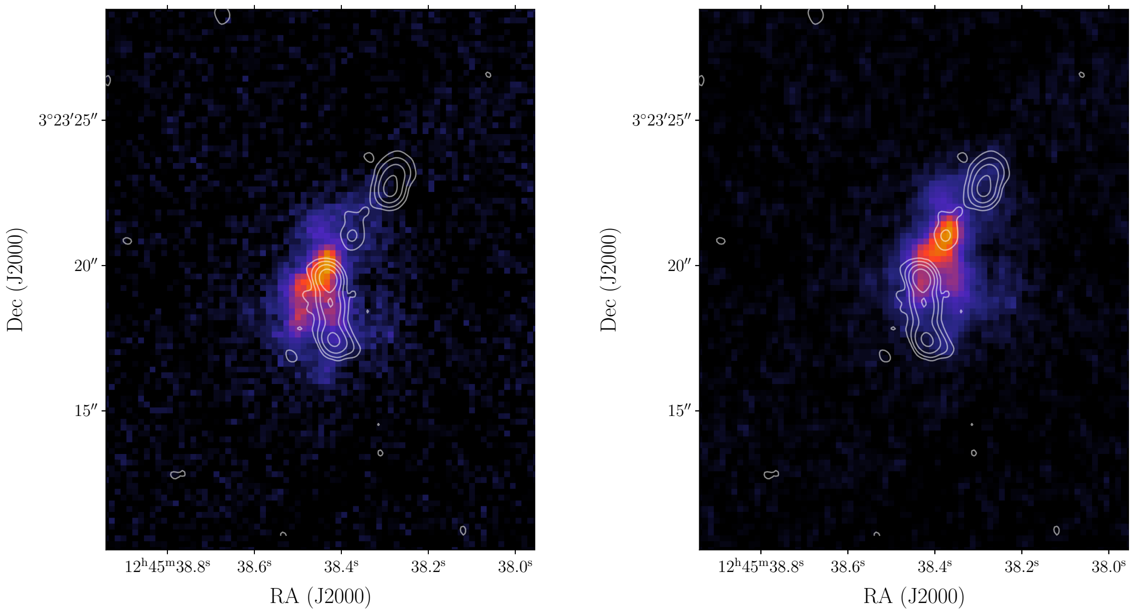

(a) Before correction

(b) After correction

Figure 4.2: Overlay between the 8.3 GHz VLA radio contours and the continuum subtracted Lyα image before (left) and after (right) applying the astrometric correction to the MUSE data. The Lyα+continuum image was created by collapsing the data cube in the wavelength dimension in the spectral range 5540 - 5570 Å.

The world coordinate system in the final data cube has a small shift from the true coordinates of the object. By measuring the coordinates of several stars in our cube and

[1]Zurich Atmosphere Purge; https://zap.readthedocs.io/en/latest/

comparing them with the coordinates for those sources in SDSS and GAIA we found a difference of $\sim 1.04''$ in declination, and $\sim 0.9''$ in right ascension between the coordinates in the cube and the coordinates in SDSS and GAIA. This difference was corrected using the *resample* function available in the Python package MPDAF. Figure 4.2 shows the Lyα image before and after the correction (panels (a) and (b), respectively). To highlight the differences we overlay the radio contours of this galaxy.

4.3 Analysis

The study of the giant nebula associated with 4C+03.24 will be focused on Lyα. As mentioned in section 1.5.1, this is not always a reliable tracer of gas kinematics and distribution due to its resonant nature (Neufeld, 1990), but it is the only emission line detected in the MUSE data with sufficient signal to noise to perform detailed kinematic analysis across the nebulosity.

For reassurance, we note that we will be able to compare with the kinematic study made by Nesvadba et al. (2017b) based on near infrared integral field spectroscopy of rest frame optical emission lines, particularly [O III] $\lambda\lambda$4959,5007. Although the authors cannot trace the entire nebula, the comparison will be of great use. It will allow us to argue that, unless stated otherwise, while resonant scattering may play some role in shaping the Lyα profiles, the main variations described and discussed in the next sections are a consequence of intrinsic motions.

4.3.1 Systemic redshift

We start by defining the systemic redshift[2] (z_{sys}) of 4C+03.24. This step is needed in order to be able to understand changes in line velocities, particularly whether gas is infalling or outflowing.

[2]Systemic redshift is defined as a fiducial value for the redshift representing the mean redshift of the stars in the host galaxy. When stellar features are not detected, as is often the case in high-z systems, emission lines from the gas are used.

Ideally, we would use He II λ1640 (hereinafter He II) because it is a non resonant recombination line that is usually present in the rest frame UV spectra of HzRGs. However, He II is not detected in the nuclear regions of this object (see Figure 4.3). In order to maximize the S/N for the He II and C IV lines, we extracted spectra from apertures of different radial sizes centered at the spatial location of the optical continuum centroid. He II was not detected in any of them, so we derive the redshift using the wavelength of the C IV doublet.

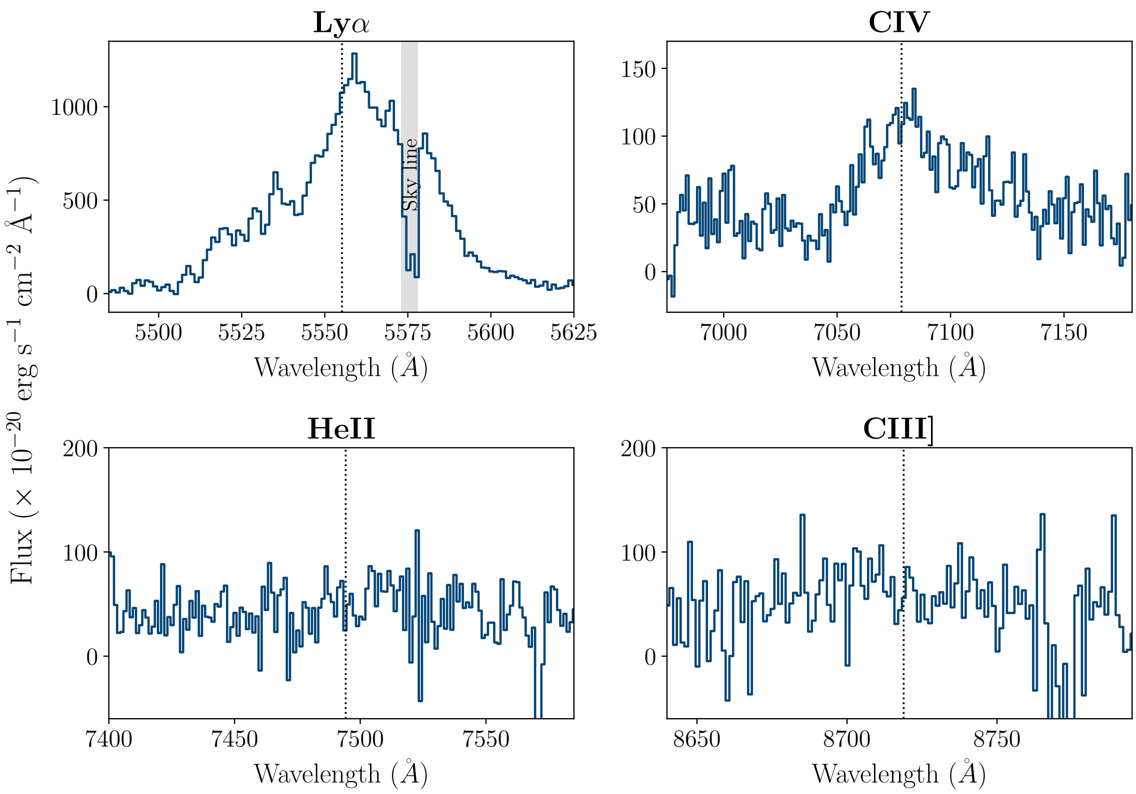

Figure 4.3: Spectral regions around the Lyα (top left panel), C IV (top right panel), He II (bottom left panel) and C III] (bottom right panel) emission lines, or their expected wavelengths when they are not detected. The 1D spectrum was extracted from the central nuclear aperture (coincident with the radio core; see Section 4.3.2). The vertical dotted line marks the expected line wavelength for the systemic redshift inferred from C IV . The grey region in the first panel marks the location of the [O I] λ5577 Å sky line that affects Lyα.

Consequently, we expect that the uncertainty in the systemic redshift estimate is potentially larger than it would have been had He II been available for use. On one hand, C IV is also sensitive to resonant scattering effects that can distort the spectral profile (e.g., Jarvis et al., 2003; Humphrey et al., 2008b; Wang et al., 2021b). On the other hand, C IV is a doublet (1548 and 1550 Å, or 9.2 Å separation at z = 3.57) and this broadens the line profile. Because the individual components are intrinsically very broad, they are severely blended.

We derive a systemic redshift of 3.569 ± 0.005 which is consistent with the systemic redshift obtained by Nesvadba et al. (2017b) using the [O III] λ5007 emission line (3.56573 ± 0.00005).

4.3.2 Aperture selection

The variation of the Lyα spatial profiles across the nebula was investigated. For this, we extracted one dimensional spectra from numerous apertures across the nebula (Figure 4.4). The selection was based on the visual inspection of the Lyα profiles at every spaxel. To disfavour aggregating spatial regions with substantially different kinematics within a given aperture, each was defined to cover spatially adjacent spaxels with similar line profiles.

An alternative would have been to apply a Voronoi binning algorithm (Cappellari and Copin, 2003), which is useful to select regions with similar S/N ratios and in our case could be interesting to obtain higher S/N ratios in the outer regions of the halo. However, this method does not take into account the shape of the emission line, potentially summing spaxels with dissimilar velocity profiles. Therefore, Voronoi binning was not applied in this work.

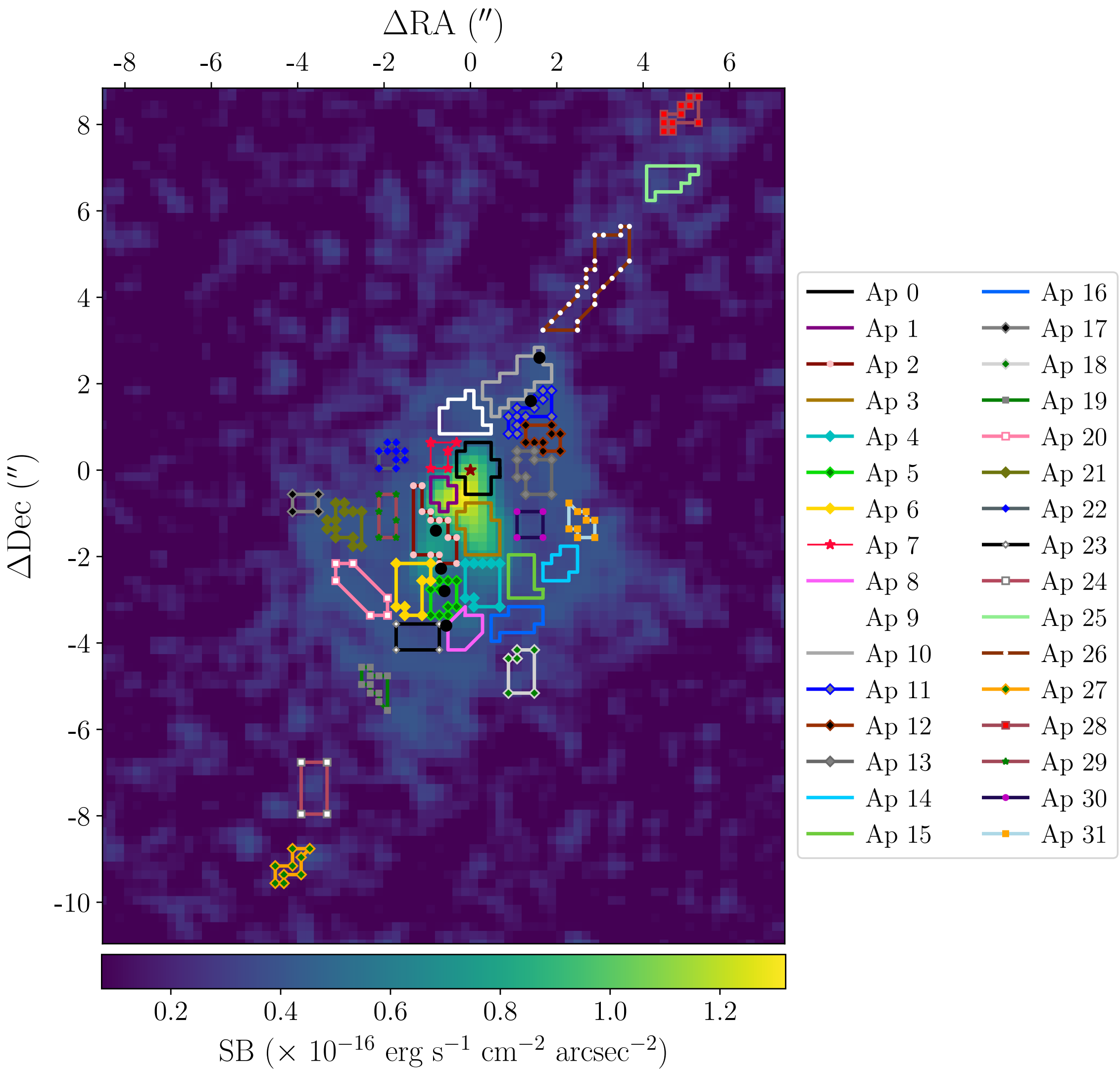

Figure 4.4: Selected apertures overlaid on the Lyα image. The black dots and the red star are the radio components presented in Table 4.1. Relative coordinates from the nucleus of the radio galaxy are shown in both right ascension and declination.

4.3.3 Non-parametric Measurements

As we will see, the Lyα profile is complex and non-Gaussian in several apertures. In such cases, performing Gaussian fitting will fail to adequately quantify its properties and infer the relative impact of resonant scattering vs. kinematics (see above). For this reason we adopt a non-parametric approach to characterize the Lyα profiles. This can be carried out by measuring velocities at which some fraction of the line flux is accumulated (Whittle, 1985). Since these measurements are performed directly on the observed profile they are independent from the assumed line profile and from assumed fitting functions (Veilleux, 1991).

We start by measuring the cumulative flux of the emission line as a function of wavelength (or velocity) without using any fitting function. Then we measure the velocity width, asymmetry and median velocity as described below. An illustration of the non-parametric measurements used in this work is shown in Figure 4.5.

- **Velocity width W_{80}**

  The index W_{80} is the width that encloses 80% of the total flux of the line. It is defined as the difference between the velocities at 90% (v_{90}) and 10% (v_{10}) of cumulative flux:

  $$W_{80} = v_{90} - v_{10} \tag{4.1}$$

  For a Gaussian profile, the velocity width is close to the FWHM, $W_{80} = 1.088\times$ FWHM, but for a non-Gaussian profile this index is more sensitive to the broad bases of the emission lines.

  Line broadening due to instrumental effects is negligible, except in the outer, most distant apertures where the Lyα line is narrower. The line profile in some of these apertures is consistent with a Gaussian. In others, the line appears somewhat asymmetric, but the S/N is too low to confirm whether this is a real effect or a consequence of the noise. In those cases, a Gaussian profile is the best possible method to characterize the kinematic parameters (the uncertainties are reflected in the large errors of these measurements). Instrumental broadening in such cases was corrected for by subtracting the instrumental profile in quadrature.

- **Asymmetry**

  The asymmetry parameter was introduced by Whittle (1985). This measure is a non-parametric analog of skewness. To measure the asymmetry of the velocity profile relative to the median velocity, we compute a dimensionless relative asymmetry given by

$$A = \frac{(v_{90} - v_{50}) - (v_{50} - v_{10})}{W_{80}} \tag{4.2}$$

where v_{10} and v_{90} are the velocities previously defined, and v_{50} is the median velocity where the flux is 50% of total. We adopt the definition used by Liu et al. (2013), where negative values of A indicate there is relatively more flux on the blue side of the line, and positive values indicate there is relatively more flux on the red side of the line.

- **Median velocity** v_{50}

  The parameter v_{50} is the median velocity of the emission line profile defined in equation 4.2. It is calculated with respect to the systemic velocity, as inferred from the C IV line at the location of the optical (UV rest frame) continuum centroid (see Section 4.3.1). This value traces the bulk gas velocity.

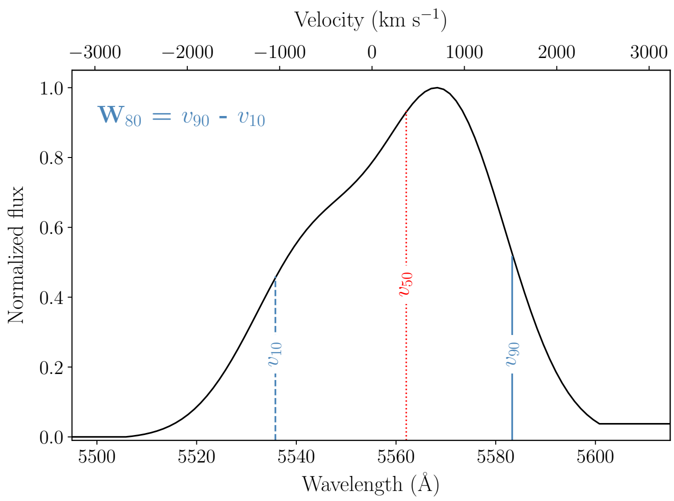

Figure 4.5: A visualization of the non-parametric measurements used in this work. In black we have an arbitrary emission line. The vertical blue lines mark the location of v_{10} and v_{90}, the velocities at which the cumulative flux is 10% and 90%, respectively. The vertical red line marks the location of v_{50}, or the velocity where the cumulative flux is 50% of the total. W_{80} is defined as the difference between v_{90} and v_{10}.

We perform the non-parametric measurements directly on the observed Lyα velocity profiles (see Figure 4.5). W_{80} and the asymmetry are measurements of differences in velocity from one part of the line profile to the other and thus are not dependent on the accurate determination of the host galaxy's redshift.

4.4 Results

The Lyα nebula surrounding 4C+03.24 shows an asymmetric and complex morphology. The Lyα emission is widespread and not confined to the expected volume of the ionization cones; it extends for $\sim$ 148 kpc ($\sim$ 20″) in the direction of the radio axis and for about 6.8″, or 50 kpc perpendicularly to it (see Figure 4.6).

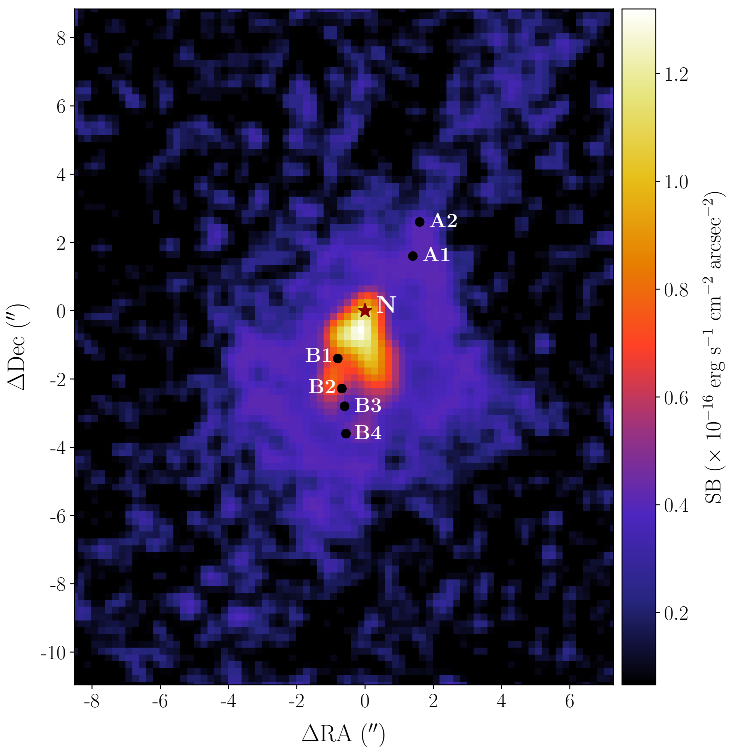

Figure 4.6: Lyα image smoothed with a 0.85 pixel kernel. The red star shows the position of the nucleus (N) and the black dots show the positions of the radio hotspots presented in Table 4.1.

We find that the Lyα nebula has a luminosity of $4.8 \pm 0.6 \times 10^{44}$ erg s^{-1}, consistent with other results found in the literature (e.g., van Ojik et al., 1996; Smail et al., 2012; Wang et al., 2023b). In the central aperture (Aperture 0) we obtain a luminosity of $6.5 \pm 0.7 \times 10^{43}$ erg s^{-1}.

Regions with different kinematic properties are found within the nebula (see also van Ojik et al., 1996). The gas in the low surface brightness halo located beyond the radio structures shows quiescent kinematics ($W_{80} \lesssim 700$ km $^{-1}$) when compared to the gas within and coincident with the radio features ($W_{80} \gtrsim 1500$ km $^{-1}$). Along the Lyα filament (see Section 4.4.1) we detect gas as quiescent as $W_{80} \lesssim 300$ km $^{-1}$.

4.4.1 Lyα morphology

We began our morphological study by creating a Lyα mosaic, showing the Lyα nebula at different velocities. To create the mosaic, sections with a spectral width of 10 Å (or 540 km s^{-1}) of the Lyα emission were collapsed and each section is shown in a panel of Figure 4.7.

To calculate the 3σ surface brightness (SB) limit we selected 10 line-free apertures, each with 5×5 pix^2 or 1 arcsec^2. We then calculate the RMS of the background. The 3σ detection limits in Figure 4.7 vary from 2.2×10^{-18} to 4.6×10^{-18} erg s^{-1} cm^{-2} arcsec^2.

The morphology of the Lyα nebula shows interesting variations with velocity. Gas moving close to the systemic velocity (panel (d)), and gas with a redshifted velocity (panels (e) and (f)) shows a broad spatial distribution, and is present both within the radio structures and beyond them. At more redshifted velocities the gas appears more widespread. Gas is detected not only along and within the radio structures as before, but also beyond these, up to ~ 68 kpc from the continuum centroid, and in the direction perpendicular to it, up to ~ 29 kpc from the radio core.

There is substantial evidence for strong interaction between the radio source and the ambient gas. The morphology of the most blueshifted gas (panels (a) and (b)) is strongly correlated with the radio source (this gas is constrained within the extension of the radio source), both in size and in its highly collimated morphology. Further evidence lies in the enhancement of the Lyα emission at the location of the south-eastern B1 (see Figure 4.1) radio hotspot, where it bends following the radio morphology very tightly, at an angle of $\sim 30°$ (panels (b) and (c) in Figure 4.7; see also van Ojik et al., 1996). This suggests that the radio/gas interaction is strongest at this location.

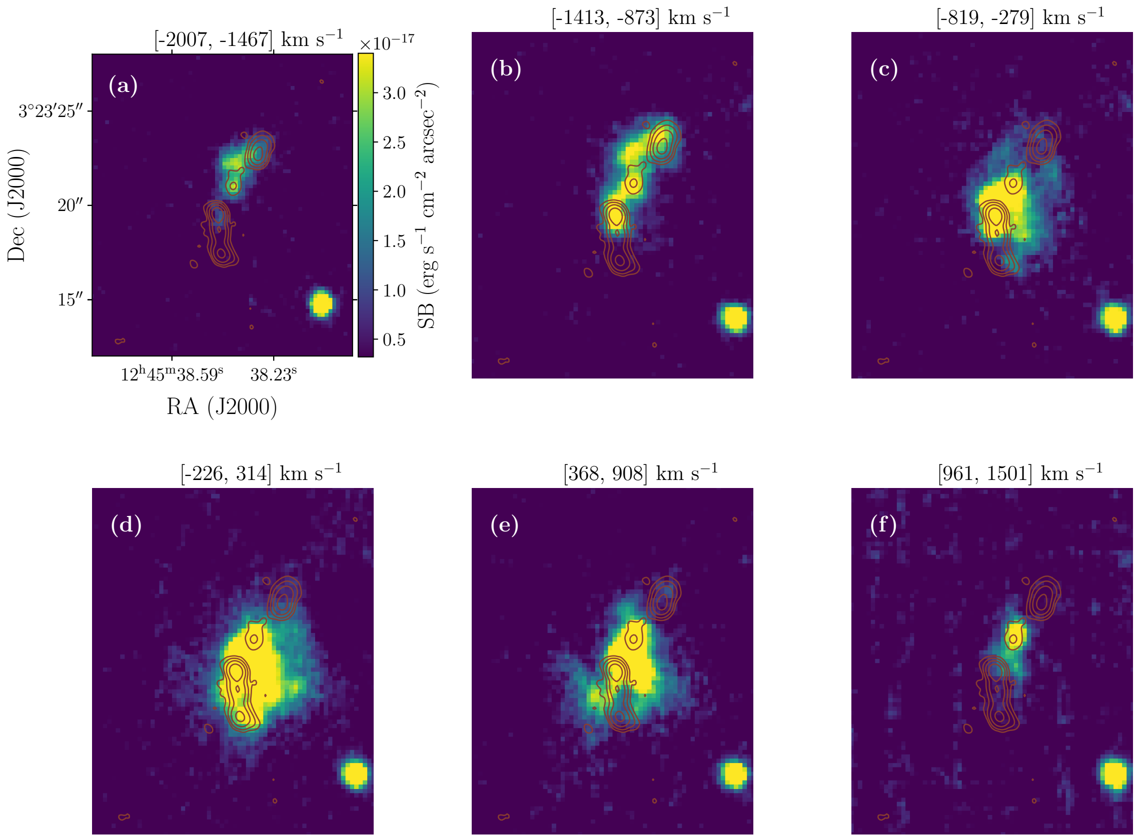

Figure 4.7: Lyα emission at different velocities to highlight the morphological variations of the nebula as a function of velocity. All the figures share the same coordinates and color scale and so the colorbar is valid for all panels. The continuum has not been subtracted from the Lyα image because its contribution is negligible everywhere, including the central aperture. The dimension of the Lyα image is 13×16 arcsec^2. The 3σ detection limit values for the mosaic images are in the range $\sim$ [2.2 - 4.6] $\times 10^{-18}$ erg s^{-1} cm^{-2} arcsec^2. The bright source to the SW is a star.

On the NE side of the nucleus, at the most blueshifted velocities (panels (a) and (b)), the Lyα emission is highly collimated along the radio axis and extends up to the edge of the radio source. This further demonstrates the significant impact of the radio source on the morphological and kinematic properties of the nebula at both the NE and SW sides of the nucleus.

Interestingly, there is a gap in the Lyα emission between the radio features B3 and B4 (panel(c)). This is naturally explained if the radio source is interacting more strongly with the ambient gas at these location and the line emission is enhanced as a consequence. An alternative scenario could be that the gas in that gap has been heated by shocks induced by the radio source to too high temperatures for Lyα emission to be efficient.

An additional, very interesting gaseous structure is the long filament that is more clearly seen in the full Lyα integrated image (Figures 4.6 and 4.15). It extends up to ~ 70 kpc from the AGN at both sides of the galaxy, at a position angle of $\sim 30°$.

4.4.2 Kinematic maps: spatial variation of W_{80}, asymmetry and v_{50}

The above results can be further visualized in the kinematic maps shown in Figure 4.8, where the spatial variation of W_{80}, v_{50} and A are shown (Section 4.3.3). A summary of the Lyα kinematic properties in all the apertures is presented in Table 4.2.

The first obvious result is that the kinematics of the gas is significantly different for the low surface brightness gas located beyond the radio structure, along the radio axis (see panel (b) in Figure 4.8). The lines are much narrower ($W_{80} \lesssim 750$ km s^{-1}) than in high surface brightness gas, especially when compared to the gas within and coincident with the radio features. The giant nebula shows a velocity shift of ~ 400 km s^{-1} between the north-western and south-eastern sides (see also van Ojik et al., 1996). Based on long slit spectroscopy along and perpendicular to the radio axis, van Ojik et al. (1996) proposed this is a giant rotating halo. Other scenarios such as radial motions (infall; e.g., Humphrey et al., 2007) may also be possible and arguably more likely based on the current data. We will discuss this in more depth in Section 4.5.

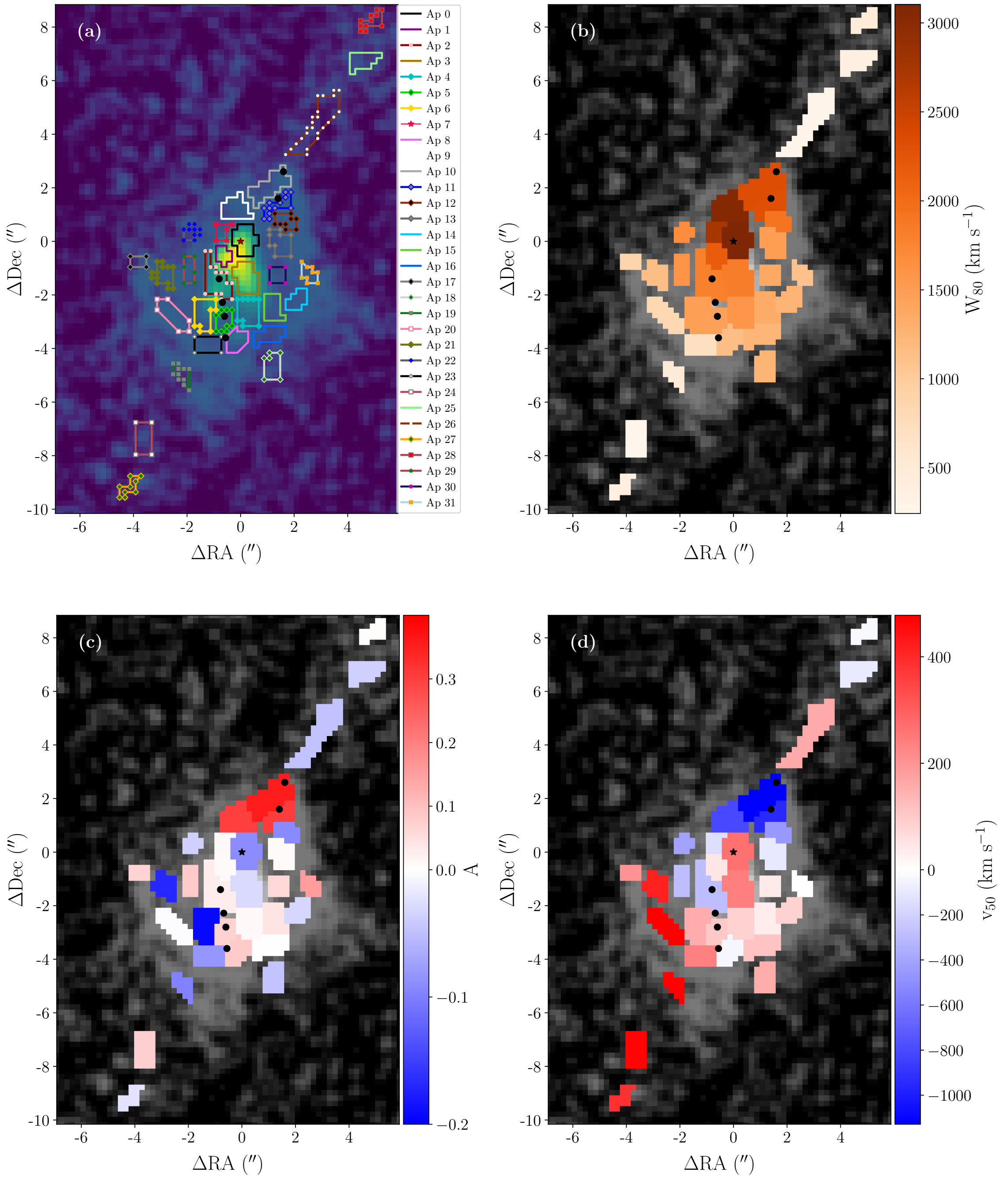

Figure 4.8: Lyα image overlayed by: (a) all the apertures to help identify the regions presented in the maps; (b) non-parametric line width, W_{80}; (c) asymmetry map; (d) v_{50} map. The values used to construct these maps are presented in Table 4.2. The black star shows the position of the nucleus and the black dots show the positions of the radio knots presented in Table 4.1.

Table 4.2: Parameters measured for all the apertures. (1) Aperture number; (2) signal-to-noise ratio; (3) W_{80} velocity width; (4) asymmetry*; (5) FWHM. These values are quoted for those apertures for which Lyα was fitted with a Gaussian profile; (6) velocity at 50% of total flux.

$^{(1)}$Aperture	$^{(2)}$SNR	$^{(3)}W_{80}$ (km s^{-1})	$^{(4)}$A	$^{(5)}$FWHM (km s^{-1})	$^{(6)}v_{50}$
0	44.1 ± 6.1	3103 ± 272	-0.09 ± 0.02		264 ± 82
1	39 ± 2	2159 ± 189	0.006 ± 0.03		48 ± 66
2	42 ± 4.5	1788 ± 151	0.03 ± 0.02		-283 ± 85
3	50 ± 6	1821 ± 141	-0.03 ± 0.02		242 ± 88
4	24.1 ± 3.2	1570 ± 191	0.01 ± 0.02		84 ± 65
5	16.7 ± 1.7	1460 ± 201	0.07 ± 0.05		101 ± 53
6	24.5 ± 2.7	1479 ± 151	-0.2 ± 0.02		154 ± 70
7	10.7 ± 1.5	2739 ± 272	0.01 ± 0.02		-144 ± 86
8	20.4 ± 1.6	1142 ± 170	0.08 ± 0.03		-40 ± 44
9	21.2 ± 3.5	3043 ± 173	0.3 ± 0.02		-808 ± 133
10	26.3 ± 4.2	2318 ± 169	0.4 ± 0.02		-1129 ± 202
11	10 ± 2	2288 ± 302	0.3 ± 0.02		-945 ± 135
12	9 ± 1	1912 ± 302	-0.09 ± 0.03		-452 ± 108
13	9.4 ± 1.3	1492 ± 243	0.007 ± 0.03		-102 ± 71
14	14 ± 2	1258 ± 212	-0.03 ± 0.04		85 ± 73
15	18 ± 3	1330 ± 149	0.04 ± 0.05		37 ± 82
16	10.7 ± 0.7	1236 ± 146	0.003 ± 0.006		109 ± 54
17	3.7 ± 0.6	874 ± 259	0.07 ± 0.2		198 ± 61
18	3.8 ± 0.8	1217 ± 243	-0.05 ± 0.04	1247 ± 208	154 ± 119
19	7.5 ± 1	501 ± 144	-0.1 ± 0.09		472 ± 132
20	13.5 ± 3.9	817 ± 162	-0.003 ± 0.08		478 ± 101
21	7.9 ± 1.3	1139 ± 197	-0.2 ± 0.05		416 ± 112
22	4 ± 0.8	1666 ± 316	-0.04 ± 0.03		-403 ± 86
23	12.5 ± 1.8	694 ± 146	-0.08 ± 0.07		236 ± 78
24	4.5 ± 0.5	292 ± 165	0.08 ± 0.2	243 ± 153	470 ± 119
25	3.6 ± 0.7	444 ± 194	-0.04 ± 0.2	361 ± 143	-92 ± 87
26	6.2 ± 0.8	349 ± 243	-0.05 ± 0.07	257 ± 118	157 ± 68
27	3.4 ± 0.5	236 ± 142	-0.02 ± 0.2	370 ± 189	386 ± 116
28	3 ± 0.6	423 ± 157	0.005 ± 0.2	473 ± 181	-30 ± 60
29	8.3 ± 0.9	1589 ± 337	0.07 ± 0.06		-288 ± 61
30	10.04 ± 1.2	1369 ± 193	0.06 ± 0.03		40 ± 38
31	6.2 ± 0.9	1111 ± 216	0.2 ± 0.05		-0.5 ± 45

*We note that some of the measurements of the asymmetry parameter are associated with large uncertainties. This has been taken into account when analysing the results.

Figure 4.8 shows that the most extreme extranuclear kinematics are identified at the location of the A1 and A2 (northern) hotspots. There, the highest W_{80} (panel (b)), the largest blueshifts (panel (d)) and the most prominent red asymmetry (panel (c)) are measured. As we will see in Section 4.4.3, the origin of this kinematic deviation relative to the underlying pattern is the contribution of a blueshifted split kinematic component, most likely produced by interaction with the radio source. At the location of the south-eastern radio features or adjacent to them, the kinematic impact is not so obvious. We will investigate this further in Section 4.4.3. Interestingly, Lyα is very broad ($W_{80} > 800$ km s^{-1}) also for gas located perpendicularly to the radio axis and outside the putative ionization cones. This will also be further explored in Section 4.5.

4.4.3 Spatial variation of the Lyα spectral profile

The maps shown in the previous sections help us visualize the morphological and kinematic information in two spatial dimensions. Very valuable information can be further obtained by visualizing the actual line profiles, as we do in this section (Figures 4.10 to 4.14). For instance, it helps visualizing and discerning potential effects of Lyα absorption vs. kinematics.

The inspection of the line profiles in all apertures shows two clear results already discussed in relation to the kinematic maps of the previous sections. On one hand, the lines are significantly narrower along the radio axis, beyond the radio structures (Figure 4.14). The second obvious result is that at several locations the line is split in two separate components (apertures 2, 6, 9, 10, Figure 4.10; apertures 7, 11, 12, Figure 4.12). The split components are clearest in apertures at or near the radio features (Figures 4.10 and 4.12, apertures 2, 9, 10, 11). The redder of the two components seems to be widely spread and traces the redshifted gas discussed above in the context of Figure 4.7. The blueshifted component is predominantly detected along and within the radio source and traces the highly collimated Lyα morphology along the radio axis seen in Figure 4.7 at the most blueshifted velocities.

At the location of the radio bent (aperture 2), in the southern hotspot, in addition to Lyα, we also detect emission from C IV , He II and C III] (Figure 4.9). This may be a consequence of the interaction between the radio jet and the ambient gas.

As we already mentioned, Lyα is highly sensitive to resonant scattering, but these main deviations (such as the split components) of the Lyα profile from a quiescent kinematic pattern do not appear to be an effect of that mechanism. The blueshifted component is likely to be a consequence of the interaction between the radio source and the gas, as discussed above. This is confirmed by the kinematic study of the nebula in optical rest frame by Nesvadba et al. (2017b) using [O III] λ5007 where they found that gas in the southern hotspot shows a velocity jump and an increase in line width (FWHM = 700 - 900 km s^{-1}) compared to the northern hotspot (FWHM ~ 300 km s^{-1}).

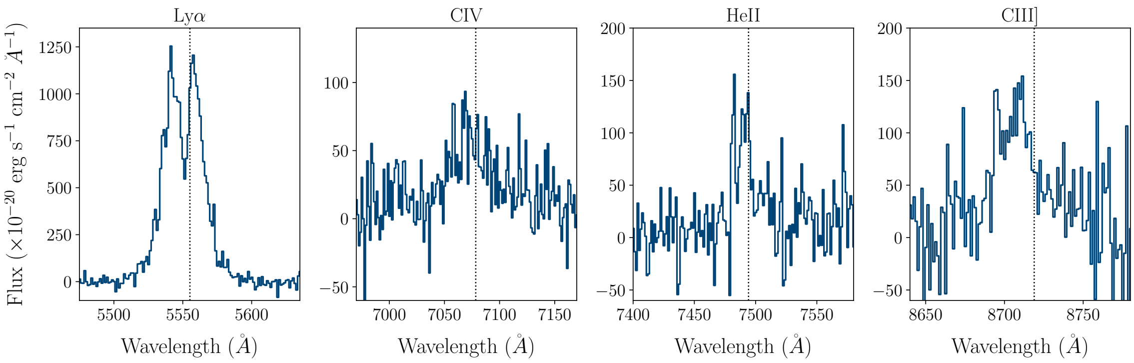

Figure 4.9: 1D spectrum of Lyα, C IV , He II and C III] emission lines extracted from aperture 2, coincident with the bending radio jet. The vertical dotted line marks the expected line wavelength for the systemic redshift.

Unlike Lyα, which shows a double peak and extremely perturbed kinematics (W_{80} = 2318 ± 169 km s^{-1}), the [O III] λ5007 gas in the northern hotspot is quiescent. In this region, [O III] λ5007 is blueshifted (~ -250 km s^{-1}) but not as strongly as Lyα (v_{50} ~ -1130 km s^{-1}). There are a few ways to explain this discrepancy: [O III] λ5007 may be less turbulent than Lyα in that region; by fitting a gaussian profile to [O III] λ5007 some flux may have been lost (particularly any faint second kinematic component). Lyα is also a much stronger line thus characteristics visible in Lyα may not be visible in other emission lines.

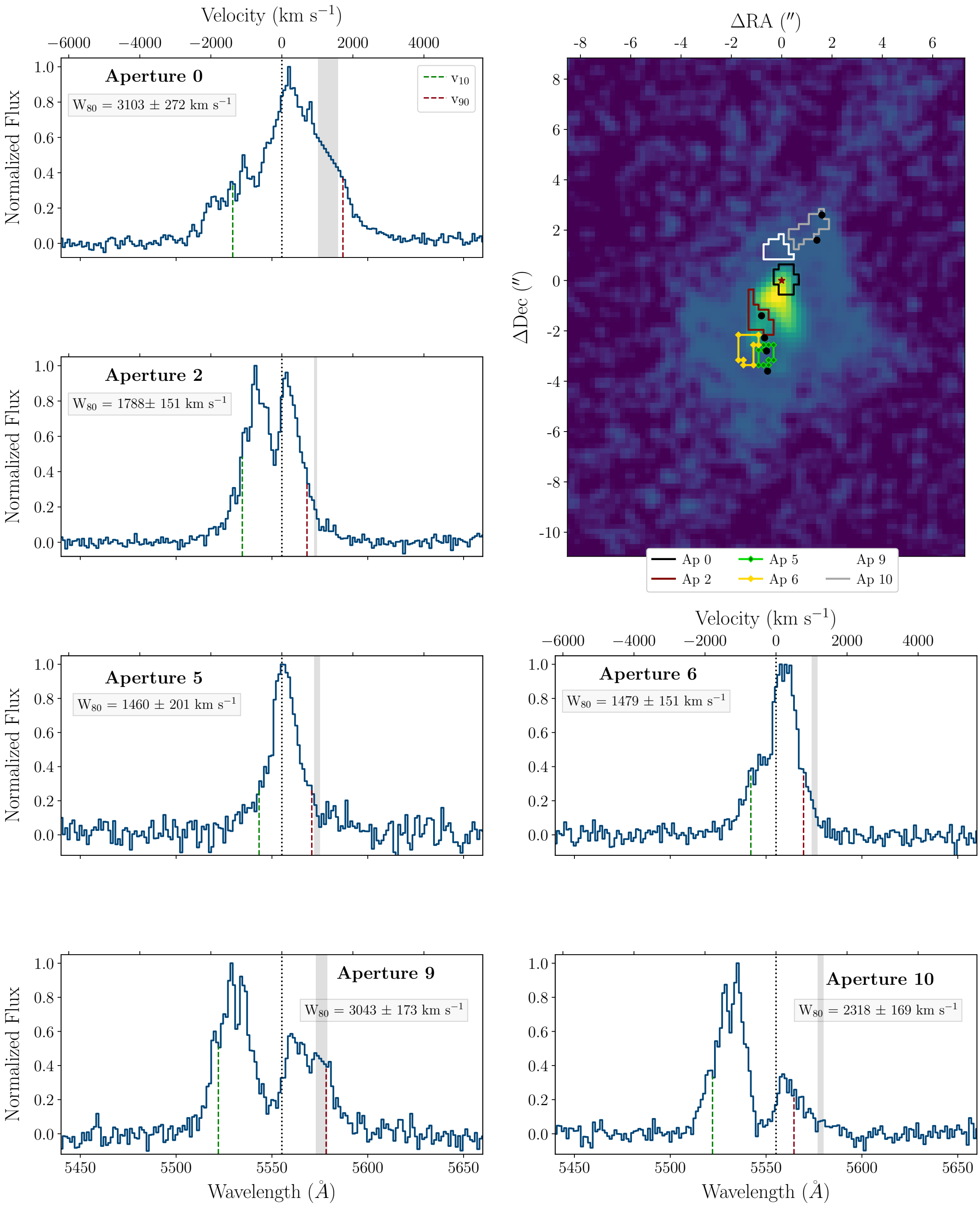

Figure 4.10: Apertures taken along the radio axis overlayed on the Lyα image and the corresponding normalized spatial profiles. The shaded grey regions mark regions interpolated to hide the sky line at 5575 Å. The Lyα image was created by collapsing the data cube in the wavelength dimension in the spectral range 5540 - 5570 Å and performing smoothing (0.85 pixel kernel) to highlight the nebula.

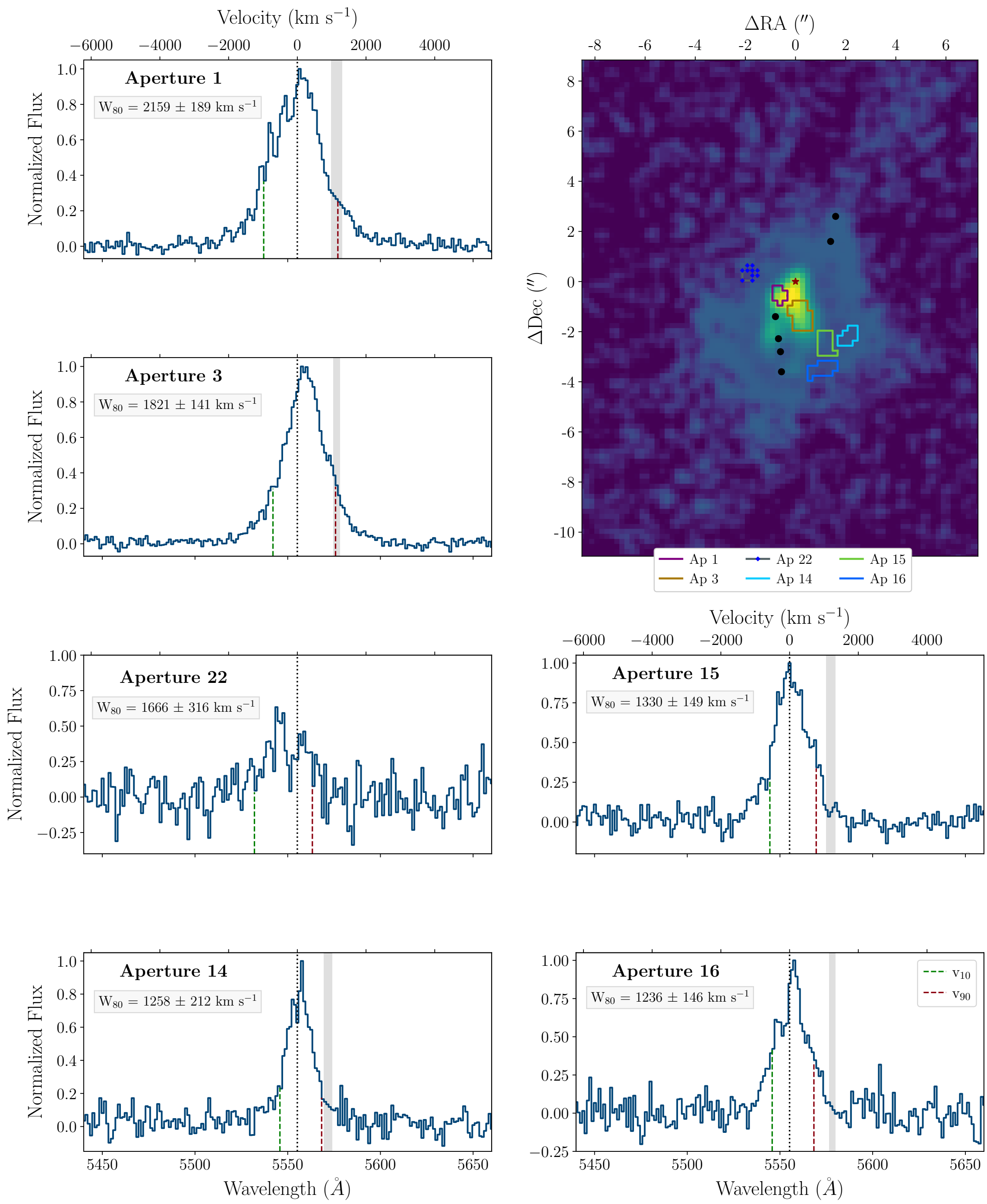

Figure 4.11: Apertures placed perpendicularly to the radio axis overlayed on the Lyα image and the corresponding spectra.

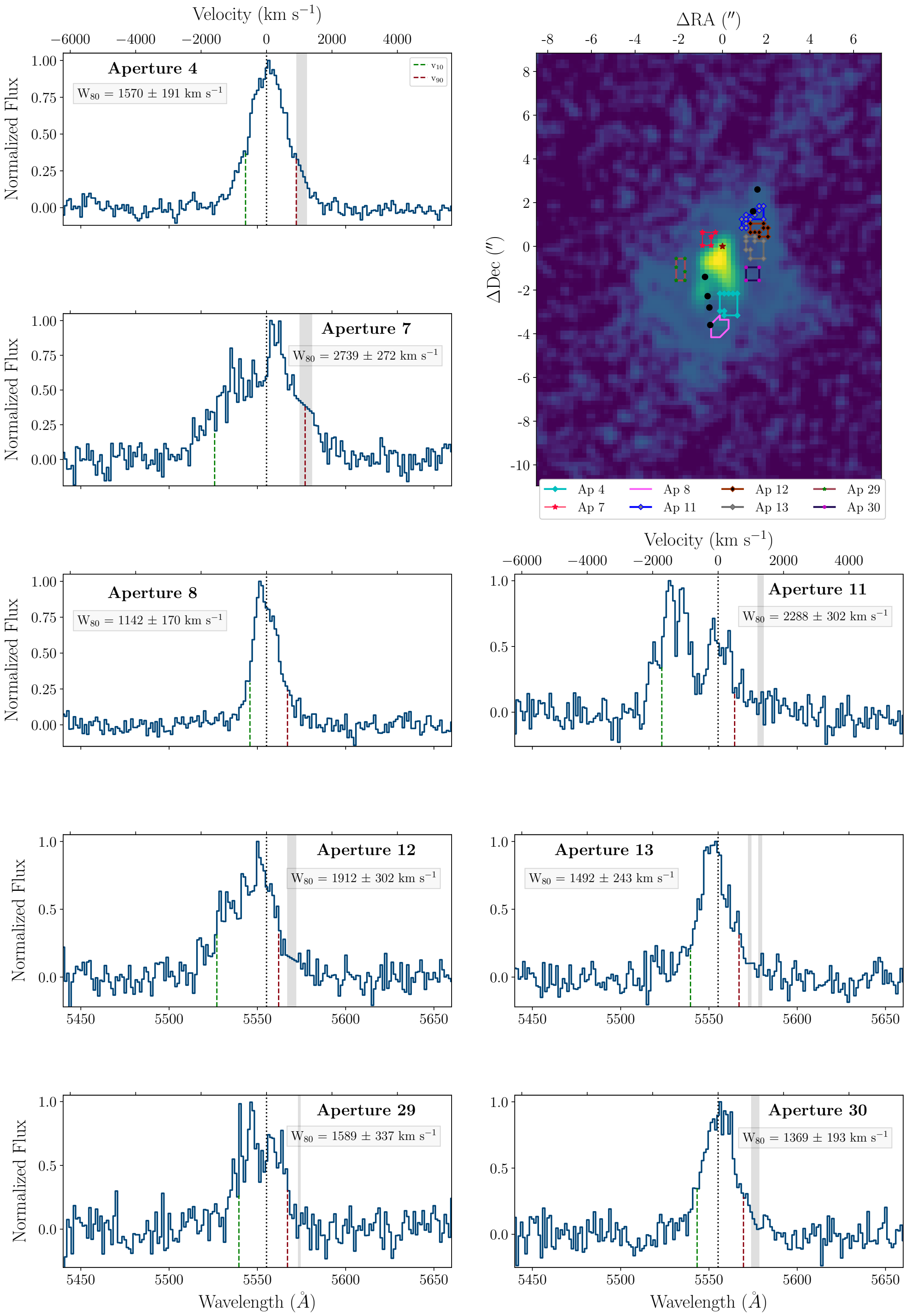

Figure 4.12: Same as Figure 4.10 for the apertures outside the central region.

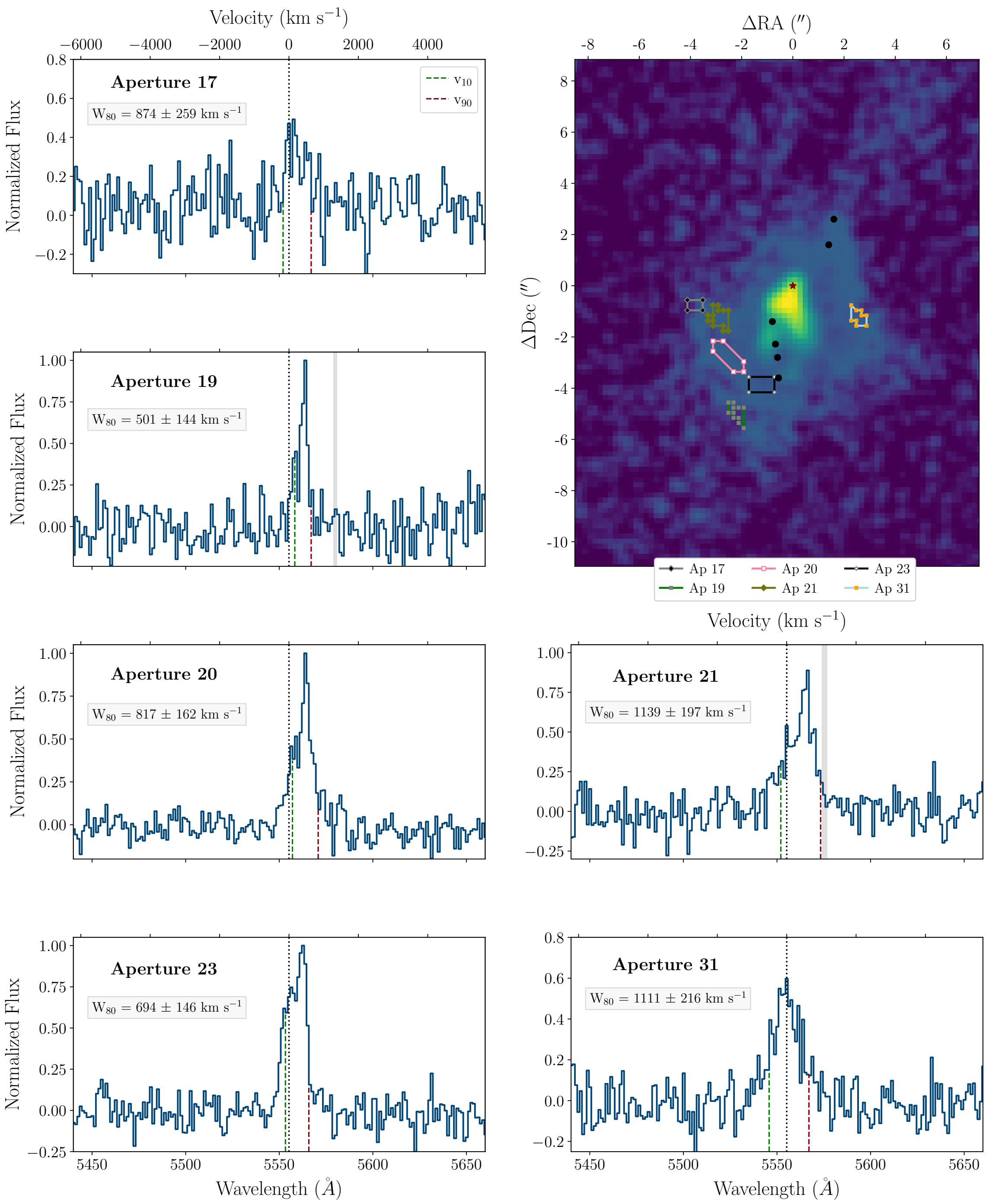

Figure 4.13: Same as Figure 4.10 for the apertures outside the central region.

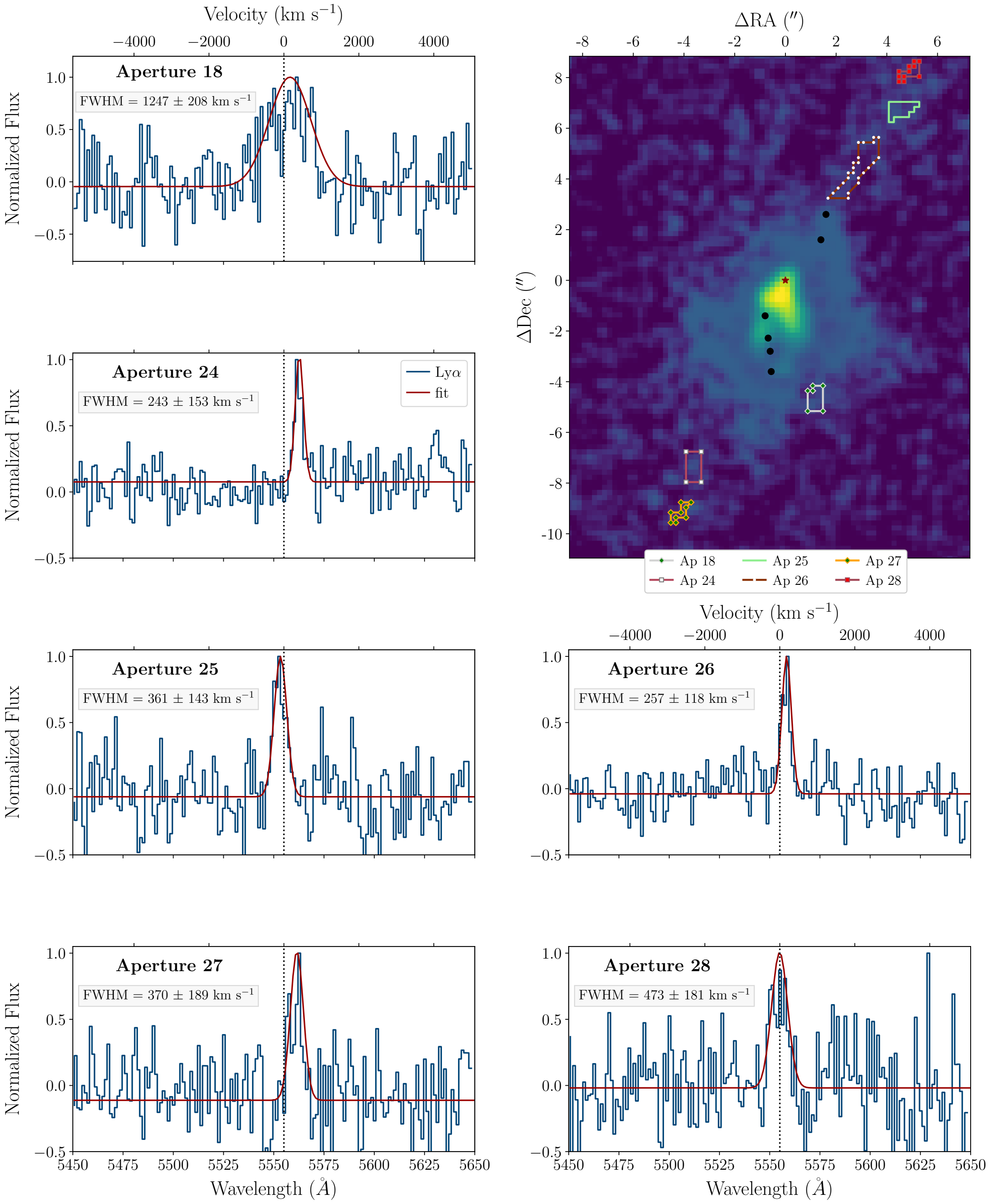

Figure 4.14: Outer apertures overlayed on the Lyα image, corresponding spectra and FWHM measurements.

Away from the radio structures the Lyα profiles are less extreme, however, the lines are rather broad and with complex kinematic profiles at numerous locations perpendicular to the radio axis, even outside the ionization cones, with W_{80} > 1000 km s^{-1} (e.g., Figures

4.12, 4.13). Although seeing smearing may play a role for gas adjacent, or very close to the nucleus (Villar-Martín et al., 2016), there is gas at too large distances for this to have any important effect on the observed gas properties. As an example, apertures 14, 15, 16, 22 to the SW, show W_{80} = 1236 - 1666 km s^{-1}, which is very broad (see Figure 4.11).

Although we cannot discard that resonant scattering may play a role at those locations, the appearance of the line profiles tentatively suggests that they are intrinsically very broad. This affirmation is based on the fact that the line profiles are rather symmetric (Figure 4.11) in general (apertures 1, 3, 22, 14, 16). The potential effects of absorption are seen as some very narrow features (e.g., apertures 1 and 14) or as a missing fraction of the blue wing (aperture 15). Reconstructing this profile would probably result on a broader intrinsic line (Wang et al., 2023b).

In order to evaluate the potential impact of resonant scattering, much deeper spectroscopy would be very valuable with the aim of detecting other non resonant emission lines such as He II in the optical or [O III] λ5007 in the near infrared, which would allow us to estimate what the velocity profile of Lyα might be without any H I absorption.

The outer apertures show quiescent kinematics (FWHM $\lesssim$ 750 km s^{-1}), with the peak of the Lyα profile relatively close to the systemic redshift of the galaxy. Along the filament, the line is comparatively very narrow. For those spectra where the line is detected with good S/N and can be clearly fitted with a Gaussian (see apertures 24, 25, 26 in Fig. 4.14), Lyα is as narrow as FWHM ~ 240 - 360 km s^{-1}.

4.5 Discussion

4.5.1 Powering of the Lyα nebula

The Lyα nebula is asymmetric and more extended in the direction of the radio axis (~ 148 kpc), but it surrounds the object completely, showing widespread emission. It is also much larger than the gas traced by the optical rest frame lines (see also Wang et al., 2023b). Based on VLT/SINFONI data and the [O III] λ5007, Nesvadba et al. (2017b) measured a projected size of the emission-line region of 39 kpc × 6.7 kpc (in our cosmology).

Along the radio axis and within the radio lobes the gas kinematics is very turbulent. This is typical of giant nebulae surrounding HzRGs (e.g., van Ojik et al., 1996; Villar-Martín et al., 2003; Humphrey et al., 2006; Villar-Martín et al., 2007b; Reuland et al., 2007). The Lyα emission is strongly blueshifted (v_{50} < -1000 km s^{-1}) and shows large W_{80} values (W_{80} > 1500 km s^{-1}) indicative of highly turbulent motions. In the perpendicular direction, away and far from the radio axis, widespread redshifted Lyα emission is detected (see also van Ojik et al., 1996; Wang et al., 2023b). Perpendicularly to the radio axis, the line profiles are narrower than those in the high surface brightness regions, but they still show turbulent motions (e.g., apertures 21 and 31 with FWHM ∼ 1100 km s^{-1}), with small velocity offsets relative to the central regions.

We find that the Lyα spectral profile is in general dominated by the motion of the gas, rather than resonant scattering, at least for the gas within the ionization cones. This is confirmed by the similar morphological and kinematic correlation between the [O III] λ5007 emission and the radio structures (Nesvadba et al., 2017b). This line also shows very turbulent kinematics, with [O III] λ5007 FWHM ∼ 2500 km s^{-1} in the central regions (see also Wang et al., 2023b). Outflows induced by the radio source are the most likely mechanisms responsible for the extreme gas motions (Villar-Martín et al., 1999a; Villar-Martín et al., 2003; Humphrey et al., 2006; Nesvadba et al., 2017b; Vernet et al., 2017).

Different mechanisms are expected to be responsible for the excitation of the gas with varying importance across the giant nebula (e.g., Villar-Martín et al., 1997; Humphrey et al., 2008a; Arrigoni Battaia et al., 2019; Mitchell et al., 2021; Li et al., 2022). AGN related processes (shocks induced by the radio source and AGN photoionization) are expected to dominate within the ionization cones (e.g., Villar-Martín et al., 1997; Humphrey et al., 2008a; Nesvadba et al., 2017b). The clear morphological association between the highest velocity and most blueshifted Lyα emission, which is highly collimated along the radio axis and constrained within the radio source edges, suggests that shock excitation dominates along and within the radio source edges, but it is not clear whether AGN photoionization may dominate. Because shock and AGN photoionization models overlap in the predicted line ratios, it is not possible to discern between both types of mechanisms even when a rich data set of both optical and UV rest-frame emission lines is available (Humphrey et al., 2008a).

The gas outside the putative ionization cones is of special interest. If the AGN does not affect its properties, such Lyα emitting gas reservoirs may be good tracers of the intrinsic gas properties, undistorted by the nuclear activity.

Unless the AGN radiation is filtering out through an obscuring porous torus, AGN photoionization needs to be discarded to excite the Lyα emission at those locations. Stellar photoionization by widespread star formation in the circumgalactic medium (Hatch et al., 2008; Emonts et al., 2016) may play a role, but the turbulent kinematics (see above) suggests that a mechanism generating shocks is at work.

Another possible mechanism is gravitational cooling radiation. Numerical simulations suggest that infalling gas through cooling flows is an important process in galaxy formation. In this case, a primordial gas halo surrounds the galaxy, and as the gas falls into the dark matter halo potential, it is collisionally excited by shocks emitting Lyα photons while converting gravitational potential energy into kinetic and thermal energy. I.e., the extended Lyα emission arises due to gas losing its gravitational energy as it falls into the galaxy's dark matter halo. In very massive halos ($\gtrsim 1 \times 10^{12}$ $M_{\odot}$; e.g., Rosdahl and Blaizot, 2012) extended Lyα emission (> 100 kpc) can be produced as a result of accretion from the IGM. The shocks may also be responsible for the observed turbulent kinematics.

In recent works, low to intermediate power jets ($P_{1.4GHz} \lesssim 10^{25}$ W Hz^{-1}) have been found to perturb the gas located perpendicularly to the radio axis and outside the ionization cones, enhancing both emission and the line widths at those locations, which is a signature of turbulent kinematics (e.g., Villar-Martín et al., 2017; Venturi et al., 2021; Venturi et al., 2023).

Three-dimensional hydrodynamic relativistic simulations have also shown that if the radio jets propagate in a clumpy ISM, the originally well-directed jets inflate energy-driven bubbles that strongly affect the ambient gas in their host galaxies. The shocks that result from the interactions between the jets and the clumpy ISM create a multiphase ISM and radial outflows that are able to affect the gas both along and perpendicularly to the radio axis (Mukherjee et al., 2016). Although a high power jet such as the one in 4C+03.24 ($P_{1.4} \sim 10^{28.7}$; Nesvadba et al., 2017b) can remain relativistic to large scales and drill with relative ease through tens of kpc, deep radio images of radio galaxies reveal giant low surface brightness radio structures that span (and can therefore affect) huge volumes well onto the CGM (Thwala et al., 2019; Candini et al., 2023).

The Lyα emission outside the putative ionization cones and the turbulent kinematics could therefore be due to the interaction of so far undetected radio structures that extend perpendicularly to the main radio axis and fill a huge volume.

Another possibility is that the gas outside the ionization cones is not ionized, but neutral, and the Lyα emission is due to resonant scattering by this gas of the Lyα photons from the high surface brightness ionized regions within the cone (Villar-Martín et al., 1996; Wang et al., 2023b). Simulations have shown such a mechanism can generate large Lyα nebulae ($\sim$ 100 kpc; e.g., Dijkstra, 2017; Costa et al., 2022). This mechanism can broaden the Lyα profile depending on the conditions of the extended neutral halo. Definitive detection of scattered Lyα radiation in gas halos requires deep polarimetric observations, since this mechanism is predicted to produce a coherent pattern of linear polarization (Dijkstra and Loeb, 2008). Indeed, the polarization signature of scattered Lyα has been detected in a Lyα blob (Hayes et al., 2011) and in the extended halo of a $z > 2$ radio galaxy (Humphrey et al., 2013b).

4.5.2 Nature of the Lyα nebula

The nature of the extended emission line halo has been discussed in van Ojik et al. (1996), Ohyama and Taniguchi (2004) and more recently in Wang et al. (2023b). van Ojik et al. (1996) suggested that the morphology and kinematics of the Lyα outer halo were indicative of large scale rotation and could represent gas accreted from the environment at earlier times. Assuming that the median velocity (v_{50}) represents the bulk velocity of the emission, and taking into account the large velocity widths measured in most of the nebula (including perpendicularly to the radio axis) we see no evidence of such large scale ordered kinematics (see Figure 4.8).

We detect a filament of faint Lyα emission along the radio axis, at both sides of the nucleus, extending beyond the radio sources (aperture 19 and apertures 24 to 28; see Figure 4.15), up to $\sim$ 71 kpc and $\sim$ 72 kpc to the SE and NW, respectively. The Lyα emission in these regions shows quiescent gravitational motions, with narrow line widths (FWHM $<$ 700 km s^{-1}) and low median velocities (-90 $\lesssim v_{50} \lesssim$ 480 km s^{-1}), with a velocity shift of $\sim$ 400 km s^{-1} between the northern and southern sides.

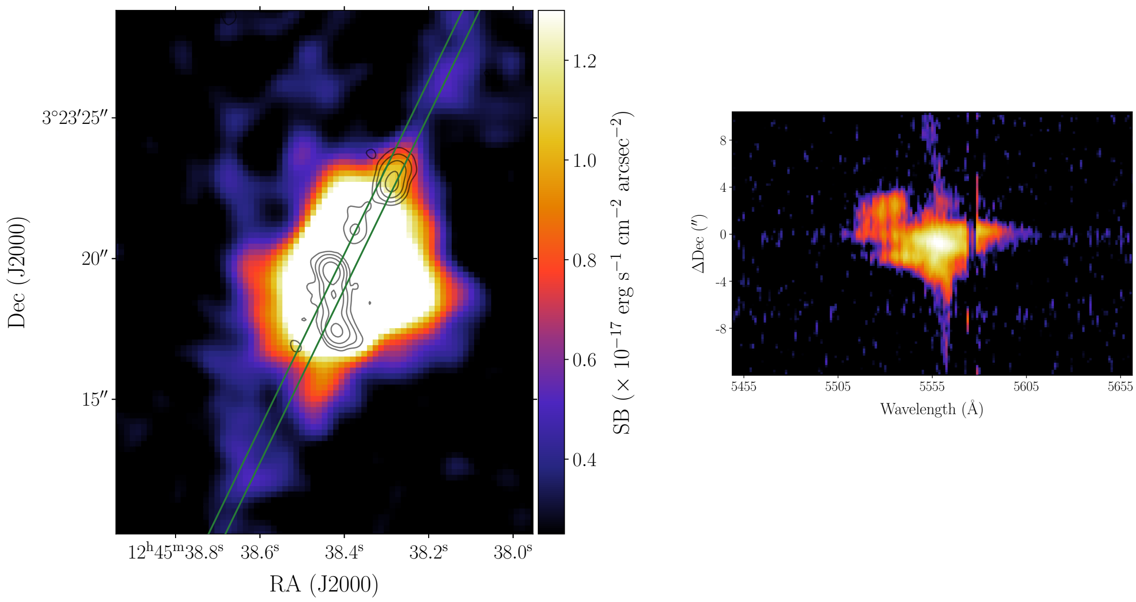

Figure 4.15: Left: Continuum subtracted Lyα image smoothed with a two pixel kernel. The emission in this image is above the 3σ detection limit ($\sim 2.5 \times 10^{-18}$ erg s^{-1} cm^{-2} arcsec^{2}). For reference, the radio contours and the pseudo-slit used to create the long-slit image are also shown. Right: Two dimensional image (smoothed with a two pixel kernel) extracted from the datacube, highlighting the filament detected at both sides of the nucleus.

The velocity map shows that in the southern region (the side closer to us according to polarization studies by van Ojik et al., 1996) the gas is redshifted relative to the nucleus of the galaxy and in the northern region the gas is mostly blueshifted compared to the central region.

The morphology and kinematics of the Lyα emission in this filament suggest that the gas along the radio axis, beyond the radio sources, is infalling towards the central regions of the nebula. This gas becomes visible as Lyα emission due to the ionizing radiation of the AGN.

Models of galaxy formation predict that the majority of gas in the high redshift universe ($z > 3$) is distributed along filaments (e.g., Martizzi et al., 2019) that are difficult to observe in emission due to their low density. A workaround has been to observe regions where strong ionizing sources (such as AGN or star-forming galaxies) are present, which can make the filaments observable in Lyα emission (Cantalupo et al., 2005). Such observations have discovered extended Lyα halos showing filamentary structures around various HzRGs and quasars (Reuland et al., 2003; Cantalupo et al., 2014; Vernet et al., 2017; Umehata et al., 2019).

If the filaments observed in this work are due to infalling gas, then the gas may have been ejected earlier from the central regions and is falling back to the galaxy or may be gas accreted from the CGM or from the IGM.

In summary, we argue that the extended Lyα emission observed around 4C+03.24 is probably the result of several mechanisms acting simultaneously. To constrain the contribution from each mechanism it would be of great interest to obtain much deeper optical (UV rest frame) and especially near infrared (optical rest frame) integral field spectroscopic data mapping the entire nebula to investigate whether lines other than Lyα are detected. This would demonstrate that the gas is ionized, rather than neutral, and provide valuable information about the possible ionization mechanisms. This would also provide very valuable information to constrain the nature and origin of the giant nebula, which is still an open question (van Ojik et al., 1996; Ohyama and Taniguchi, 2004; Wang et al., 2023b).

4.6 Conclusions

The Lyα nebula surrounding 4C+03.24 is asymmetric, showing more extended emission in the direction of the radio axis (~ 148 kpc) than perpendicularly to it (~ 50 kpc). In general, the Lyα emission shows perturbed kinematics, both along and perpendicularly to the radio axis. The regions along the radio axis and beyond the radio sources are the exception, showing quiescent kinematics and filamentary structure. The kinematics and morphology of the Lyα nebula surrounding 4C+03.24 are complex, suggesting the presence of different kinematic components:

- Highly collimated blueshifted Lyα emission along the radio axis, constrained by the radio structures, showing disturbed kinematics (W_{80} > 1500 km s^{-1}) which we suggest is the result of interactions between the radio jets and the ambient gas.

- Turbulent (700 km s^{-1} < W_{80} < 1500 km s^{-1}) Lyα emission detected perpendicularly to the radio axis, outside the putative ionization cones, of unclear origin. While we believe that AGN photoionization does not play a role, other mechanisms such as cooling radiation, shocks or resonant scattering may be responsible for the Lyα emission in these regions. The turbulent kinematics suggest that a mechanism related to shocks is powering the emission in these regions. One possible explanation is that as the radio jets expand, they shock the clumpy ambient gas inducing radial outflows that are able to shock the gas both along and perpendicularly to the radio axis.

- A filament of Lyα emission, detected along the radio axis beyond the radio structures, at both sides of the nucleus, showing quiescent motions (FWHM < 700 km s^{-1}) and low median velocities (-90 $\lesssim v_{50} \lesssim$ 480 km s^{-1}). Due to its kinematics, we suggest that this gas is infalling towards the central regions.

4C03.24 is embedded in a giant ($\sim 50 \times 150$ kpc^2), widely spread nebula. The radio source is propagating through this gas reservoir, inducing turbulence along and possibly perpendicularly to the radio axis, up to several tens of kpc from the AGN. In the process, it modifies dramatically both the kinematics and the morphology of the gas. The radio source has also been affected by the interaction, as the sharp SE bend demonstrates.

In the outskirts of the nebula an additional, apparently different gas component has been detected. It is a very narrow filament that extends up to $\sim$ 71 kpc and $\sim$ 72 kpc to the SE and NW of the host galaxy and is very tightly aligned with the radio axis. Its relatively quiescent kinematics in comparison with the orientation of the system, suggests that the filament is infalling. It may be physically connected and feeding the inner, turbulent, high surface brightness and more widespread Lyα nebula. An interesting possibility is that we are witnessing the growth of the host galaxy by accretion of circumgalactic gas streams. Simulations have predicted that steady streams of cold gas penetrate the dark matter halos of galaxies and provide the raw material necessary to sustain star formation. Rather than being cold (molecular) gas, the 4C03.24 filament is probably ionized (detected in Lyα) and may have been ionized by the AGN continuum, however scattering by neutral gas or collisional ionization cannot be discarded. Accreting gas streams have been detected via the Lyα emission line around other distant massive galaxies (e.g., Martin et al., 2015; Umehata et al., 2019; Bacon et al., 2021; Daddi et al., 2021; Emonts et al., 2023).

Chapter 5

Summary and Future work

HzRGs are great candidates to study the evolution of massive galaxies. Due to their characteristics, radio-mode feedback, quasar-mode feedback and the host galaxies can be studied simultaneously. They are also often associated with giant Lyα nebulae that allow us to trace their ISM and CGM and study the impact of AGN feedback on their host galaxies.

This work has studied different mechanisms related to the AGN phenomena and how they influence the ionization, kinematic and morphological properties of the ionized gas in the most luminous active galaxies (type 2 quasars and narrow line radio galaxies). Because of their interest in cosmological studies, the investigation has been focused especially (but not only) on high z $\sim$ 2 - 4 active galaxies, although the methodology and knowledge acquired can be applied to AGN at different redshifts.

Two well differentiated projects have been completed. The first one had the goal of investigating the influence that the inclusion of non-thermal electron energy distributions (EEDs) has in the predicted emission line spectra of active galaxies based on AGN photoionization models. For this, a large set of photoionization models was built with the photoionization code MAPPINGS 1e (Chapter 2). They span a broad (but realistic) range of parameters both for the gas (density, metallicity and ionization parameter) and for the slope of the ionizing continuum. Most importantly (and here lies one of the main novelties of this work), a diversity of EEDs was considered, including the Maxwell-Boltzmann (M-B) distribution, usually assumed in the literature, and deviations from it, parameterized by a diversity of κ EEDs.

This theoretical investigation has been completed by comparing (for the first time in the case of the κ EEDs) the emission line ratios predicted by the models with a large data set of measured rest-frame UV (optical observed frame) ratios for 15 HzRGs, 126 QSO2, and two Seyfert galaxies. The comparison was also extended to the rest-frame optical (observed in the near infrared) line ratios for a subset of $\sim$ 12 objects for which this information was available. In total, up to 23 emission lines where considered in this study, covering a broad ionization range (from low (e.g., [O I]) to very high ionization species (e.g., N V)).

The work in this thesis has demonstrated the strong impact that the inclusion of non-thermal electron energy distributions has on the predicted emission line ratios of luminous type 2 AGN (Chapter 2). Using an identical set of input parameters (gas density, abundance, ionization parameter, ionizing continuum) in the photoionization models, non-thermal EEDs and the M-B models predict significantly different line ratios. We have shown that κ-distributed electron energies strongly enhance the flux of high-excitation collisionally excited lines. This results in strong enhancement of some UV and optical emission lines, and in a reduction of the flux of IR lines compared to the M-B distribution, especially for strong deviations from equilibrium (i.e. low values of κ). The impact of adopting κ distributions strongly depends on the gas metallicity and ionization parameter.

By comparing the line ratios computed by the photoionization models with line ratios compiled from the literature, in Section 3 we showed that κ distributions give an overall better fit to the observations. This highlights the interest and importance of considering supra-thermal electrons in photoionization models.

This study can be expanded in different ways. On one hand, a great improvement would come from a more complete data set of near infrared spectroscopy to measure optical rest-frame emission lines for as many objects as possible. One of the main difficulties encountered in this study was the lack of this information for most AGN in our sample. By working with optical data, at the redshift range studied here we have been restricted to a limited number of rest-frame UV lines for the vast majority of objects. An obvious way to expand this work will be to compare the predictions of the models that best reproduce the NLR UV line ratios, with the optical ones for the same objects, using NIR spectroscopy.

The second project is presented in Chapter 4. It is the study of the giant (> 100 kpc) Lyα nebula that surrounds 4C+03.24, a radio galaxy at z = 3.57 based on VLT-MUSE archive integral field spectroscopy. A VLA radio map of the source has been also used in the study.

In consistency with previous works, we detect widespread Lyα emission, which is elongated along the main radio axis, with a maximum extent along this axis of $\sim$ 148 kpc, and $\sim$ 50 kpc perpendicularly to it. Gas is detected within and well beyond the radio structures, both along and well away, perpendicular to them. The kinematic properties of the nebula are clearly correlated with the morphology of the radio source, as found in other HzRGs. This is evidence that the radio source is interacting with the gas as it advances across the giant nebula. The impact of the interaction is obvious both on the gas and on the radio source, which has suffered a sharp bend as a consequence.

Two other interesting results have emerged from this study. On one hand, although the most turbulent gas is clearly associated with the radio source, kinematically perturbed, low surface brightness gas is also detected outside the putative ionization cones of the AGN, far from the radio source and perpendicular to it, up to $\sim$ 29 kpc from the nucleus. The possible excitation mechanism and origin of the gas turbulence have been discussed, although the final answer remains open.

In addition, a filament of very low surface brightness Lyα emission has been detected along the radio axis beyond the radio structures, at both sides of the nucleus. It shows comparatively quiescent kinematics. We suggest that this gas is infalling towards the central regions, possibly feeding the widespread inner gas reservoir.

In spite of the relatively low S/N of the available data, the study of the giant ionized nebula associated with 4C+03.24 is yet another example of the extraordinary advantage of a large field of view ($1' \times 1'$) and high sensitivity integral field spectroscopy for the investigation of giant nebulae in the high z universe. This said, significantly deeper data would have allowed a more in depth study, if lines other than Lyα from the giant nebula could have been detected. Although we have carefully argued the usefulness of Lyα as kinematic tracer in this particular case, lines such as N V , He II, C IV and C III] in the extended halo would have been of great value. They would provide rich additional information at different locations about the excitation mechanisms, the ionization and physical properties of the gas, as well as diagnostics for the gas metallicity. This could be key to disentangle between the different mechanisms in action. Such as gas accretion from the CGM (expected to be less chemically enriched) or gas ejection from the host galaxy via outflows (chemical enriched).

A very interesting follow up of the two main projects developed in this thesis would be to map and model the spatially resolved emission line ratios of the ionized gas in HzRGs and QSO2s using deep optical and, very especially, near infrared high spatial resolution integral field spectroscopy. With the James Webb Space Telescope (JWST; Gardner et al., 2006; Rigby et al., 2023), excellent opportunities have emerged. Thanks to the high efficiency in the near infrared and the high spatial resolution, it is now possible to map in great detail the environment of high-z radio galaxies and QSO2s with rest-frame optical emission lines.

The ionization state, kinematics, physical properties of the gas and the abundances can be studied in two spatial dimensions with the near-infrared spectrograph (NIRSpec; Jakobsen et al., 2022) with very high spatial resolution and spectral resolution of R = 2700 ($\sim$ 110 km s^{-1}). An advance from ground-based near-IR studies (spatial resolution $\sim$ 5 kpc) to spatial resolutions of less than 1 kpc will be achieved (the cost is a smaller field of view of 3.1×3.2 arcsec^2). It is possible to detect spatially extended optical lines, key for nebular diagnostics (density, reddening, ionization level), including very faint lines such as [O III] λ4363 or [N II] λ5755, essential to constrain the electron temperature. In this way, the metallicity of the gas can be mapped in two spatial dimensions and with much greater accuracy than that provided by the UV emission lines (Pérez-Montero et al., 2019).

Overall, studying the ionized gas in high-z luminous active galaxies is essential to investigate the impact of the nuclear activity on the host galaxy, from the nuclear region (the classical NLR) out onto the CGM, and, ultimately, the potential impact on evolution of these massive systems. Ultimately, this will help understand jet/AGN/stellar feedback in HzRGs, whether and how star formation is modified by the presence of an active SMBH and, thus, the role played by nuclear activity in the evolution of the host galaxies.

Bibliography

Adelberger, K. L. et al. 2003. *ApJ*, vol. 584, pp. 45–75. DOI: 10.1086/345660.

Alexandroff, R. et al. 2013. *MNRAS*, vol. 435, pp. 3306–3325. DOI: 10.1093/mnras/stt1500.

Ali, A. and Dopita, M. A. 2019. *MNRAS*, vol. 484, pp. 3251–3266. DOI: 10.1093/mnras/stz201.

Allen, M. G. et al. 2008. *ApJS*, vol. 178, pp. 20–55. DOI: 10.1086/589652.

Anderson, M. E. et al. 2013. *ApJ*, vol. 762, p. 106. DOI: 10.1088/0004-637X/762/2/106.

Anderson, M. E. et al. 2016. *MNRAS*, vol. 455, pp. 227–243. DOI: 10.1093/mnras/stv2314.

Antonucci, R. 1993. *ARA&A*, vol. 31, pp. 473–521. DOI: 10.1146/annurev.aa.31.090193.002353.

Ao, Y. et al. 2020. *Nature Astronomy*, vol. 4, pp. 670–674. DOI: 10.1038/s41550-020-1033-3.

Aravindan, A. et al. 2023. *ApJ*, vol. 950, p. 33. DOI: 10.3847/1538-4357/acca7c.

Archibald, E. N. et al. 2002. *MNRAS*, vol. 336, pp. 353–362. DOI: 10.1046/j.1365-8711.2002.05725.x.

Arnold, H. et al. 2021. *PhRvL*, vol. 126, p. 135101. DOI: 10.1103/PhysRevLett.126.135101.

Arribas, S. et al. 2014. *A&A*, vol. 568, A14. DOI: 10.1051/0004-6361/201323324.

Arrigoni Battaia, F. et al. 2018. *MNRAS*, vol. 473, pp. 3907–3940. DOI: 10.1093/mnras/stx2465.

Arrigoni Battaia, F. et al. 2019. *MNRAS*, vol. 482, pp. 3162–3205. DOI: 10.1093/mnras/sty2827.

Asmus, D. 2019. *MNRAS*, vol. 489, pp. 2177–2188. DOI: 10.1093/mnras/stz2289.

Asmus, D. et al. 2016. *ApJ*, vol. 822, p. 109. DOI: 10.3847/0004-637X/822/2/109.

Bañados, E. et al. 2018. *Nature*, vol. 553, pp. 473–476. DOI: 10.1038/nature25180.

Bacon, R. et al. 2010. *SPIE Conf. Ser*, vol. 7735, p. 773508. DOI: 10.1117/12.856027.

Bacon, R. et al. 2021. *A&A*, vol. 647, A107. DOI: 10.1051/0004-6361/202039887.

Baldwin, J. A. et al. 1981. *PASP*, vol. 93, pp. 5–19. DOI: 10.1086/130766.

Baring, M. G. 1991. *MNRAS*, vol. 253, pp. 388–400. DOI: 10.1093/mnras/253.3.388.

Barvainis, R. et al. 2005. *ApJ*, vol. 618, pp. 108–122. DOI: 10.1086/425859.

Beck, M. et al. 2016. *ApJ*, vol. 818, p. 138. DOI: 10.3847/0004-637X/818/2/138.

Beckmann, V. and Shrader, C. 2012. *Active Galactic Nuclei*. Wiley-VCH Verlag GmbH & Co. KGaA, Boschstr., Weinheim, Germany, p. 69469.

Behroozi, P. S. et al. 2013. *ApJ*, vol. 770, p. 57. DOI: 10.1088/0004-637X/770/1/57.

Bellstedt, S. et al. 2020. *MNRAS*, vol. 498, pp. 5581–5603. DOI: 10.1093/mnras/staa2620.

Bennert, N. et al. 2006a. *A&A*, vol. 456, pp. 953–966. DOI: 10.1051/0004-6361:20065319.

Bennert, N. et al. 2006b. *A&A*, vol. 446, pp. 919–932. DOI: 10.1051/0004-6361:20053571.

Bennett, J. S. and Sijacki, D. 2020. *MNRAS*, vol. 499, pp. 597–615. DOI: 10.1093/mnras/staa2835.

Benson, A. J. et al. 2003. *ApJ*, vol. 599, pp. 38–49. DOI: 10.1086/379160.

Best, P. N. et al. 2006. *MNRAS*, vol. 368, pp. L67–L71. DOI: 10.1111/j.1745-3933.2006.00159.x.

Bicknell, G. V. et al. 2004. *New Astron. Rev.*, vol. 48, pp. 1151–1155. DOI: 10.1016/j.newar.2004.09.005.

Biernacki, P. and Teyssier, R. 2018. *MNRAS*, vol. 475, pp. 5688–5703. DOI: 10.1093/mnras/sty216.

Binette, L. et al. 1985. *ApJ*, vol. 297, pp. 476–491. DOI: 10.1086/163544.

Binette, L. et al. 1996. *A&A*, vol. 312, pp. 365–379.

Binette, L. et al. 2012. *A&A*, vol. 547, A29. DOI: 10.1051/0004-6361/201219515.

Binette, L. et al. 2022. *RMxAA*, vol. 58, pp. 133–153. DOI: 10.22201/ia.01851101p.2022.58.01.11.

Binsack, J. H. 1966. PhD thesis. MIT.

Bischetti, M. et al. 2019. *A&A*, vol. 630, A59. DOI: 10.1051/0004-6361/201833557.

Blandford, R. et al. 2019. *ARA&A*, vol. 57, pp. 467–509. DOI: 10.1146/annurev-astro-081817-051948.

Blandford, R. D. and Rees, M. J. 1974. *MNRAS*, vol. 169, pp. 395–415. DOI: 10.1093/mnras/169.3.395.

Blumenthal, G. R. et al. 1984. *Nature*, vol. 311, pp. 517–525. DOI: 10.1038/311517a0.

Bohm, D. and Aller, L. H. 1947. *ApJ*, vol. 105, p. 131. DOI: 10.1086/144890.

Bonzini, M. et al. 2013. *MNRAS*, vol. 436, pp. 3759–3771. DOI: 10.1093/mnras/stt1879.

Borisova, E. et al. 2016. *ApJ*, vol. 831, p. 39. DOI: 10.3847/0004-637X/831/1/39.

Bouché, N. et al. 2016. *ApJ*, vol. 820, p. 121. DOI: 10.3847/0004-637X/820/2/121.

Bower, R. G. et al. 2006. *MNRAS*, vol. 370, pp. 645–655. DOI: 10.1111/j.1365-2966.2006.10519.x.

Bradshaw, S. J. and Raymond, J. 2013. *Space Sci. Rev.*, vol. 178, pp. 271–306. DOI: 10.1007/s11214-013-9970-0.

Bremer, M. N. et al. 1992. *MNRAS*, vol. 258, 23P. DOI: 10.1093/mnras/258.1.23P.

Brown, M. J. I. et al. 2006. *ApJ*, vol. 638, pp. 88–99. DOI: 10.1086/498843.

Brüggen, M. and Kaiser, C. R. 2002. *Nature*, vol. 418, pp. 301–303. DOI: 10.1038/nature00857.

Brusa, M. et al. 2015. *A&A*, vol. 578, A11. DOI: 10.1051/0004-6361/201425491.

Cai, Z. et al. 2017. *ApJ*, vol. 837, p. 71. DOI: 10.3847/1538-4357/aa5d14.

Cai, Z. et al. 2019. *ApJS*, vol. 245, p. 23. DOI: 10.3847/1538-4365/ab4796.

Candini, S. et al. 2023. *A&A*, vol. 677, A4. DOI: 10.1051/0004-6361/202347036.

Cano-Díaz, M. et al. 2012. *A&A*, vol. 537, p. L8. DOI: 10.1051/0004-6361/201118358.

Cantalupo, S. 2017. *Gas Accretion onto Galaxies*. Ed. by A. Fox and R. Davé. Vol. 430, p. 195. DOI: 10.1007/978-3-319-52512-9_9.

Cantalupo, S. et al. 2005. *ApJ*, vol. 628, pp. 61–75. DOI: 10.1086/430758.

Cantalupo, S. et al. 2014. *Nature*, vol. 506, pp. 63–66. DOI: 10.1038/nature12898.

Cappellari, M. and Copin, Y. 2003. *MNRAS*, vol. 342, pp. 345–354. DOI: 10.1046/j.1365-8711.2003.06541.x.

Carswell, R. F. and Ferland, G. J. 1988. *MNRAS*, vol. 235, pp. 1121–1128.

Castignani, G. et al. 2019. *A&A*, vol. 623, A48. DOI: 10.1051/0004-6361/201834066.

Chambers, K. C. et al. 1987. *Nature*, vol. 329, pp. 604–606. DOI: 10.1038/329604a0.

Christensen, L. et al. 2006. *A&A*, vol. 459, pp. 717–729. DOI: 10.1051/0004-6361:20065318.

Cicone, C. et al. 2015. *A&A*, vol. 574, A14. DOI: 10.1051/0004-6361/201424980.

Cicone, C. et al. 2018. *Nature Astronomy*, vol. 2, pp. 176–178. DOI: 10.1038/s41550-018-0406-3.

Cimatti, A. et al. 1998. *A&A*, vol. 329, pp. 399–408. DOI: 10.48550/arXiv.astro-ph/9708204.

Collet, C. et al. 2015. *A&A*, vol. 579, A89. DOI: 10.1051/0004-6361/201424544.

Condon, J. J. et al. 2013. *ApJ*, vol. 768, p. 37. DOI: 10.1088/0004-637X/768/1/37.

Congiu, E. et al. 2017. *MNRAS*, vol. 471, pp. 562–588. DOI: 10.1093/mnras/stx1628.

Cooke, E. A. et al. 2014. *MNRAS*, vol. 440, pp. 3262–3274. DOI: 10.1093/mnras/stu522.

Costa, T. et al. 2018. *MNRAS*, vol. 479, pp. 2079–2111. DOI: 10.1093/mnras/sty1514.

Costa, T. et al. 2022. *MNRAS*, vol. 517, pp. 1767–1790. DOI: 10.1093/mnras/stac2432.

Cresci, G. et al. 2015a. *ApJ*, vol. 799, p. 82. DOI: 10.1088/0004-637X/799/1/82.

Cresci, G. et al. 2015b. *A&A*, vol. 582, A63. DOI: 10.1051/0004-6361/201526581.

Croston, J. H. et al. 2019. *A&A*, vol. 622, A10. DOI: 10.1051/0004-6361/201834019.

Croton, D. J. et al. 2006. *MNRAS*, vol. 365, pp. 11–28. DOI: 10.1111/j.1365-2966.2005.09675.x.

Crumley, P. et al. 2019. *MNRAS*, vol. 485, pp. 5105–5119. DOI: 10.1093/mnras/stz232.

Curti, M. et al. 2017. *MNRAS*, vol. 465, pp. 1384–1400. DOI: 10.1093/mnras/stw2766.

Dabhade, P. et al. 2017. *MNRAS*, vol. 469, pp. 2886–2906. DOI: 10.1093/mnras/stx860.

Daddi, E. et al. 2021. *A&A*, vol. 649, A78. DOI: 10.1051/0004-6361/202038700.

D'Agostino, J. J. et al. 2019. *MNRAS*, vol. 487, pp. 4153–4168. DOI: 10.1093/mnras/stz1611.

D'Amato, Q. et al. 2022. *A&A*, vol. 668, A133. DOI: 10.1051/0004-6361/202244452.

Danovich, M. et al. 2015. *MNRAS*, vol. 449, pp. 2087–2111. DOI: 10.1093/mnras/stv270.

Dasyra, K. M. and Combes, F. 2012. *A&A*, vol. 541, p. L7. DOI: 10.1051/0004-6361/201219229.

Davé, R. et al. 2019. *MNRAS*, vol. 486, pp. 2827–2849. DOI: 10.1093/mnras/stz937.

Davelaar, J. et al. 2019. *A&A*, vol. 632, A2. DOI: 10.1051/0004-6361/201936150.

Davidzon, I. et al. 2017. *A&A*, vol. 605, A70. DOI: 10.1051/0004-6361/201730419.

De Breuck, C. et al. 2000. *A&A*, vol. 362, pp. 519–543. DOI: 10.48550/arXiv.astro-ph/0008264.

De Breuck, C. et al. 2002. *AJ*, vol. 123, pp. 637–677. DOI: 10.1086/324632.

De Breuck, C. et al. 2010. *ApJ*, vol. 725, pp. 36–62. DOI: 10.1088/0004-637X/725/1/36.

Decker, R. B. and Krimigis, S. M. 2003. *Advances in Space Research*, vol. 32, pp. 597–602. DOI: 10.1016/S0273-1177(03)00356-9.

Dekel, A. et al. 2009. *Nature*, vol. 457, pp. 451–454. DOI: 10.1038/nature07648.

Dey, A. et al. 1997. *ApJ*, vol. 490, pp. 698–709. DOI: 10.1086/304911.

Di Matteo, T. et al. 2005. *Nature*, vol. 433, pp. 604–607. DOI: 10.1038/nature03335.

Dialynas, K. et al. 2009. *J. Geophys. Res. Space Phys.*, vol. 114, A01212. DOI: 10.1029/2008JA013761.

Diaz, A. I. et al. 1988. *A&A*, vol. 195, pp. 53–59.

Dickey, C. M. et al. 2019. *ApJ*, vol. 884, p. 180. DOI: 10.3847/1538-4357/ab3220.

Dijkstra, M. 2014. *PASA*, vol. 31, e040. DOI: 10.1017/pasa.2014.33.

Dijkstra, M. 2017, arXiv:1704.03416. DOI: 10.48550/arXiv.1704.03416.

Dijkstra, M. and Loeb, A. 2008. *MNRAS*, vol. 386, pp. 492–504. DOI: 10.1111/j.1365-2966.2008.13066.x.

Dijkstra, M. and Loeb, A. 2009. *MNRAS*, vol. 400, pp. 1109–1120. DOI: 10.1111/j.1365-2966.2009.15533.x.

Dijkstra, M. et al. 2006. *ApJ*, vol. 649, pp. 14–36. DOI: 10.1086/506243.

Dopita, M. A. and Sutherland, R. S. 2000. *ApJ*, vol. 539, pp. 742–750. DOI: 10.1086/309241.

Dopita, M. A. et al. 2002. *ApJ*, vol. 572, pp. 753–761. DOI: 10.1086/340429.

Dopita, M. A. et al. 2013. *ApJS*, vol. 208, p. 10. DOI: 10.1088/0067-0049/208/1/10.

Dopita, M. A. et al. 2014. *A&A*, vol. 566, A41. DOI: 10.1051/0004-6361/201423467.

Dors, O. L. et al. 2015. *MNRAS*, vol. 453, pp. 4102–4111. DOI: 10.1093/mnras/stv1916.

Dors, O. L. et al. 2018. *MNRAS*, vol. 479, pp. 2294–2307. DOI: 10.1093/mnras/sty1658.

Dors, O. L. et al. 2020. *MNRAS*, vol. 492, pp. 468–479. DOI: 10.1093/mnras/stz3492.

Draine, B. T. and Kreisch, C. D. 2018. *ApJ*, vol. 862, p. 30. DOI: 10.3847/1538-4357/aac891.

Drouart, G. et al. 2014. *A&A*, vol. 566, A53. DOI: 10.1051/0004-6361/201323310.

Drouart, G. et al. 2016. *A&A*, vol. 593, A109. DOI: 10.1051/0004-6361/201526880.

Dudík, J. et al. 2017. *Sol. Phys.*, vol. 292, p. 100. DOI: 10.1007/s11207-017-1125-0.

Dunlop, J. S. et al. 2003. *MNRAS*, vol. 340, pp. 1095–1135. DOI: 10.1046/j.1365-8711.2003.06333.x.

Duras, F. et al. 2017. *A&A*, vol. 604, A67. DOI: 10.1051/0004-6361/201731052.

Eales, S. A. et al. 1993. *ApJ*, vol. 409, p. 578. DOI: 10.1086/172688.

Emonts, B. H. C. et al. 2016. *Science*, vol. 354, pp. 1128–1130. DOI: 10.1126/science.aag0512.

Emonts, B. H. C. et al. 2023. *Science*, vol. 379, pp. 1323–1326. DOI: 10.1126/science.abh2150.

Ergun, R. E. et al. 2020. *ApJ*, vol. 898, p. 153. DOI: 10.3847/1538-4357/ab9ab5.

Espinoza, C. M. et al. 2018. *Geophysics Research Letters*, vol. 45, pp. 6362–6370. DOI: 10.1029/2018GL078631.

Fabian, A. C. 1994. *ARA&A*, vol. 32, pp. 277–318. DOI: 10.1146/annurev.aa.32.090194.001425.

Fabian, A. C. 2012. *ARA&A*, vol. 50, pp. 455–489. DOI: 10.1146/annurev-astro-081811-125521.

Falkendal, T. et al. 2019. *A&A*, vol. 621, A27. DOI: 10.1051/0004-6361/201732485.

Fanaroff, B. et al. 2021. *MNRAS*, vol. 505, pp. 6003–6016. DOI: 10.1093/mnras/stab1540.

Fanaroff, B. L. and Riley, J. M. 1974. *MNRAS*, vol. 167, 31P–36P. DOI: 10.1093/mnras/167.1.31P.

Fardal, M. A. et al. 2001. *ApJ*, vol. 562, pp. 605–617. DOI: 10.1086/323519.

Farina, E. P. et al. 2019. *ApJ*, vol. 887, p. 196. DOI: 10.3847/1538-4357/ab5847.

Feltre, A. et al. 2016. *MNRAS*, vol. 456, pp. 3354–3374. DOI: 10.1093/mnras/stv2794.

Ferland, G. J. and Netzer, H. 1983. *ApJ*, vol. 264, pp. 105–113. DOI: 10.1086/160577.

Ferland, G. J. et al. 1998. *PASP*, vol. 110, pp. 761–778. DOI: 10.1086/316190.

Ferland, G. J. et al. 2009. *MNRAS*, vol. 392, pp. 1475–1502. DOI: 10.1111/j.1365-2966.2008.14153.x.

Ferland, G. J. et al. 2016. *RMxAA*, vol. 52, p. 261. DOI: 10.48550/arXiv.1605.03634.

Ferrarese, L. and Ford, H. 2005. *Space Sci. Rev*, vol. 116, pp. 523–624. DOI: 10.1007/s11214-005-3947-6.

Ferrarese, L. and Merritt, D. 2000. *ApJ*, vol. 539, pp. L9–L12. DOI: 10.1086/312838.

Ferruit, P. et al. 1997. *A&A*, vol. 322, pp. 73–85.

Field, G. B. et al. 1969. *ApJ*, vol. 155, p. L149. DOI: 10.1086/180324.

Fluetsch, A. et al. 2019. *MNRAS*, vol. 483, pp. 4586–4614. DOI: 10.1093/mnras/sty3449.

Förster Schreiber, N. M. and Wuyts, S. 2020. *ARA&A*, vol. 58, pp. 661–725. DOI: 10.1146/annurev-astro-032620-021910.

Fossati, M. et al. 2021. *MNRAS*, vol. 503, pp. 3044–3064. DOI: 10.1093/mnras/stab660.

Fu, H. and Stockton, A. 2008. *ApJ*, vol. 677, pp. 79–91. DOI: 10.1086/529015.

Fumagalli, M. et al. 2014. *ApJ*, vol. 780, p. 74. DOI: 10.1088/0004-637X/780/1/74.

Furlanetto, S. R. et al. 2005. *ApJ*, vol. 622, pp. 7–27. DOI: 10.1086/426808.

Fynbo, J. P. U. et al. 2003. *A&A*, vol. 407, pp. 147–157. DOI: 10.1051/0004-6361:20030840.

Fynbo, J. U. et al. 1999. *MNRAS*, vol. 305, pp. 849–858. DOI: 10.1046/j.1365-8711.1999.02520.x.

Galametz, A. et al. 2010. *A&A*, vol. 522, A58. DOI: 10.1051/0004-6361/201015035.

Galametz, A. et al. 2012. *ApJ*, vol. 749, p. 169. DOI: 10.1088/0004-637X/749/2/169.

Gallagher, R. et al. 2019. *MNRAS*, vol. 485, pp. 3409–3429. DOI: 10.1093/mnras/stz564.

García-Rojas, J. and Esteban, C. 2007. *ApJ*, vol. 670, pp. 457–470. DOI: 10.1086/521871.

García-Rojas, J. et al. 2019. *arXiv e-prints*, arXiv:1904.06763. DOI: 10.48550/arXiv.1904.06763.

Gardner, J. P. et al. 2006. *Space Sci. Rev*, vol. 123, pp. 485–606. DOI: 10.1007/s11214-006-8315-7.

Geach, J. E. et al. 2009. *ApJ*, vol. 700, pp. 1–9. DOI: 10.1088/0004-637X/700/1/1.

Gebhardt, K. et al. 2000. *ApJ*, vol. 539, pp. L13–L16. DOI: 10.1086/312840.

Gendre, M. A. et al. 2010. *MNRAS*, vol. 404, pp. 1719–1732. DOI: 10.1111/j.1365-2966.2010.16413.x.

Gendre, M. A. et al. 2013. *MNRAS*, vol. 430, pp. 3086–3101. DOI: 10.1093/mnras/stt116.

Georganopoulos, M. and Kazanas, D. 2003. *ApJ*, vol. 589, pp. L5–L8. DOI: 10.1086/375796.

Ghisellini, G. and Celotti, A. 2001. *A&A*, vol. 379, pp. L1–L4. DOI: 10.1051/0004-6361:20011338.

Giammanco, C. and Beckman, J. E. 2005. *A&A*, vol. 437, pp. L11–L14. DOI: 10.1051/0004-6361:200500129.

Giavalisco, M. et al. 2011. *ApJ*, vol. 743, p. 95. DOI: 10.1088/0004-637X/743/1/95.

Girdhar, A. et al. 2022. *MNRAS*, vol. 512, pp. 1608–1628. DOI: 10.1093/mnras/stac073.

Gloeckler, G. et al. 1992. *A&AS*, vol. 92, pp. 267–289.

Grevesse, N. et al. 2010. *Ap&SS*, vol. 328, pp. 179–183. DOI: 10.1007/s10509-010-0288-z.

Groves, B. A. et al. 2004. *ApJS*, vol. 153, pp. 9–73. DOI: 10.1086/421113.

Guo, Y. et al. 2020. *ApJ*, vol. 898, p. 26. DOI: 10.3847/1538-4357/ab9b7f.

Hada, K. et al. 2013. *ApJ*, vol. 779, p. 6. DOI: 10.1088/0004-637X/779/1/6.

Hagihara, Y. 1939a. *Japanese Journal of Astronomy and Geophysics*, vol. 17, p. 199.

Hagihara, Y. 1939b. *Japanese Journal of Astronomy and Geophysics*, vol. 17, p. 417.

Haiman, Z. and Rees, M. J. 2001. *ApJ*, vol. 556, pp. 87–92. DOI: 10.1086/321567.

Haiman, Z. et al. 2000. *ApJ*, vol. 537, pp. L5–L8. DOI: 10.1086/312754.

Hamann, F. and Ferland, G. 1992. *ApJ*, vol. 391, p. L53. DOI: 10.1086/186397.

Hamann, F. and Ferland, G. 1993. *ApJ*, vol. 418, p. 11. DOI: 10.1086/173366.

Hani, M. H. et al. 2018. *MNRAS*, vol. 475, pp. 1160–1176. DOI: 10.1093/mnras/stx3252.

Hardcastle, M. J. and Croston, J. H. 2020. *New Astron. Rev.*, vol. 88, p. 101539. DOI: 10.1016/j.newar.2020.101539.

Häring, N. and Rix, H.-W. 2004. *ApJ*, vol. 604, pp. L89–L92. DOI: 10.1086/383567.

Harrington, J. P. 1968. *ApJ*, vol. 152, p. 943. DOI: 10.1086/149608.

Harrison, C. M. 2017. *Nature Astronomy*, vol. 1, p. 0165. DOI: 10.1038/s41550-017-0165.

Harrison, C. M. et al. 2014. *MNRAS*, vol. 441, pp. 3306–3347. DOI: 10.1093/mnras/stu515.

Harrison, C. M. et al. 2018. *Nature Astronomy*, vol. 2, pp. 198–205. DOI: 10.1038/s41550-018-0403-6.

Hashimoto, T. et al. 2011. *PASJ*, vol. 63, p. L7. DOI: 10.1093/pasj/63.1.L7.

Hasinger, G. et al. 2005. *A&A*, vol. 441, pp. 417–434. DOI: 10.1051/0004-6361:20042134.

Hatch, N. A. et al. 2008. *MNRAS*, vol. 383, pp. 931–942. DOI: 10.1111/j.1365-2966.2007.12626.x.

Hatch, N. A. et al. 2014. *MNRAS*, vol. 445, pp. 280–289. DOI: 10.1093/mnras/stu1725.

Hayashi, M. et al. 2012. *ApJ*, vol. 757, p. 15. DOI: 10.1088/0004-637X/757/1/15.

Hayes, M. et al. 2011. *Nature*, vol. 476, pp. 304–307. DOI: 10.1038/nature10320.

Hebb, M. H. and Menzel, D. H. 1940. *ApJ*, vol. 92, p. 408. DOI: 10.1086/144230.

Heckman, T. M. and Best, P. N. 2014. *ARA&A*, vol. 52, pp. 589–660. DOI: 10.1146/annurev-astro-081913-035722.

Heckman, T. M. et al. 1991. *ApJ*, vol. 381, p. 373. DOI: 10.1086/170660.

Heerikhuisen, J. et al. 2008. *ApJ*, vol. 682, pp. 679–689. DOI: 10.1086/588248.

Hennawi, J. F. et al. 2015. *Science*, vol. 348, pp. 779–783. DOI: 10.1126/science.aaa5397.

Henry, R. B. C. et al. 2000. *ApJ*, vol. 541, pp. 660–674. DOI: 10.1086/309471.

Hernán-Caballero, A. et al. 2014. *MNRAS*, vol. 443, pp. 3538–3549. DOI: 10.1093/mnras/stu1413.

Herrera-Camus, R. et al. 2019. *ApJ*, vol. 871, p. 37. DOI: 10.3847/1538-4357/aaf6a7.

Herrera-Camus, R. et al. 2020. *A&A*, vol. 635, A47. DOI: 10.1051/0004-6361/201936434.

Herrera Ruiz, N. et al. 2016. *A&A*, vol. 589, p. L2. DOI: 10.1051/0004-6361/201628302.

Hickox, R. C. et al. 2009. *ApJ*, vol. 696, pp. 891–919. DOI: 10.1088/0004-637X/696/1/891.

Ho, L. C. 2002. *ApJ*, vol. 564, pp. 120–132. DOI: 10.1086/324399.

Ho, L. C. 2008. *ARA&A*, vol. 46, pp. 475–539. DOI: 10.1146/annurev.astro.45.051806.110546.

Holt, J. et al. 2009. *MNRAS*, vol. 400, pp. 589–602. DOI: 10.1111/j.1365-2966.2009.15491.x.

Hönig, S. F. 2019. *ApJ*, vol. 884, p. 171. DOI: 10.3847/1538-4357/ab4591.

Hönig, S. F. and Kishimoto, M. 2017. *ApJ*, vol. 838, p. L20. DOI: 10.3847/2041-8213/aa6838.

Hopkins, A. M. and Beacom, J. F. 2006. *ApJ*, vol. 651, pp. 142–154. DOI: 10.1086/506610.

Hopkins, P. F. and Elvis, M. 2010. *MNRAS*, vol. 401, pp. 7–14. DOI: 10.1111/j.1365-2966.2009.15643.x.

Hopkins, P. F. et al. 2006. *ApJS*, vol. 163, pp. 1–49. DOI: 10.1086/499298.

Hopkins, P. F. et al. 2008. *ApJS*, vol. 175, pp. 356–389. DOI: 10.1086/524362.

Huang, J. et al. 2023. *MNRAS*, vol. 525, pp. 5702–5718. DOI: 10.1093/mnras/stad2642.

Humphrey, A. 2019. *MNRAS*. DOI: 10.1093/mnras/stz687.

Humphrey, A. and Binette, L. 2014. *MNRAS*, vol. 442, pp. 753–758. DOI: 10.1093/mnras/stu723.

Humphrey, A. et al. 2006. *MNRAS*, vol. 369, pp. 1103–1114. DOI: 10.1111/j.1365-2966.2006.10224.x.

Humphrey, A. et al. 2007. *MNRAS*, vol. 375, pp. 705–714. DOI: 10.1111/j.1365-2966.2006.11344.x.

Humphrey, A. et al. 2008a. *MNRAS*, vol. 383, pp. 11–40. DOI: 10.1111/j.1365-2966.2007.12506.x.

Humphrey, A. et al. 2008b. *MNRAS*, vol. 390, pp. 1505–1516. DOI: 10.1111/j.1365-2966.2008.13826.x.

Humphrey, A. et al. 2010. *MNRAS*, vol. 408, pp. L1–L5. DOI: 10.1111/j.1745-3933.2010.00906.x.

Humphrey, A. et al. 2011. *MNRAS*, vol. 418, pp. 74–89. DOI: 10.1111/j.1365-2966.2011.19437.x.

Humphrey, A. et al. 2013a. *MNRAS*, vol. 428, pp. 563–572. DOI: 10.1093/mnras/sts055.

Humphrey, A. et al. 2013b. *ApJ*, vol. 768, p. L3. DOI: 10.1088/2041-8205/768/1/L3.

Humphrey, A. et al. 2019. *A&A*, vol. 621, A10. DOI: 10.1051/0004-6361/201732007.

Husband, K. et al. 2016. *MNRAS*, vol. 462, pp. 421–428. DOI: 10.1093/mnras/stw1520.

Husemann, B. and Harrison, C. M. 2018. *Nature Astronomy*, vol. 2, pp. 196–197. DOI: 10.1038/s41550-018-0407-2.

Ivezić, Ž. et al. 2002. *AJ*, vol. 124, pp. 2364–2400. DOI: 10.1086/344069.

Izotov, Y. I. et al. 2006. *A&A*, vol. 448, pp. 955–970. DOI: 10.1051/0004-6361:20053763.

Jakobsen, P. et al. 2022. *A&A*, vol. 661, A80. DOI: 10.1051/0004-6361/202142663.

Jarvis, M. E. et al. 2019. *MNRAS*, vol. 485, pp. 2710–2730. DOI: 10.1093/mnras/stz556.

Jarvis, M. J. et al. 2003. *MNRAS*, vol. 338, pp. 263–272. DOI: 10.1046/j.1365-8711.2003.06053.x.

Jo, J. U. et al. 2021. *Ap&SS*, vol. 366, p. 18. DOI: 10.1007/s10509-021-03925-7.

Jones, M. L. et al. 2019. *ApJ*, vol. 881, p. 110. DOI: 10.3847/1538-4357/ab2d9f.

Jones, M. et al. 2004. *An Introduction to Galaxies and Cosmology*. 2nd edn. (Cambridge Univ. Press).

Jurac, S. et al. 2002. *GeoRL*, vol. 29, p. 2172. DOI: 10.1029/2002GL015855.

Kakkad, D. et al. 2018. *A&A*, vol. 618, A6. DOI: 10.1051/0004-6361/201832790.

Kaler, J. B. 1986. *ApJ*, vol. 308, p. 322. DOI: 10.1086/164503.

Karouzos, M. et al. 2016. *ApJ*, vol. 833, p. 171. DOI: 10.3847/1538-4357/833/2/171.

Kauffmann, G. et al. 2003. *MNRAS*, vol. 346, pp. 1055–1077. DOI: 10.1111/j.1365-2966.2003.07154.x.

Kellermann, K. I. et al. 1989. *AJ*, vol. 98, p. 1195. DOI: 10.1086/115207.

Kewley, L. J. and Dopita, M. A. 2002. *ApJS*, vol. 142, pp. 35–52. DOI: 10.1086/341326.

Kewley, L. J. et al. 2001. *ApJ*, vol. 556, pp. 121–140. DOI: 10.1086/321545.

Kim, E. et al. 2020. *ApJ*, vol. 894, p. 33. DOI: 10.3847/1538-4357/ab837f.

King, A. 2003. *ApJ*, vol. 596, pp. L27–L29. DOI: 10.1086/379143.

King, A. and Pounds, K. 2015. *ARA&A*, vol. 53, pp. 115–154. DOI: 10.1146/annurev-astro-082214-122316.

Kirpichev, I. P. et al. 2021. *J. Geophys. Res. Space Phys.*, vol. 126, e29409. DOI: 10.1029/2021JA029409.

Klamer, I. J. et al. 2004. *ApJ*, vol. 612, pp. L97–L100. DOI: 10.1086/424843.

Kolwa, S. et al. 2023. *MNRAS*, vol. 525, pp. 5831–5845. DOI: 10.1093/mnras/stad2647.

Kormendy, J. and Ho, L. C. 2013. *ARA&A*, vol. 51, pp. 511–653. DOI: 10.1146/annurev-astro-082708-101811.

Kormendy, J. and Richstone, D. 1995. *ARA&A*, vol. 33, p. 581. DOI: 10.1146/annurev.aa.33.090195.003053.

Koutsouridou, I. and Cattaneo, A. 2022. *MNRAS*, vol. 516, pp. 4194–4211. DOI: 10.1093/mnras/stac2240.

Kraemer, S. B. et al. 1998. *ApJ*, vol. 508, pp. 232–242. DOI: 10.1086/306389.

Langer, W. D. and Pineda, J. L. 2015. *A&A*, vol. 580, A5. DOI: 10.1051/0004-6361/201525950.

Laor, A. and Draine, B. T. 1993. *ApJ*, vol. 402, p. 441. DOI: 10.1086/172149.

Le Fèvre, O. et al. 2019. *A&A*, vol. 625, A51. DOI: 10.1051/0004-6361/201732197.

Lee, J. and Yi, S. K. 2013. *ApJ*, vol. 766, p. 38. DOI: 10.1088/0004-637X/766/1/38.

Lee, J. and Yi, S. K. 2017. *ApJ*, vol. 836, p. 161. DOI: 10.3847/1538-4357/aa5b87.

Leubner, M. P. 2002. *Ap&SS*, vol. 282, pp. 573–579. DOI: 10.1023/A:1020990413487.

Li, Y.-P. et al. 2018. *ApJ*, vol. 866, p. 70. DOI: 10.3847/1538-4357/aade8b.

Li, Z. et al. 2022. *MNRAS*, vol. 513, pp. 3414–3428. DOI: 10.1093/mnras/stac958.

Lin, B.-Z. and Zhang, Y. 2020. *ApJ*, vol. 899, p. 33. DOI: 10.3847/1538-4357/ab9d7e.

Liu, G. et al. 2013. *MNRAS*, vol. 436, pp. 2576–2597. DOI: 10.1093/mnras/stt1755.

Liu, X. W. et al. 2001. *MNRAS*, vol. 327, pp. 141–168. DOI: 10.1046/j.1365-8711.2001.04676.x.

Livadiotis, G. 2018. *Nonlinear Processes in Geophysics*, vol. 25, pp. 77–88. DOI: 10.5194/npg-25-77-2018.

Livadiotis, G. and McComas, D. J. 2009. *J. Geophys. Res. Space Phys.*, vol. 114, A11105. DOI: 10.1029/2009JA014352.

Livadiotis, G. and McComas, D. J. 2022. *ApJ*, vol. 940, p. 83. DOI: 10.3847/1538-4357/ac99df.

Longair, M. S. et al. 1973. *MNRAS*, vol. 164, p. 243. DOI: 10.1093/mnras/164.3.243.

Lusso, E. et al. 2019. *MNRAS*, vol. 485, pp. L62–L67. DOI: 10.1093/mnrasl/slz032.

Lyman, T. 1906. *ApJ*, vol. 23, p. 181. DOI: 10.1086/141330.

Mackenzie, R. et al. 2021. *MNRAS*, vol. 502, pp. 494–509. DOI: 10.1093/mnras/staa3277.

Madau, P. and Dickinson, M. 2014. *ARA&A*, vol. 52, pp. 415–486. DOI: 10.1146/annurev-astro-081811-125615.

Maiolino, R. and Mannucci, F. 2019. *A&A Rev.*, vol. 27, p. 3. DOI: 10.1007/s00159-018-0112-2.

Maiolino, R. et al. 2012. *MNRAS*, vol. 425, pp. L66–L70. DOI: 10.1111/j.1745-3933.2012.01303.x.

Maiolino, R. et al. 2017. *Nature*, vol. 544, pp. 202–206. DOI: 10.1038/nature21677.

Maksimovic, M. et al. 1997. *A&A*, vol. 324, pp. 725–734.

Manzano-King, C. M. et al. 2019. *ApJ*, vol. 884, p. 54. DOI: 10.3847/1538-4357/ab4197.

Marconi, A. and Hunt, L. K. 2003. *ApJ*, vol. 589, pp. L21–L24. DOI: 10.1086/375804.

Marques-Chaves, R. et al. 2019. *A&A*, vol. 629, A23. DOI: 10.1051/0004-6361/201936013.

Martin, D. C. et al. 2015. *Nature*, vol. 524, pp. 192–195. DOI: 10.1038/nature14616.

Martizzi, D. et al. 2019. *MNRAS*, vol. 486, pp. 3766–3787. DOI: 10.1093/mnras/stz1106.

Mathews, W. G. and Ferland, G. J. 1987. *ApJ*, vol. 323, p. 456. DOI: 10.1086/165843.

Matsuda, Y. et al. 2004. *AJ*, vol. 128, pp. 569–584. DOI: 10.1086/422020.

Matsuoka, K. et al. 2009. *A&A*, vol. 503, pp. 721–730. DOI: 10.1051/0004-6361/200811478.

Matsuoka, K. et al. 2018. *A&A*, vol. 616, p. L4. DOI: 10.1051/0004-6361/201833418.

Matthews, T. A. et al. 1964. *ApJ*, vol. 140, p. 35. DOI: 10.1086/147890.

Matzeu, G. A. et al. 2023. *A&A*, vol. 670, A182. DOI: 10.1051/0004-6361/202245036.

McCarthy, P. J. 1993. *ARA&A*, vol. 31, pp. 639–688. DOI: 10.1146/annurev.aa.31.090193.003231.

McCarthy, P. J. et al. 1987a. *ApJ*, vol. 321, pp. L29–L33. DOI: 10.1086/185000.

McCarthy, P. J. et al. 1987b. *ApJ*, vol. 319, p. L39. DOI: 10.1086/184951.

McCarthy, P. J. et al. 1990. *ApJ*, vol. 365, pp. 487–501. DOI: 10.1086/169503.

McKee, C. F. and Ostriker, J. P. 1977. *ApJ*, vol. 218, pp. 148–169. DOI: 10.1086/155667.

McLure, R. J. et al. 2004. *MNRAS*, vol. 351, pp. 347–361. DOI: 10.1111/j.1365-2966.2004.07793.x.

Mendoza, C. and Bautista, M. A. 2014. *ApJ*, vol. 785, p. 91. DOI: 10.1088/0004-637X/785/2/91.

Mickaelian, A. M. et al. 2021. *Front. Astron. Space Sci.*, vol. 7, p. 82. DOI: 10.3389/fspas.2020.505043.

Mignoli, M. et al. 2019. *A&A*, vol. 626, A9. DOI: 10.1051/0004-6361/201935062.

Miley, G. and De Breuck, C. 2008. *A&A Rev.*, vol. 15, pp. 67–144. DOI: 10.1007/s00159-007-0008-z.

Miley, G. K. et al. 2006. *ApJ*, vol. 650, pp. L29–L32. DOI: 10.1086/508534.

Miller, L. et al. 1990. *MNRAS*, vol. 244, pp. 207–213.

Miller, P. et al. 1993. *MNRAS*, vol. 263, pp. 425–460. DOI: 10.1093/mnras/263.2.425.

Mingo, B. et al. 2014. *MNRAS*, vol. 440, pp. 269–297. DOI: 10.1093/mnras/stu263.

Mingo, B. et al. 2019. *MNRAS*, vol. 488, pp. 2701–2721. DOI: 10.1093/mnras/stz1901.

Mitchell, P. D. et al. 2021. *MNRAS*, vol. 501, pp. 5757–5775. DOI: 10.1093/mnras/stab035.

Mo, H. et al. 2010. Cambridge University Press. DOI: 10.1017/CBO9780511807244.

Moe, M. et al. 2009. *ApJ*, vol. 706, pp. 525–534. DOI: 10.1088/0004-637X/706/1/525.

Molina, J. et al. 2022. *ApJ*, vol. 935, p. 72. DOI: 10.3847/1538-4357/ac7d4d.

Moncuquet, M. et al. 2002. *J. Geophys. Res.*, vol. 107, p. 1260. DOI: 10.1029/2001JA900124.

Moncuquet, M. et al. 2020. *ApJS*, vol. 246, p. 44. DOI: 10.3847/1538-4365/ab5a84.

Morais, S. G. et al. 2017. *MNRAS*, vol. 465, pp. 2698–2713. DOI: 10.1093/mnras/stw2926.

Morganti, R. et al. 2013. *Science*, vol. 341, pp. 1082–1085. DOI: 10.1126/science.1240436.

Morganti, R. et al. 2015. *A&A*, vol. 580, A1. DOI: 10.1051/0004-6361/201525860.

Mori, M. et al. 2004. *ApJ*, vol. 613, pp. L97–L100. DOI: 10.1086/425255.

Moster, B. P. et al. 2013. *MNRAS*, vol. 428, pp. 3121–3138. DOI: 10.1093/mnras/sts261.

Moy, E. and Rocca-Volmerange, B. 2002. *A&A*, vol. 383, pp. 46–55. DOI: 10.1051/0004-6361:20011727.

Mukherjee, D. et al. 2016. *MNRAS*, vol. 461, pp. 967–983. DOI: 10.1093/mnras/stw1368.

Mullin, L. M. et al. 2008. *MNRAS*, vol. 390, pp. 595–621. DOI: 10.1111/j.1365-2966.2008.13534.x.

Nagao, T. et al. 2003. *AJ*, vol. 125, pp. 1729–1735. DOI: 10.1086/368248.

Nagao, T. et al. 2006. *A&A*, vol. 447, pp. 863–876. DOI: 10.1051/0004-6361:20054127.

Natarajan, P. and Treister, E. 2009. *MNRAS*, vol. 393, pp. 838–845. DOI: 10.1111/j.1365-2966.2008.13864.x.

Nesvadba, N. P. H. et al. 2017a. *A&A*, vol. 600, A121. DOI: 10.1051/0004-6361/201629357.

Nesvadba, N. P. H. et al. 2017b. *A&A*, vol. 599, A123. DOI: 10.1051/0004-6361/201528040.

Netzer, H. 2013. *The Physics and Evolution of Active Galactic Nuclei*. Cambridge University Press.

Netzer, H. 2015. *ARA&A*, vol. 53, pp. 365–408. DOI: 10.1146/annurev-astro-082214-122302.

Netzer, H. 2022. *MNRAS*, vol. 509, pp. 2637–2646. DOI: 10.1093/mnras/stab3133.

Neufeld, D. A. 1990. *ApJ*, vol. 350, p. 216. DOI: 10.1086/168375.

Nicholls, D. C. et al. 2012. *ApJ*, vol. 752, p. 148. DOI: 10.1088/0004-637X/752/2/148.

Nicholls, D. C. et al. 2013. *ApJS*, vol. 207, p. 21. DOI: 10.1088/0067-0049/207/2/21.

Ogasawara, K. et al. 2013. *J. Geophys. Res. Space Phys.*, vol. 118, pp. 3126–3137. DOI: 10.1002/jgra.50353.

Ogawa, S. et al. 2021. *ApJ*, vol. 906, p. 84. DOI: 10.3847/1538-4357/abccce.

Ohyama, Y. and Taniguchi, Y. 2004. *AJ*, vol. 127, pp. 1313–1317. DOI: 10.1086/382106.

Oka, M. et al. 2018. *Space Sci. Rev*, vol. 214, p. 82. DOI: 10.1007/s11214-018-0515-4.

Olbert, S. 1968. *Physics of the Magnetosphere*. Ed. by R. L. Carovillano et al. Springer Netherlands: Dordrecht, pp. 641–659.

Osterbrock, D. E. 1962. *ApJ*, vol. 135, p. 195. DOI: 10.1086/147258.

Osterbrock, D. E. 1977. *ApJ*, vol. 215, pp. 733–745. DOI: 10.1086/155407.

Osterbrock, D. E. 1981. *ApJ*, vol. 249, pp. 462–470. DOI: 10.1086/159306.

Osterbrock, D. 1989. *Astrophysics of Gaseous Nebulae and Active Galactic Nuclei*. University Science Books.

Osterbrock, D. and Ferland, G. 2006. *Astrophysics of gaseous nebulae and active galactic nuclei*. University Science Books.

Overzier, R. A. 2016. *A&A Rev.*, vol. 24, p. 14. DOI: 10.1007/s00159-016-0100-3.

Overzier, R. A. et al. 2008. *ApJ*, vol. 673, pp. 143–162. DOI: 10.1086/524342.

Overzier, R. A. et al. 2013. *ApJ*, vol. 771, p. 89. DOI: 10.1088/0004-637X/771/2/89.

Padovani, P. 2016. *A&A Rev.*, vol. 24, p. 13. DOI: 10.1007/s00159-016-0098-6.

Padovani, P. et al. 2017. *A&A Rev.*, vol. 25, p. 2. DOI: 10.1007/s00159-017-0102-9.

Pan, Z. et al. 2022. *ApJ*, vol. 928, p. 172. DOI: 10.3847/1538-4357/ac5aab.

Partridge, R. B. and Peebles, P. J. E. 1967. *ApJ*, vol. 147, p. 868. DOI: 10.1086/149079.

Peimbert, M. 1967. *ApJ*, vol. 150, p. 825. DOI: 10.1086/149385.

Peimbert, M. et al. 2017. *PASP*, vol. 129, p. 082001. DOI: 10.1088/1538-3873/aa72c3.

Pentericci, L. et al. 1999. *A&A*, vol. 341, pp. 329–347. DOI: 10.48550/arXiv.astro-ph/9809056.

Pentericci, L. et al. 2000. *A&A*, vol. 361, pp. L25–L28. DOI: 10.48550/arXiv.astro-ph/0008143.

Pentericci, L. et al. 2001. *ApJS*, vol. 135, pp. 63–85. DOI: 10.1086/321781.

Pérez-Montero, E. et al. 2019. *MNRAS*, vol. 489, pp. 2652–2668. DOI: 10.1093/mnras/stz2278.

Perger, K. et al. 2019. *MNRAS*, vol. 490, pp. 2542–2549. DOI: 10.1093/mnras/stz2723.

Perna, M. et al. 2015. *A&A*, vol. 583, A72. DOI: 10.1051/0004-6361/201526907.

Perna, M. et al. 2023. *arXiv e-prints*, arXiv:2310.03067. DOI: 10.48550/arXiv.2310.03067.

Peterson, B. M. 2006. *Physics of Active Galactic Nuclei at all Scales*. Ed. by D. Alloin. Vol. 693, p. 77. DOI: 10.1007/3-540-34621-X_3.

Petrini, D. and da Silva, E. P. 1997. *A&A*, vol. 317, pp. 262–264.

Pierrard, V. and Pieters, M. 2014. *J. Geophys. Res. Space Phys.*, vol. 119, pp. 9441–9455. DOI: 10.1002/2014JA020678.

Podigachoski, P. et al. 2015. *A&A*, vol. 575, A80. DOI: 10.1051/0004-6361/201425137.

Radcliffe, J. F. et al. 2021. *A&A*, vol. 649, p. L9. DOI: 10.1051/0004-6361/202140791.

Radomski, J. T. et al. 2003. *ApJ*, vol. 587, pp. 117–122. DOI: 10.1086/367612.

Radovich, M. et al. 1998. *Astronomische Nachrichten*, vol. 319, pp. 325–346. DOI: 10.1002/asna.2123190602.

Raymond, J. C. et al. 2010. *ApJ*, vol. 712, pp. 901–907. DOI: 10.1088/0004-637X/712/2/901.

Rees, M. J. 1988. *MNRAS*, vol. 231, 91P–95. DOI: 10.1093/mnras/231.1.91P.

Retana-Montenegro, E. 2022. *A&A*, vol. 663, A153. DOI: 10.1051/0004-6361/202039750.

Reuland, M. et al. 2003. *ApJ*, vol. 592, pp. 755–766. DOI: 10.1086/375619.

Reuland, M. et al. 2004. *MNRAS*, vol. 353, pp. 377–390. DOI: 10.1111/j.1365-2966.2004.08063.x.

Reuland, M. et al. 2007. *AJ*, vol. 133, pp. 2607–2623. DOI: 10.1086/516571.

Revalski, M. et al. 2021. *ApJ*, vol. 910, p. 139. DOI: 10.3847/1538-4357/abdcad.

Reyes, R. et al. 2008. *AJ*, vol. 136, pp. 2373–2390. DOI: 10.1088/0004-6256/136/6/2373.

Ricci, T. V. et al. 2014. *MNRAS*, vol. 440, pp. 2442–2456. DOI: 10.1093/mnras/stu442.

Richards, G. T. et al. 2006. *AJ*, vol. 131, pp. 2766–2787. DOI: 10.1086/503559.

Richardson, C. T. et al. 2014. *MNRAS*, vol. 437, pp. 2376–2403. DOI: 10.1093/mnras/stt2056.

Rickards Vaught, R. J. et al. 2023. *arXiv e-prints*, arXiv:2309.17440. DOI: 10.48550/arXiv.2309.17440.

Riechers, D. A. et al. 2008. *ApJ*, vol. 686, p. L9. DOI: 10.1086/592834.

Riess, A. G. et al. 1998. *AJ*, vol. 116, pp. 1009–1038. DOI: 10.1086/300499.

Rigby, E. E. et al. 2015. *A&A*, vol. 581, A96. DOI: 10.1051/0004-6361/201526475.

Rigby, J. et al. 2023. *PASP*, vol. 135, p. 048001. DOI: 10.1088/1538-3873/acb293.

Robinson, A. et al. 1987. *MNRAS*, vol. 227, pp. 97–114. DOI: 10.1093/mnras/227.1.97.

Rocca-Volmerange, B. et al. 2004. *A&A*, vol. 415, pp. 931–940. DOI: 10.1051/0004-6361:20031717.

Rosdahl, J. and Blaizot, J. 2012. *MNRAS*, vol. 423, pp. 344–366. DOI: 10.1111/j.1365-2966.2012.20883.x.

Rosito, M. S. et al. 2021. *A&A*, vol. 652, A44. DOI: 10.1051/0004-6361/202039976.

Ross, N. P. et al. 2015. *MNRAS*, vol. 453, pp. 3932–3952. DOI: 10.1093/mnras/stv1710.

Röttgering, H. J. A. et al. 1994. *A&AS*, vol. 108, pp. 79–141.

Runnoe, J. C. et al. 2012. *MNRAS*, vol. 426, pp. 2677–2688. DOI: 10.1111/j.1365-2966.2012.21644.x.

Salvestrini, F. et al. 2022. *A&A*, vol. 663, A28. DOI: 10.1051/0004-6361/202142760.

Sandage, A. 1965. *ApJ*, vol. 141, p. 1560. DOI: 10.1086/148245.

Sanders, R. L. et al. 2023a. *ApJ*, vol. 943, p. 75. DOI: 10.3847/1538-4357/aca9cc.

Sanders, R. L. et al. 2023b. *ApJ*, vol. 955, p. 54. DOI: 10.3847/1538-4357/acedad.

Santoro, F. et al. 2020. *A&A*, vol. 644, A54. DOI: 10.1051/0004-6361/202039077.

Saxena, A. et al. 2018. *MNRAS*, vol. 480, pp. 2733–2742. DOI: 10.1093/mnras/sty1996.

Scherer, K. et al. 2022. *A&A*, vol. 664, A132. DOI: 10.1051/0004-6361/202243449.

Scheuer, P. A. G. 1974. *MNRAS*, vol. 166, pp. 513–528. DOI: 10.1093/mnras/166.3.513.

Schmidt, M. 1963. *Nature*, vol. 197, p. 1040. DOI: 10.1038/1971040a0.

Schmidt, M. 1970. *ApJ*, vol. 162, p. 371. DOI: 10.1086/150668.

Schmidt, M. and Green, R. F. 1983. *ApJ*, vol. 269, pp. 352–374. DOI: 10.1086/161048.

Scholtz, J. et al. 2020. *MNRAS*, vol. 492, pp. 3194–3216. DOI: 10.1093/mnras/staa030.

Seyfert, C. K. 1943. *ApJ*, vol. 97, p. 28. DOI: 10.1086/144488.

Seymour, N. et al. 2007. *ApJS*, vol. 171, pp. 353–375. DOI: 10.1086/517887.

Seymour, N. et al. 2011. *MNRAS*, vol. 413, pp. 1777–1786. DOI: 10.1111/j.1365-2966.2011.18253.x.

Seymour, N. et al. 2012. *ApJ*, vol. 755, p. 146. DOI: 10.1088/0004-637X/755/2/146.

Shakura, N. I. and Sunyaev, R. A. 1973. *A&A*, vol. 24, pp. 337–355.

Shangguan, J. et al. 2018. *ApJ*, vol. 854, p. 158. DOI: 10.3847/1538-4357/aaa9be.

Shankar, F. et al. 2009. *ApJ*, vol. 690, pp. 20–41. DOI: 10.1088/0004-637X/690/1/20.

Shukla, G. et al. 2021. *MNRAS*, vol. 501, pp. 5362–5378. DOI: 10.1093/mnras/staa3977.

Shull, J. M. 2014. *ApJ*, vol. 784, p. 142. DOI: 10.1088/0004-637X/784/2/142.

Shull, J. M. and van Steenberg, M. E. 1985. *ApJ*, vol. 298, pp. 268–274. DOI: 10.1086/163605.

Silk, J. and Rees, M. J. 1998. *A&A*, vol. 331, pp. L1–L4. DOI: 10.48550/arXiv.astro-ph/9801013.

Silva, M. et al. 2018. *MNRAS*, vol. 474, pp. 3649–3672. DOI: 10.1093/mnras/stx3019.

Silva, M. et al. 2020. *MNRAS*, vol. 495, pp. 4707–4746. DOI: 10.1093/mnras/staa1409.

Singha, M. et al. 2023. *arXiv e-prints*, arXiv:2309.16926. DOI: 10.48550/arXiv.2309.16926.

Smail, I. et al. 2012. *ApJ*, vol. 760, p. 132. DOI: 10.1088/0004-637X/760/2/132.

Smirnova-Pinchukova, I. et al. 2022. *A&A*, vol. 659, A125. DOI: 10.1051/0004-6361/202142011.

Smith, D. J. B. and Jarvis, M. J. 2007. *MNRAS*, vol. 378, pp. L49–L53. DOI: 10.1111/j.1745-3933.2007.00318.x.

Snedden, S. A. and Gaskell, C. M. 1999. *ApJ*, vol. 521, pp. L91–L94. DOI: 10.1086/312188.

Sobral, D. et al. 2013. *MNRAS*, vol. 428, pp. 1128–1146. DOI: 10.1093/mnras/sts096.

Soifer, B. T. et al. 1987. *ApJ*, vol. 320, p. 238. DOI: 10.1086/165536.

Solórzano-Iñarrea, C. et al. 2004. *MNRAS*, vol. 351, pp. 997–1014. DOI: 10.1111/j.1365-2966.2004.07842.x.

Somerville, R. S. et al. 2008. *MNRAS*, vol. 391, pp. 481–506. DOI: 10.1111/j.1365-2966.2008.13805.x.

Soto, K. T. et al. 2016. *MNRAS*, vol. 458, pp. 3210–3220. DOI: 10.1093/mnras/stw474.

Spitzer, L. 1962.

Springel, V. et al. 2005. *MNRAS*, vol. 361, pp. 776–794. DOI: 10.1111/j.1365-2966.2005.09238.x.

Stacey, H. R. et al. 2019. *A&A*, vol. 622, A18. DOI: 10.1051/0004-6361/201833967.

Stalevski, M. et al. 2017. *MNRAS*, vol. 472, pp. 3854–3870. DOI: 10.1093/mnras/stx2227.

Steidel, C. C. et al. 1991. *AJ*, vol. 101, p. 1187. DOI: 10.1086/115755.

Steidel, C. C. et al. 2000. *ApJ*, vol. 532, pp. 170–182. DOI: 10.1086/308568.

Storey, P. J. and Sochi, T. 2013. *MNRAS*, vol. 430, pp. 599–610. DOI: 10.1093/mnras/sts660.

Storey, P. J. and Sochi, T. 2014. *MNRAS*, vol. 440, pp. 2581–2587. DOI: 10.1093/mnras/stu477.

Sturm, E. et al. 2011. *ApJ*, vol. 733, p. L16. DOI: 10.1088/2041-8205/733/1/L16.

Sutherland, R. S. et al. 2013. Astrophysics Source Code Library, record ascl:1306.008.

Swinbank, A. M. et al. 2015. *MNRAS*, vol. 449, pp. 1298–1308. DOI: 10.1093/mnras/stv366.

Tadhunter, C. 2008. *New Astron. Rev.*, vol. 52, pp. 227–239. DOI: 10.1016/j.newar.2008.06.004.

Tadhunter, C. N. 2002. *Revista Mexicana de Astronomia y Astrofisica Conference Series*. Ed. by W. J. Henney et al. Vol. 13, pp. 213–221.

Tadhunter, C. N. et al. 1989. *European Southern Observatory Conference and Workshop Proceedings*. Ed. by E. J. A. Meurs and R. A. E. Fosbury. Vol. 32, p. 293.

Taniguchi, Y. and Shioya, Y. 2000. *ApJ*, vol. 532, pp. L13–L16. DOI: 10.1086/312557.

Taylor, A. J. et al. 2022. *ApJ*, vol. 939, p. L3. DOI: 10.3847/2041-8213/ac959d.

Thomas, A. D. et al. 2016. *ApJ*, vol. 833, p. 266. DOI: 10.3847/1538-4357/833/2/266.

Thwala, S. A. et al. 2019. *MNRAS*, vol. 485, pp. 1938–1946. DOI: 10.1093/mnras/stz347.

Tortora, C. et al. 2009. *MNRAS*, vol. 396, pp. 61–77. DOI: 10.1111/j.1365-2966.2009.14718.x.

Trebitsch, M. et al. 2016. *A&A*, vol. 593, A122. DOI: 10.1051/0004-6361/201527024.

Tristram, K. R. W. et al. 2007. *A&A*, vol. 474, pp. 837–850. DOI: 10.1051/0004-6361:20078369.

Tristram, K. R. W. et al. 2014. *A&A*, vol. 563, A82. DOI: 10.1051/0004-6361/201322698.

Tsallis, C. 1988. *Journal of Statistical Physics*, vol. 52, pp. 479–487. DOI: 10.1007/BF01016429.

Tsallis, C. et al. 1995. *Physical Review Letters*, vol. 75, pp. 3589–3593. DOI: 10.1103/PhysRevLett.75.3589.

Tumlinson, J. et al. 2017. *ARA&A*, vol. 55, pp. 389–432. DOI: 10.1146/annurev-astro-091916-055240.

Uchiyama, H. et al. 2022. *ApJ*, vol. 926, p. 76. DOI: 10.3847/1538-4357/ac441c.

Umehata, H. et al. 2019. *Science*, vol. 366, pp. 97–100. DOI: 10.1126/science.aaw5949.

Urry, C. M. and Padovani, P. 1995. *PASP*, vol. 107, p. 803. DOI: 10.1086/133630.

Vaddi, S. et al. 2019. *MNRAS*, vol. 484, pp. 385–408. DOI: 10.1093/mnras/sty3494.

van Breugel, W. et al. 1999. *ApJ*, vol. 518, pp. L61–L64. DOI: 10.1086/312080.

van Hoof, P. A. M. et al. 2004. *MNRAS*, vol. 350, pp. 1330–1341. DOI: 10.1111/j.1365-2966.2004.07734.x.

van Ojik, R. et al. 1996. *A&A*, vol. 313, pp. 25–44. DOI: 10.48550/arXiv.astro-ph/9608099.

van Ojik, R. et al. 1997. *A&A*, vol. 317, pp. 358–384. DOI: 10.48550/arXiv.astro-ph/9608092.

Vasyliunas, V. M. 1968. *JGR*, vol. 73, pp. 2839–2884. DOI: 10.1029/JA073i009p02839.

Vayner, A. et al. 2017. *ApJ*, vol. 851, p. 126. DOI: 10.3847/1538-4357/aa9c42.

Vayner, A. et al. 2023. *arXiv e-prints*, arXiv:2307.13751. DOI: 10.48550/arXiv.2307.13751.

Veilleux, S. 1991. *ApJS*, vol. 75, p. 383. DOI: 10.1086/191535.

Veilleux, S. et al. 2020. *A&A Rev.*, vol. 28, p. 2. DOI: 10.1007/s00159-019-0121-9.

Venemans, B. P. et al. 2007. *A&A*, vol. 461, pp. 823–845. DOI: 10.1051/0004-6361:20053941.

Venturi, G. et al. 2021. *A&A*, vol. 648, A17. DOI: 10.1051/0004-6361/202039869.

Venturi, G. et al. 2023. *arXiv e-prints*, arXiv:2309.02498. DOI: 10.48550/arXiv.2309.02498.

Verhamme, A. et al. 2006. *A&A*, vol. 460, pp. 397–413. DOI: 10.1051/0004-6361:20065554.

Verhamme, A. et al. 2008. *A&A*, vol. 491, pp. 89–111. DOI: 10.1051/0004-6361:200809648.

Vernet, J. et al. 2001. *A&A*, vol. 366, pp. 7–25. DOI: 10.1051/0004-6361:20000076.

Vernet, J. et al. 2017. *A&A*, vol. 602, p. L6. DOI: 10.1051/0004-6361/201730865.

Villar-Martín, M. et al. 1996. *A&A*, vol. 312, pp. 751–760. DOI: 10.48550/arXiv.astro-ph/9605009.

Villar-Martín, M. et al. 1997. *A&A*, vol. 323, pp. 21–30. DOI: 10.48550/arXiv.astro-ph/9701016.

Villar-Martín, M. et al. 1999. *A&A*, vol. 351, pp. 47–58. DOI: 10.48550/arXiv.astro-ph/9909265.

Villar-Martín, M. et al. 2001. *ApSSS*, vol. 277, pp. 571–574. DOI: 10.1023/A:1012764309451.

Villar-Martín, M. et al. 2003. *MNRAS*, vol. 346, pp. 273–294. DOI: 10.1046/j.1365-2966.2003.07090.x.

Villar-Martín, M. et al. 2006. *MNRAS*, vol. 366, pp. L1–L5. DOI: 10.1111/j.1745-3933.2005.00118.x.

Villar-Martín, M. et al. 2007a. *MNRAS*, vol. 375, pp. 1299–1310. DOI: 10.1111/j.1365-2966.2006.11371.x.

Villar-Martín, M. et al. 2007b. *MNRAS*, vol. 378, pp. 416–428. DOI: 10.1111/j.1365-2966.2007.11811.x.

Villar-Martín, M. et al. 2008. *MNRAS*, vol. 390, pp. 218–226. DOI: 10.1111/j.1365-2966.2008.13779.x.

Villar-Martín, M. et al. 2011. *MNRAS*, vol. 418, pp. 2032–2042. DOI: 10.1111/j.1365-2966.2011.19622.x.

Villar-Martín, M. et al. 2014. *MNRAS*, vol. 440, pp. 3202–3219. DOI: 10.1093/mnras/stu448.

Villar-Martín, M. et al. 2016. *MNRAS*, vol. 460, pp. 130–162. DOI: 10.1093/mnras/stw901.

Villar-Martín, M. et al. 2017. *MNRAS*, vol. 472, pp. 4659–4678. DOI: 10.1093/mnras/stx2209.

Villar-Martín, M. et al. 2018. *MNRAS*, vol. 474, pp. 2302–2312. DOI: 10.1093/mnras/stx2911.

Vogelsberger, M. et al. 2020. *Nature Reviews Physics*, vol. 2, pp. 42–66. DOI: 10.1038/s42254-019-0127-2.

Wang, A. et al. 2023a. *MNRAS*. DOI: 10.1093/mnras/stad2651.

Wang, C. et al. 2019a. *MNRAS*, vol. 482, pp. 3576–3590. DOI: 10.1093/mnras/sty2906.

Wang, F. et al. 2019b. *ApJ*, vol. 884, p. 30. DOI: 10.3847/1538-4357/ab2be5.

Wang, F. et al. 2021a. *ApJ*, vol. 907, p. L1. DOI: 10.3847/2041-8213/abd8c6.

Wang, W. et al. 2021b. *A&A*, vol. 654, A88. DOI: 10.1051/0004-6361/202141558.

Wang, W. et al. 2023b. *arXiv e-prints*, arXiv:2309.15144.

Weilbacher, P. M. et al. 2020. *A&A*, vol. 641, A28. DOI: 10.1051/0004-6361/202037855.

White, R. L. et al. 2007. *ApJ*, vol. 654, pp. 99–114. DOI: 10.1086/507700.

White, S. D. M. and Rees, M. J. 1978. *MNRAS*, vol. 183, pp. 341–358. DOI: 10.1093/mnras/183.3.341.

Whittle, M. 1985. *MNRAS*, vol. 213, p. 1. DOI: 10.1093/mnras/213.1.1.

Wilson, A. S. and Raymond, J. C. 1999. *ApJ*, vol. 513, pp. L115–L118. DOI: 10.1086/311923.

Wilson, A. S. et al. 1997. *ApJ*, vol. 482, pp. L131–L134. DOI: 10.1086/310702.

Winkel, N. et al. 2023. *A&A*, vol. 670, A3. DOI: 10.1051/0004-6361/202244630.

Wu, J. et al. 2017. *MNRAS*, vol. 468, pp. 109–121. DOI: 10.1093/mnras/stx416.

Wylezalek, D. et al. 2013. *ApJ*, vol. 769, p. 79. DOI: 10.1088/0004-637X/769/1/79.

Wylezalek, D. et al. 2020. *MNRAS*, vol. 492, pp. 4680–4696. DOI: 10.1093/mnras/staa062.

Wyse, A. B. 1942. *ApJ*, vol. 95, p. 356. DOI: 10.1086/144409.

Xu, Y. et al. 2023. *arXiv e-prints*, arXiv:2310.06614. DOI: 10.48550/arXiv.2310.06614.

Yang, Y. et al. 2014. *ApJ*, vol. 793, p. 114. DOI: 10.1088/0004-637X/793/2/114.

Yao, Z.-W. and Zhang, Y. 2022a. *ApJ*, vol. 939, p. 60. DOI: 10.3847/1538-4357/ac9b4d.

Yao, Z.-W. and Zhang, Y. 2022b. *ApJ*, vol. 936, p. 143. DOI: 10.3847/1538-4357/ac8979.

Yates-Jones, P. M. et al. 2021. *MNRAS*, vol. 508, pp. 5239–5250. DOI: 10.1093/mnras/stab2917.

Yuan, S. et al. 2016. *MNRAS*, vol. 462, pp. 1603–1615. DOI: 10.1093/mnras/stw1747.

Zakamska, N. L. et al. 2003. *AJ*, vol. 126, pp. 2125–2144. DOI: 10.1086/378610.

Zakamska, N. L. et al. 2004. *AJ*, vol. 128, pp. 1002–1016. DOI: 10.1086/423220.

Zakamska, N. L. et al. 2016. *MNRAS*, vol. 455, pp. 4191–4211. DOI: 10.1093/mnras/stv2571.

Zhang, Y. 2008. *A&A*, vol. 486, pp. 221–228. DOI: 10.1051/0004-6361:200809381.

Zhang, Y. et al. 2016. *ApJ*, vol. 817, p. 68. DOI: 10.3847/0004-637X/817/1/68.

Zhang, Z. T. et al. 2013. *MNRAS*, vol. 430, pp. 2605–2621. DOI: 10.1093/mnras/sts713.

Zheng, W. et al. 1997. *ApJ*, vol. 475, pp. 469–478. DOI: 10.1086/303560.

Zubovas, K. and King, A. 2012. *ApJ*, vol. 745, p. L34. DOI: 10.1088/2041-8205/745/2/L34.